Doctoral Dissertation

Study on the Effectiveness and Feasibility of a Newly Developed Tsunami Attenuation Method by Experimental and Numerical Approach

Thaw Tar

July 2018

Graduate School of Engineering,
Osaka University

Abstract

Large-scale oil spills and fires occurred in Kesennuma City, Miyagi Prefecture, Japan during the 2011 Great East Japan Earthquake due to the large-scale earthquake and subsequent tsunami, mainly due to the drifting, tumbling and damage of oil and gas storage tanks in that area. If Tokai-Nankai-Tonankai earthquakes occur, similar large-scale disasters might occur. Thus, it is urgent to develop countermeasures against such tsunami induced disasters.

As a kind of countermeasure, a new tsunami attenuation method was developed using flexible structures called flexible pipes instead of traditional rigid sea-wall type countermeasures. Flexible pipes are fire-hose-like pipes at a significantly larger scale which can be folded and installed on the sea-bed in such a way that the pipes would not disturb the surrounding marine traffic. At the moment of tsunami occurrence, these pipes are to be injected with compressed air, forming vertical flexible structures which can reduce the momentum of tsunamis.

This thesis deals with evaluation of the performance of a tsunami mitigation approach using flexible pipes in terms of effectiveness and feasibility, with the assumption of Osaka Bay as a target prevention area. This study was carried out in three parts:

1. Analysis on the effectiveness of flexible pipes based on material and orientatin
2. Analysis on the effectiveness of flexible pipes under a quasi-2D flow
3. Study on the feasibility of flexible pipe implementation by structural analysis.

This thesis is composed of six chapters:

Chapter 1 explains the needs of new types of tsunami countermeasures in order to prevent secondary disasters caused by tsunamis such as large-scale oil spills and fires. Then a brief preview of a newly developed countermeasure using flexible pipes is presented.

In Chapter 2, literature review of traditional and currently developed tsunami countermeasures are made. Moreover, current approaches to model tsunami flows and countermeasures in laboratory experiments as well as numerical models are reviewed.

In Chapter 3, the overview and concept design of newly developed tsunami countermeasure utilizing flexible pipes are explained, including the working principle of pipe deployment mechanisms. Then the specifications of this type of countermeasure are proposed for effectiveness and feasibility analysis.

In Chapter 4, the experimental setup and equipment for the experiments are explained in details including the calibration of sensors and choice of scale model pipes and tanks.

In Chapter 5, the dependency of flexible pipe performance on the material and orientation are experimentally investigated by comparing the reduction of wave force and flow velocities by three types of pipes with different bending stiffness values. Then, simulations were carried out to estimate the force reduction based on the orientation of the pipes arrangement.

Chapter 6 presents the effectiveness of flexible pipes under a quasi 2D flow, with the discussions on the reduction of momentum flux and reduction of wave forces acting on a cylindrical storage tank in semi-submerged condition, located on an earth-bank and with and without the presence of an artificial dyke wall.

Chapter 7 is divided into two parts. In the first part, the results of computations of inline and cross-flow behavior of flexible pipes as a two-way fluid structure interaction (FSI) problem are presented, including the lift and drag coefficients. In the second part, feasibility analysis of flexible pipes was carried out by conducting the structural analysis. The drag coefficients obtained from the first part were used in the structural analysis. From the full-scale rigid pipe simulations, the effectiveness of the flexible pipes in full-scale was estimated. Simulations results suggested that flexible pipes were effective and thus, feasible for real-world implementation.

Chapter 8 summarizes the main conclusions, including the main contributions and results of this study. Possible future improvements for this work are also presented.

Acknowledgements

First of all, I would like to express my sincere gratitude to Professor Naomi Kato for bringing to Osaka University, Japan and nurturing me by supervising my research, dedicating his time and experience during my Masters' course as well as PhD course. I have learned a lot of things from him, especially how to carry out research properly, the mindset of a researcher, the relentlessness and thinking based on logic. He took care of me very well not only with my research but also with my wellbeing in Japan. Since I was a privately-funded student, he partially supported me with my finance before I got scholarship for my PhD work. It is a great loss for me that Professor Kato passed away on 9th May, 2018. I deeply wish his soul rest in peace.

Secondly, I would like to appreciate Associate Professor Dr. Hiroyoshi Suzuki for his supervision with my research after the retirement of Professor Kato. I greatly appreciate his help as well as guidance during my PhD course, especially for his advice on experiments and simulations. Moreover, I am grateful to him for giving me the opportunity to use expensive experimental equipment and sophisticated high-performance computing facilities. Dr. Suzuki also took care of my student life at Osaka University such as giving me opportunities to apply for scholarships, so that I could focus on my research very well.

Thirdly, I am very grateful to Dr. Hidetaka Senga for his help with the experiments. He taught me how to connect the sensors to the computers by using different kinds of interfaces and amplifiers. I also appreciate him for his comments on my fluid structure interaction simulations.

I would like to express my special thanks to Matsuda Yosaichirou Scholarship Foundation and Nishimura Scholarship Foundation for awarding me with the scholarships for my Masters' and

doctoral courses. Without their financial support, my life would be much more difficult than my current situation.

I would like to acknowledge Professor Shin-ichi Aoki and Dr. Susumu Araki, from Department of Civil Engineering, Osaka University, for their kind permission to use their tsunami wave flume and related measurement equipment.

I would like to express my sincere gratitude to Mr. Yoshiki Nagai, Mr. Kazuhiro Ohnishi, Mr. Takuya Okubayashi for their help in the physically demanding experiments. I wish to show my deep appreciation to my sincere, close friend and lab member Dr. Wai Phyo Kyaw for his help in experiments and his advices in my numerical simulations.

My sincere gratitude to Dr. Mahdi Choyekh, Dr. Swrn Rathour, Dr. Wai Phyo Kyaw, Mr. Ukita, Mr. Takasu, Mr. Shoji, Mr. Okubayashi, Mr. Nagai, Mr. Ohnishi, Mr. Inoue, Mr. Ryan, Mr. Tomobe, Mr. Okuda, Mr. Sato and all other lab members during my stay in 7th Laboratory for their kind hearts and a nice and warm atmosphere.

I would like to deeply thank my parents for their physical, mental and financial support throughout my life. Without their support, I would not even be able to carry out these advanced studies in Japan.

Finally, I greatly appreciate my friends and relatives either from Japan or Myanmar for their understanding, forgiveness, peace and support.

List of published papers

Journal papers:

1. Tar, T., Kato, N., Suzuki, H., Nagai, Y., Ohnishi, K., Okbayashi, T. 2017. Experimental and numerical study on the reduction of tsunami flow using multiple flexible pipes, Journal of Loss Prevention in the Process Industries, 50 (B), 364-385
2. Tar. T., Kato, N. and Suzuki, H. 2017. Development of biologically inspired flexible pipes for tsunami attenuation, Marine Technology Society Journal 51(5), 116-136.

Peer-reviewed conference papers:

1. Tar, T., Suzuki, H., and Kato, N. 2018. Numerical study on the fluid structure interaction of largely deformable finite-length flexible structures in tsunami flow by strongly coupled partitioned approach. Proceedings of The Twenty-Eighth (2018) International Ocean and Polar Engineering Conference held by International Society of Offshore and Polar Engineers (ISOPE), June 10-15, Sapporo, Japan.

Nomenclature

EI	Bending stiffness
E	Modulus of elasticity
I	Moment of inertia
L	Length
D	Outside diameter
p_n	Porosity
V_v	Volume of void
V	Volume
$F_{no\ pipes}$	Hydrodynamic force acting on the tank when no flexible pipes were used
F_{pipes}	Hydrodynamic force acting on the tank when flexible pipes were used
$\bar{u}_i$	Flow velocity in *i* directions of Cartesian coordinate system
p	Pressure
ρ	Fluid density in finite volume framework
μ_{eff}	Effective dynamic viscosity
μ	Dynamic viscosity of fluid
μ_t	Turbulent dynamic viscosity
α	Single phase function of a finite volume cell
$\bar{u}_{c,i}$	Artificial compression term to compress the phase interface
U	Flow velocity of full-scale tsunami in inflow direction
u	Flow velocity of laboratory scale tsunami in inflow direction
g	Gravitational constant
H	Still water depth
η	Wave elevation

C_D	Drag coefficient
C_M	Inertia coefficient
ρ_{water}	Water density
ρ_{air}	Air density
ρ_{pipe}	Pipe density
ρ_S	Solid density
h	Flow depth of a tsunami flow
B	Breadth of structure being attacked by tsunami wave
F_D	Drag force on the structure caused by the tsunami flow
M	Momentum flux per breadth
$M_{average}$	Average value of maximum momentum fluxes from each test case
$M_{reduction}$	Reduced momentum flux
Re	Reynolds' number
KC	Keulegen-Carpenter number
ν	Kinematic viscosity
T	Period of tsunami wave
F_x	Horizontal force by the tsunami-like wave on the model oil tank
F_z	Vertical force by the tsunami-like wave on the model oil tank
$F_{x\_normalized}$	Normalized horizontal force
$F_{z\_normalized}$	Normalized vertical force
F_{x_max}	Maximum horizontal force on the model tank
F_{z_max}	Maximum vertical force on the model tank
$\mathbf{M}$	Mass matrix of the pipe in the finite element analysis
$\mathbf{K}$	Stiffness matrix of the pipe in the finite element analysis
$\mathbf{Q}_{\boldsymbol{e}}$	External force vector of the pipe in the finite element analysis
$\boldsymbol{e}$	Position vector for a node in the finite element analysis

$\ddot{\boldsymbol{e}}$	acceleration vector for a node in the finite element analysis
σ_f	Stress tensor
I	Unity tensor
γ	Mesh diffusivity coefficient
v_S	Solid velocity
u_S	Solid displacement

Contents

List of Figures

List of Tables

Chapter 1

Introduction

Background

In 2011, a large-scale earthquake (magnitude 9.0), occurred in Japan, called 2011 Great East Japan Earthquake. This earthquake caused a huge tsunami that attacked a large area along the North coasts of Japan. The maximum run-up of the tsunami was observed to be 40 m in the Iwate Prefecture, Japan (Mori, 2012). Most of the energy storage tanks in Japan such as oil and gas tanks in petroleum industrial complexes are located in the coastal areas because crude oil and natural gases are imported by means of maritime transport such as very large crude carriers (VLCCs). Many of such tanks located on the eastern coast of Japan were damaged and large-scale oil-spills and fires occurred during this 2011 earthquake tsunami. In total, 418 tanks were damaged during the earthquake, and the largest number of damaged tanks were observed in Miyagi, Iwate and Fukushima prefectures while 157 tanks suffered movements including washing away, sliding and tumble (Fire Defense Research Center, 2011). Smaller oil storage tanks were drifted and collapsed (Fig. 1.1, Fire Defense Research Center, 2011) while larger tanks suffered from movement and tumble, especially if these tanks were nearly empty (Fig. 1.2, Fire Defense Research Center, 2011).

Fig. 1.1 Oil tank drifted and collapsed by tsunami (Fire Defense Research Centre, 2011)

It is believed that this damage of oil tanks by 2011 Great East Japan Earthquake is the largest-scale one in the world caused by tsunami on oil and gas storage tanks (Hatayama, 2014). It is estimated that 11,521kL of various types of oil (7,530kL heavy oil, 498kL kerosene, 1,958kL diesel, 1535kL gasoline) spilled in Kesennuma City, Miyagi Prefecture and 4400kL of oil in Sendai Oil Refinery (Fire Defense Research Center, 2011). Such a severe scenario is shown in Fig. 1.3, showing the occurrence of oil spill and the spilled oil leaking inside and outside of the dyke walls surrounding the oil storage tanks.

Fig. 1.2 Movement and tumblesome of large tanks (Fire Defense Research Centre, 2011)

Fig. 1.3 Oil spill occurred from a tank, with the leaked oil inside and outside the dyke wall (Fire Defense Research Centre, 2011)

A large-scale fire broke out in Sendai Oil Refinery area after the tsunami and oil-spills. According to the interviews with the staff at the incident site, the spilled oil was floating on the water surface and was ignited by some sparks, causing a large-scale fire. Several oil and gas tanks were burnt down during this fire (Fire Defense Research Center, 2011) as in Fig. 1.4a and Fig. 1.4b.

The spilled oil on the water surface started large-scale fires burning on the water which was very difficult for the firefighters to extinguish (Fig. 1.5).

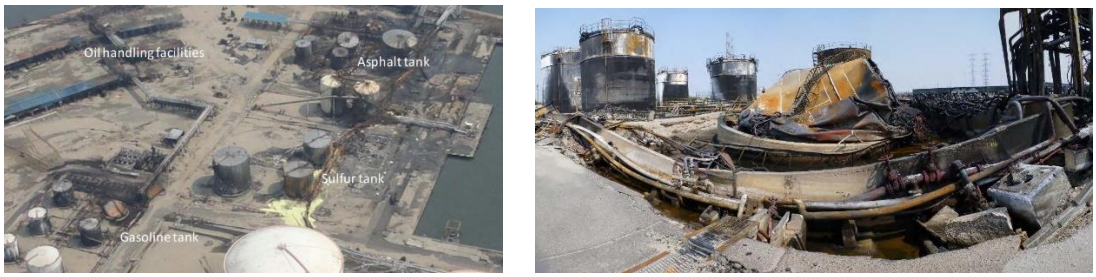

(a) (b)

Fig. 1.4 (a) Burnt out section in an oil refinery in Sendai area (Fire Defense Research Centre, 2011) (b) Closer view of a burnt oil tank

Fig. 1.5 Spilled crude oil causing a large-scale fire on water surface in the port area in Kesennuma City (Yomiuri Shinbun)

Fig. 1.6 Mud sample with oil contamination in Kesennuma City (The Mainichi Newspaper, 2012)

Tsunami induced oil-spills from oil and petroleum complexes in 2011 Great East Japan Earthquake tsunami not only caused large fires but also led to severe environmental problems. Tsunami flows are highly turbulent, causing high turbid sea water. When the water comes in contact with the spilled oils caused by tsunami, there is a potential for mixing of the oil and soil particles (Kyaw, 2017). Consequently, the heavier oil-soil mixture tends to sink to the sea

bed instead of floating on the sea surface. This kind of mixture is difficult to recover, causing severe long-term environmental problems to the sea as well as the shore. One of the mud samples taken from the coastal area of Kesennuma City, Japan is shown in Fig. 1.6, showing the soil was severely contaminated with spilled oil due to tsunami.

Such disasters will be anticipated in Osaka Bay, Tokyo Bay or Ise Bay if Tokai-Nankai-Tonankai earthquake occurs. In this thesis, Osaka Bay scenario is considered. In the Sakai Senboku Industrial Zone area, Sakai City, Osaka Prefecture, there are 818 oil tanks (satellite map in Fig. 1.7) while in Osaka North Port area, Osaka City, Osaka Prefecture, there are 237 oil tanks vulnerable to large-scale oil-spills and fires if tsunami attack occurs (Kyaw, 2017). It is very urgent to develop countermeasures to prevent or reduce the risk of such disasters caused by large tsunamis.

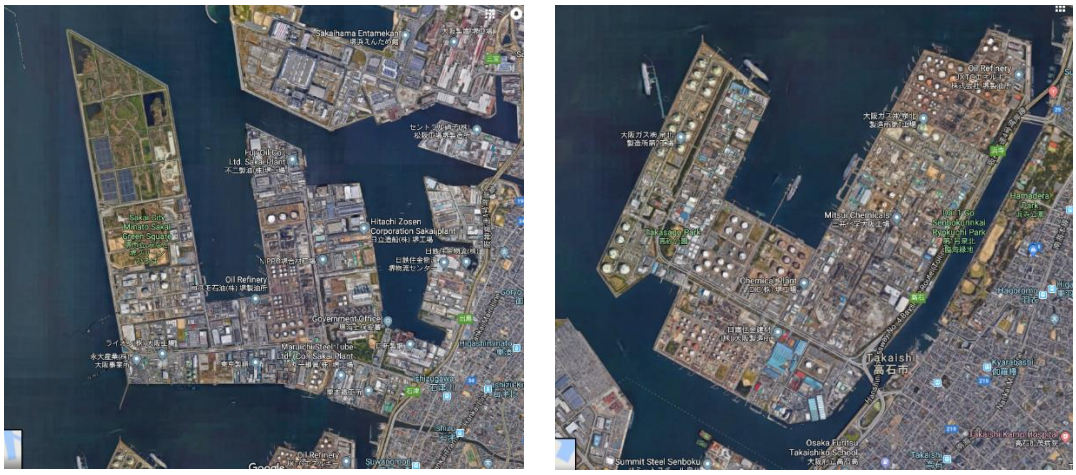

Fig. 1.7 Oil refineries in Sakai Senboku area, Osaka, showing several oil storage tanks

1.1 Introduction to newly developed countermeasure with flexible structures

After the occurrence of the 2011 Great East Japan Earthquake, hardware countermeasures to tsunami-oriented risk were taken according to the policy of Ministry of Land, Infrastructure, Transport and Tourism, Japan (2012). These countermeasures include the redesign of port configuration, including concrete tsunami embankments and the setting of breakwaters in the industrial complexes. One of the major problems with such countermeasures is that these breakwaters and sea-walls would disturb the marine traffic for normal calm conditions. Therefore, recently, breakwaters have been being designed not to disturb the environment during normal conditions and to be able to deploy only when the tsunami warning is triggered.

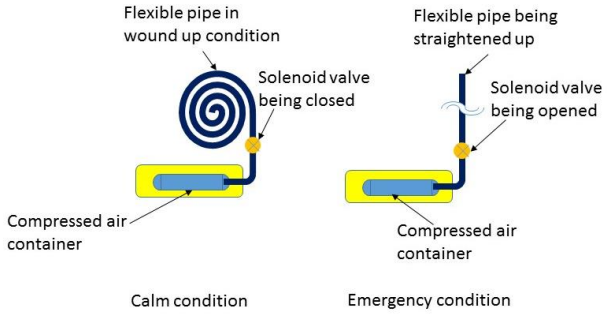

Fig. 1.8 Operation of flexible pipes in calm condition and emergency condition

From the viewpoints of cost-effectiveness and environmental friendliness, Kato et al. (2014) introduced the use of bio-inspired flexible pipes to reduce the tsunami-related damage. The operation of flexible pipes is illustrated in Fig. 1.8. for the calm condition, the pipes are to be wound up and connected to a compressed air source such as a compressed air container or air compressor via a remotely operated solenoid valve. This arrangement is placed on the seabed in front of the industrial parks that hold the oil and gas storages. In the emergency condition, the solenoid valves are opened, letting the compressed air into the flexible pipes, with enough air pressure to stand the flexible pipes being upright as shown in Fig 1.8 (right).

Several hundreds or thousands of flexible pipes can be installed together to form a flexible-pipe arrangement having multiple rows of pipes. One of the characteristics of this approach is that the momentum carried by the tsunami wave is reduced gradually by the drag forces of the flexible-pipe-system instead of attempting to stop the tsunami flow at once. Moreover, such a system can be constructed in conjunction with the other tsunami countermeasures such as earth-bank arrangements.

1.2 Objectives

The main objectives of this study are

1. To investigate the effectiveness of flexible pipes in decreasing momentum carried by the tsunami and
2. To evaluate the feasibility for practical implementation of flexible-pipe-system on the coasts of Japan.

To achieve the first objective, scale-model experiments were conducted and reductions of flow velocities and elevation were compared. Moreover, hydrodynamic forces acting on scale-model oil tanks were measured and compared to directly estimate the effectiveness of the pipes in tsunami damage protection of energy storage tanks in real world. Numerical studies, replicating the experiments, were also carried out in finite volume framework. Numerical models were validated by comparing with the experiment results and detail analyses were made on the flow phenomena.

To investigate the second objective, the deformations of flexible pipes under the tsunami load were investigated numerically based on experimental data, considering this as a one-way fluid structure interaction (FSI) problem. The drag and inertia coefficients of a single flexible pipe required in these computations were numerically determined assuming this problem as a two-way FSI phenomenon.

1.3 Methodology

One of the main characteristics of this tsunami damage reduction technique is that flexible structures are utilized instead of rigid structures. However, this approach leads to a major problem. If the bending stiffness (EI) of the pipes is not large enough, the deformations of the pipes will be very large under the tsunami load, significantly affecting the effectiveness of the pipes in tsunami load reduction. On the other hand, it is not feasible to obtain rigid-structure-like bending stiffness in the flexible pipes due to the limitations in the compressed air pressure as well as lack of molecular integrity of solids such as wood or steel. Therefore, it is necessary to consider the minimum bending stiffness which can make the system effective.

To compare the effectiveness of different EI values, different materials with different EI were used as scale-model flexible pipes as the first stage. From these experiments, it was observed that the pipes with minimum EI could reduce the hydrodynamic force by the tsunami acting on the scale-model tank similarly as harder pipes. Therefore, this type of material was considered for further investigations in the next steps.

In the second stage, the influence of the width of flexible-pipe-arrangement in the cross-flow direction on the force reduction performance was addressed. Simulations with open-source computational fluid dynamics (CFD) were conducted using the same scale and conditions as the experiments with the assumption of rigid pipes and the simulation results were validated with experimental results. Then, the effect of different widths on the reduction performance was estimated from the numerical results.

In the third stage, experiments were carried out with the assumption of a quasi-2D scenario, i.e., without the effect of flow around the pipes being considered. Reduction of momentum, surface elevation and hydrodynamic forces were measured to estimate the full-scale wave load reduction.

In the fourth stage, the deformations of full-scale pipes were predicted by means of numerical method by combining the results of one-way FSI problem and two-way FSI problem.

With this approach, it will be possible to properly assess the effectiveness and feasibility of the flexible pipe system as one of the tsunami mitigation schemes.

1.4 Structure of the thesis

The thesis is composed of 8 chapters, including this introduction.

- Chapter 2 is divided into two parts. In the first part, the traditional and currently developed tsunami countermeasures are reviewed, briefly explaining their concept design as well as the pros and cons of each major type of countermeasures. In the second part of this chapter, current approaches to represent tsunami flows and countermeasures in laboratory experiments as well as in computations will be discussed.
- In Chapter 3, the overview and concept design of flexible pipes are described, including the working principles of pipe deploying mechanisms and design specifications.
- In Chapter 4, the experimental setup including the experimental wave basin, measurement equipment and scale model flexible pipes and energy storage tanks
- In Chapter 5, the wave force reduction performances by different materials and different orientations are presented.
- Chapter 6 presents the effectiveness of flexible pipes under a quasi 2D tsunami flow, with the discussions on reduction of unsteady momentum flux, reduction of wave forces acting on a cylindrical oil storage tank in semi-submerged condition, located on an earth-bank and with and without the presence of an artificial dyke wall.
- Chapter 7 is divided into two parts. In the first part, the results of computations of the inline and cross-flow behavior of flexible pipes as a two-way fluid structure interaction

(FSI) problem are presented, including the cross-flow vibration frequencies and amplitudes as well as lift and drag coefficients. The second part presents the results of structural analysis, showing the prediction of deformation of full-scale pipe under a uniform flow corresponding to a tsunami, using the drag coefficients predicted from the first part of this chapter.

- Chapter 8 concludes, summarizing the main contributions and results of this study.

Chapter 2

Literature review

According to the definition of Ministry of Land, Infrastructure, Transport and Tourism, Japan (MLITT, 2012), tsunamis are categorized as Level 1 and Level 2. Level 1 tsunamis are caused by earthquakes with the occurrence of once in one-hundred years while Level 2 tsunamis are corresponding to earthquakes with the occurrence of once in several hundred years to 1000 years. The responsibility of tsunami countermeasures for Level 1 tsunami include

(1) protection of human life

(2) continuation of economic activities and

(3) continuation of port functions immediately after the tsunami.

However, for Level 2 tsunamis, the countermeasures must be able to provide

(1) protection of human life

(2) prevention of secondary disasters (namely oil-spills and fires)

(3) support for fast recovery of damaged areas.

Several countermeasures have been introduced for Level 2 tsunamis based on these points described above. Another requirement for the tsunami countermeasures which are to be employed for protecting the industrial complexes is that these countermeasures should not disturb the marine traffic during the normal days where there is no tsunami attack. Since the

occurrence of 2011 Great East Japan Earthquake tsunami, new types of countermeasures have been developed while existing traditional tsunami countermeasures were reviewed and improved by not only Japanese researchers but also researchers and engineers around the world. On the other hand, tsunami damage on residential areas as well as industrial complexes were estimated by either experimental or numerical approaches.

2.1 Current developments on tsunami countermeasures

2.1.1 Traditional tsunami countermeasures

Tsunami countermeasures include traditional breakwaters and sea-walls as well as newly developed technologies that can raise the sea-walls only when the tsunami occurs. For instance, the breakwaters in Kamaishi city, Iwate Prefecture are 63 m deep structures. These breakwaters are 670 and 990 m long with a 300 m opening as in Fig 2.1. During 2011 Tohoku tsunami, these breakwaters could reduce tsunami inundation height at the shore-line from 13.7 to 8.0 m and run-up height from 20.2 to 10 m although the breakwaters themselves were severely damaged by the tsunami (Suppasri et al., 2013). Several hundreds of kilometers of sea-walls have been constructed along the shores of Japan to protect the residential areas by allowing tsunami to flow around the sides of the sea-walls (Suppasri et al., 2013). Such countermeasures are suitable for protecting residential areas along the shore-line. However, the rigid structures such as breakwaters and seawalls would disturb the marine traffic and fishery activities during normal (calm) conditions and destroy the scenery. While it is very important to review and improve the existing seawalls for most of the coastal areas, it is still necessary to develop countermeasures that have no significant disturbance to the marine traffic.

Fig. 2.1 Tsunami breakwaters in Kamaishi city and Ofunato city before the 2011 tsunami (Suppasri et al.)

2.1.2 Natural tsunami countermeasures

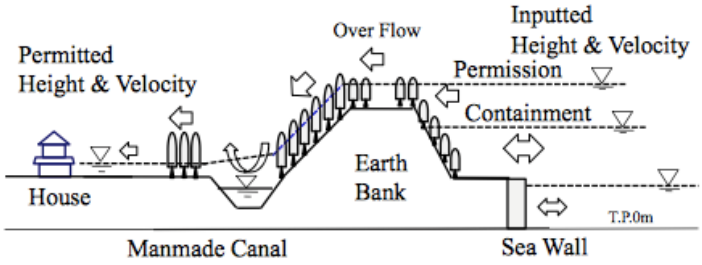

Fig. 2.2 Design concept against tsunami with earth bank, sea-wall and manmade canal (Tokida et al., 2014)

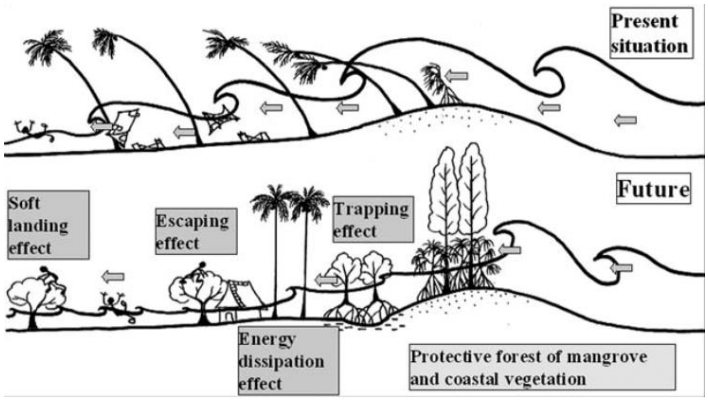

Fig. 2.3 Functions of coastal vegetation during tsunami inundation (Tokina et al., 2007)

Several researchers have been studying the effectiveness of naturally-inspired tsunami countermeasures such as mangroves and earth-banks since the occurrence of 2004 Indian Ocean tsunami. Tokida and Tanimoto (2014) discussed the combined effect of natural earth-bank and manmade canals and dug pools in reducing tsunami damage on residential areas based on the surveys during 2004 Indian Ocean tsunami and 2011 Japan tsunami. Their concept design is shown in Fig. 2.2. Their model was designed to protect wooden houses from tsunami and it is very promising to protect residential areas.

On the other hand, mangrove plants alone were observed to be effective in reducing tsunami damage of households.Tanaka et al. (2007) pointed out that mangrove (*Rhizophora apiculata* and *Sonneratia sp*) was effective in providing protection from tsunami damage by the drag caused by these plants and by catching floating debris, according to field surveys on the southern coast of Sri Lanka and on the Andaman coast of Thailand after 2004 Indian Ocean tsunami.

Several experiments and field survey works including Irtem (2009), Huang et al. (2011), Bao (2011), and Mazda et al. (2006) gave similar results to Tanaka et al. (2007)'s work. Various numerical models including Boussinesq equations with body force terms, full Navier-Stokes equations with cylindrical structures representing the mangrove plants, and body force models and spectral models have also been developed and used to confirm the effectiveness of mangrove in wave energy reduction by many researchers such as Maza et al. (2015), Huang et al. (2011) and Suzuki et al. (2011). However, the growth of such plants as mangrove on the coast of Japan would certainly disturb the marine traffic near the oil related industrial compounds to be protected. Moreover, it would be environmentally impossible to raise mangroves in those countries such as Japan located in the mid latitude. Rosman et al. (2013) carried out experiments to investigate the interaction of flexible giant-kelps (*Macrocytis pyrifera*) with orbital waves using 1/25 scale flexible structures that represented kelp forests.

They compared the horizontal orbital velocities and wave elevations of linear waves with and without giant-kelps models. According to their work, kelp forests also have the ability to attenuate wave energy through energy dissipation although the effectiveness is lower than mangrove.

2.1.3 Recently developed tsunami countermeasures

Several new technologies were introduced as tsunami countermeasures without significant disturbance to marine traffic. Takayama et al. (2010) developed a buoyancy-driven vertical piling system in which large rigid cylindrical steel pipes are inserted into the sea-bed by means of piling. Compressed air is pumped into these pipes in order to make them move to the free-surface, forming a rigid wall made of rigid cylinders when tsunami attack occurs as illustrated in Fig. 2.4. They carried out scale-model experiments and actual field tests with full-scale structures at Numazu Port, Shizuoka, Japan. Kimura et al. (2012) introduce the use of flap-gate breakwater system where the breakwaters are placed on the sea-bed and raised up as a continuous seawall by means of buoyancy when tsunami or storm surges come in (Fig. 2.5). Both approaches use a wall type breakwater to cut down the tsunami force by a large factor and both of them would not disturb the marine traffic due to their placement on the sea-bed during the calm conditions. On the other hand, rigid walls and rigid mechanisms are employed in both systems. Therefore, if the earthquake is too strong (Magnitudes larger than 7.0) or if the tsunami height is too large (Level 2 tsunamis), the structural response of such systems might lead to breakage of the walls as well as the mechanisms for deploying the walls.

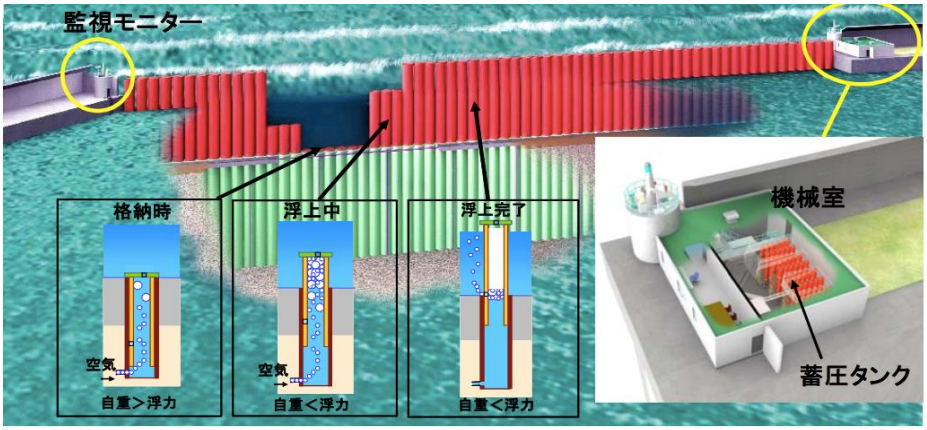

Fig. 2.4 Buoyancy driven vertical piling system (imagination, Takayama et al., 2010)

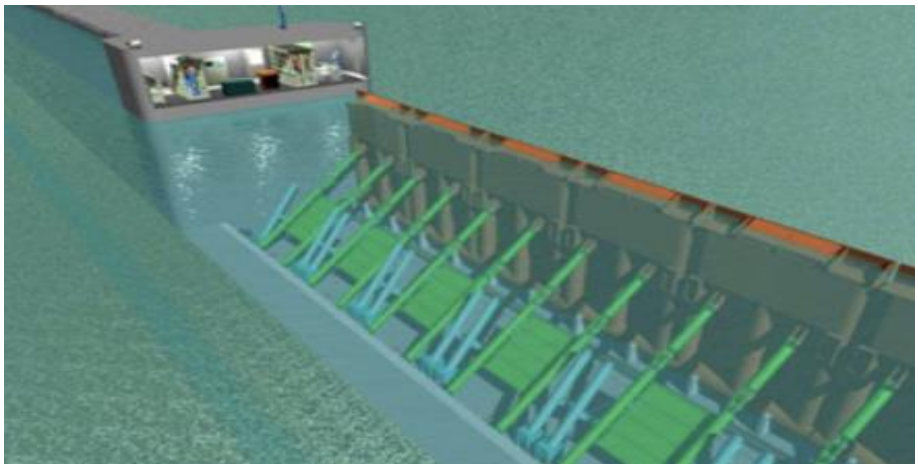

Fig. 2.5 Flap-gate breakwater system (imagination, Kimura et al., 2012)

2.2 Studies on tsunami and interaction of oil tanks with tsunami flows

2.2.1 Generation of tsunami wave in laboratory

Tsunami can be regarded as a long-period shallow water wave having periods of several minutes to several tens of minutes. Therefore, it is usually necessary to use long-stroke paddle type wave generators to create scale-model tsunami-like long-period waves. In the experiments carried out by Kunimatsu et al. (2015), they used a wave generator with a 1.4 m long stroke which spans for a period of 10 seconds. This wave generator can generate a wave having approximately 10-second-peroid with the maximum elevation of 10 cm. Iemura et al. (2007) used a similar approach in their experiments measuring the tsunami wave force acting on a

bridge located inland. Several other researchers including Matsumoto et al. (2013), Huang et al. (2011) and Fujii and Imamura (2010) also carried out experiments using the same tsunami wave generation approach.

On the other hand, dam break method was also employed as a means of laboratory scale tsunami generation. Imamura et al. (2008) investigated the motion of boulders along the tsunami run-up on a laboratory scale by using dam-break method to create a run-up bore. This approach is suitable for the experiments in which the effects of backwash flow are studied. In their work, they could predict the maximum position of the boulder transported by tsunami flow as well as the final stop position. Liu et al. (2014) also experimentally predicted the motions of boulder drifted along the tsunami with a dam break bore.

2.2.2 Numerical modeling of tsunami flows

Modeling methods of tsunami flows vary depending on the phenomena to be investigated. Fault models can be used to generate a tsunami wave corresponding to the earthquake that causes that tsunami. This approach relies on the fault model and useful for very large-scale predictions of tsunami wave height and run-up height. In the report of Ministry of Land, Infrastructure, Transport and Tourism, Japan (MLITT, 2012), Storm Surge and Tsunami Simulator in Oceans and Coastal Areas (STOC) code was used to compute the run-up of 2011 Japan tsunami towards the Kamaishi harbor. This code utilizes nested mesh technique in order to solve the tsunami wave for different accuracies at different locations. The simulation results showed good agreements with measured run-up using the GPS data during the tsunami. Kyaw (2017) also used to predict the tsunami run-up in Osaka Bay caused a Nankai-fault-earthquake. In their model, a fault zone representing the Nankai fault was used to compute the initial water elevation which was used to generate the tsunami.

For smaller scale simulations, especially for the replication of experiments, the Boussinesq equations (Boussinesq, 1872) are widely used with the assumption of tsunami as a non-linear solitary wave. Huang et al. (2011) used this approach to estimate the mean drag coefficients of mangrove forests in the tsunami flow. Their numerical results agreed very well with the experiments provided that there was no run-up and wave breaking occurring. For simulations involving serious wave breaking, Volume of Fluid (VoF) model have been used. Ramsden (1990) computed the phenomenon of a coastal bore by solving the full Navier-Stokes equations on a 2D finite difference grid with VoF approach. Maza et al. (2015) used 3D Reynolds Averaged Navier-Stokes (RANS) solver with VoF method to compute a lab-scale tsunami flow around scale-model mangroves. In their work, Boussinesq equations were solved and the elevation results were fed as boundary conditions to the RANS solver. They could estimate the wave energy dissipated by the mangrove forest.

2.2.3 Estimation of tsunami wave force on coastal structures

It is important to estimate the wave force acting on the structures by the tsunami in order to estimate the wave force reduced by the proposed tsunami attenuation method. Yeh (2007) and FEMA P646 (2008) proposed that the design drag force on a structure can be computed by the following equation.

$$F_D = \frac{1}{2}\rho C_D B (hu^2)_{max} \tag{2.1}$$

where, h is the flow depth at the location of interest when there is no flow obstruction and u is the flow velocity at that point. ρ is the water density, C_D is the drag coefficient and B is the breadth of the structure. Yeh (2007) also pointed out that the maximum momentum flux per unit mass of water represented by $(hu^2)_{max}$ does not equal to $h_{max}u_{max}^2$ because the maximum flow velocity and maximum elevation do not occur simultaneously. To estimate $(hu^2)_{max}$, Yeh (2006) developed an envelope curve of hu^2along the beach based on the analytic solution of the nonlinear shallow-water wave theory. According to Yeh (2006)'s equation, hu^2can be estimated as:

$$\frac{(hu^2)_{max}}{gR^2} = 0.125 - 0.235\frac{z}{R} + 0.11\left(\frac{z}{R}\right)^2 \tag{2.2}$$

where, R is the ground elevation at the maximum tsunami penetration measured from initial shoreline, and z is the ground elevation of the location of interest.

The formula suggested by Yeh (2007) is suitable for the design purposes of building and structures located on the coastal areas which are vulnerable to tsunami attacks with the assumption of tsunami flow as a quasi-steady flow. However, in order to estimate the unsteady forces including inertia forces, equations including unsteady terms such as Morison's equation (Morison et al., 1950) are considered. Kunimatsu et al. (2015) experimentally studied the usability of Morison's equation in predicting tsunami load on oil storage tanks. Araki et al.

(2016) confirmed the applicability of Morison's formula in tsunami load estimation by improving Kunimatsu's work.

Based on above approaches, several researchers experimentally predicted the wave forces on residential structures or oil tanks. Matsumoto et al. (2013) measured the drag force acting on a horizontal pipeline and oil tanks as well as the vertical distributions of laboratory scale tsunami wave. Ikemura et al. (2007), predicted the drag force of a bridge under tsunami flow by using a 1:77 length scale-model bridge. They also measured the impact load on the bridge by a floating boulder as well as the effect of a breakwater in tsunami damage reduction. Fujii and Imamura (2010) measured the tsunami force acting on multiple oil storage tanks in different arrangements by considering the interaction between each oil tank. Kunimatsu et al. (2015) also studied the effect of surrounding oil tanks on the hydrodynamic forces acting on a tank.

2.2.4 Oil tank motion under tsunami flow

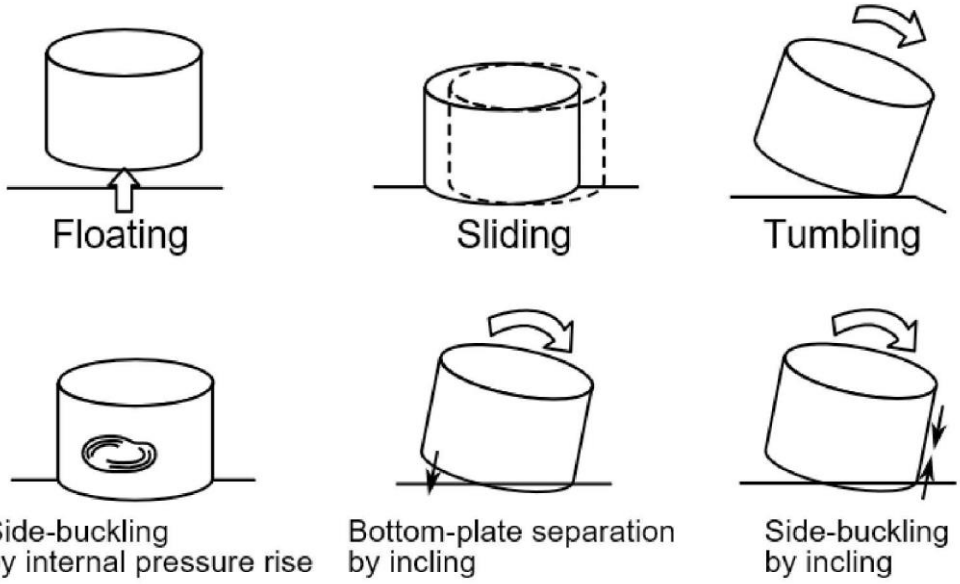

Fig. 2.6 Damage patterns of oil storage tanks during tsunami (FDMA, 2011)

The tsunami-induced oil-storage tank damage patterns according to FDMA (2011) handbook are shown in Fig. 2.6. Most patterns are caused by the tank motion due to floating, sliding and tumble. Hatayama (2014) predicted the tank motion and damage by probabilistic approach based on the inundation depth data and tank movement survey data (FDMA, 2011). This approach could predict tank movement with a reliable accuracy while every mis-prediction was a safe error.

On the other hand, FDMA (2011) proposed safety criteria on the tank movement which was over-predicting with every mis-prediction as a safe error. Kyaw (2017) improved the criteria to predict the tank motion more accurately from the experimental results.

2.3 Conclusions

In this chapter, reviews are made on some of the previous works on the tsunami countermeasures including traditional breakwater types, nature-inspired methods and sophisticated approaches such as flap-gate wave-breaker and buoyancy driven piling systems, discussing the effectiveness and weaknesses of each countermeasure in a general point of view. Then, experimental and numerical modelling of tsunami flows as well as prediction of tsunami load on coastal structures are reviewed. From the past results, RANS with VoF method showed promising results in modelling the tsunami for laboratory scales. For full-scale modelling, nested mesh approaches such as STOC are advantageous. Finally, different oil tank motions under the tsunami flow are reviewed. This gives insights into the prevention of such motions by the application of countermeasures. Overall, these previous researches can be used as a basement in considerations for the experiments and simulations concerning with tsunamis as well as evaluating the effectiveness and feasibility of newly developed tsunami countermeasures.

Chapter 3

Overview of flexible pipes

In this chapter, the overview of the flexible pipes system will be explained with detail explanation on the design parameters being considered.

3.1 Operation principle of flexible pipes

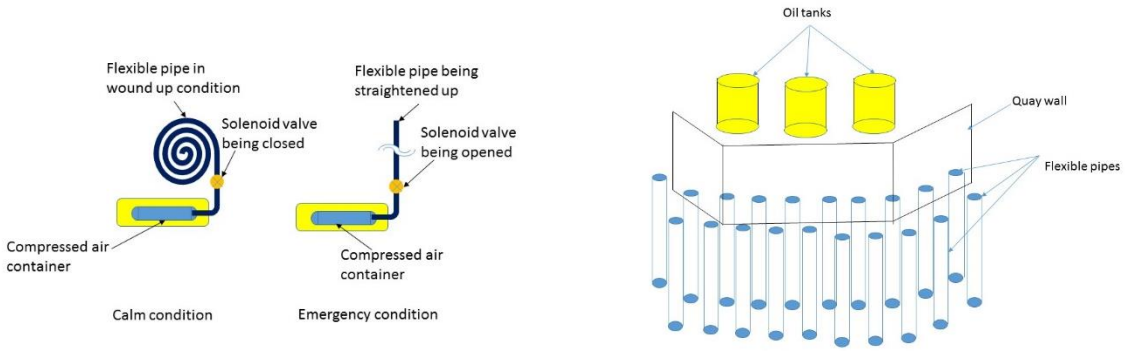

(a) (b)

Fig. 3.1 (a) Operation of flexible pipes in calm condition and emergency condition (b) An example of flexible pipes arrangement in front of oil storage tanks

As briefly explained in Chapter 1, flexible pipes are large diameter pipes wound up and connected to compressed air source which would support the pipes with enough pressure to get straightened up in emergency conditions (Fig. 3.1a). Several hundreds of pipes can be used together to protect the oil storage tanks together with other tsunami protection systems such as quay walls or breakwaters as shown in Fig. 3.1b.

Fig. 3.2 shows the side view of such arrangement showing the design length of the pipes and the design tsunami heights. According to the report from Central Disaster Prevention Council (CDPC, 2012), the tank will take no severe damage if the tsunami wave height is less than 6m (if the inundation height is less than 3m), provided that the tank is not nearly empty. If the wave height is between 6m and 10m (or the inundation height is less than 5m), the tank motion as well as pipe line damage will occur leading to minor or major oil-spill from the pipe line or from the tank motion. If the wave height is more than 10m (or the inundation depth is more than 5m), the oil tank will take serious damage and/or tumble leading to major oil-spill. On the other hand, if the oil tank is nearly empty, it can easily be floated and drifted along the tsunami leading to a minor oil-spill even when 6m tsunami attack occurs. For the Osaka Bay scenario, the length of the flexible pipes was defined to be 15m because the maximum tsunami wave height numerically predicted is 6m (Kyaw, 2017).

For the tsunami having 6m height, it is expected that the flexible pipes reduce the inundation depth below 3m, protecting the oil tank as well as pipelines. For 10m tsunami waves, the flexible pipes need to reduce the inundation depth below 5m, protecting either full tanks or nearly empty tanks from serious damage.

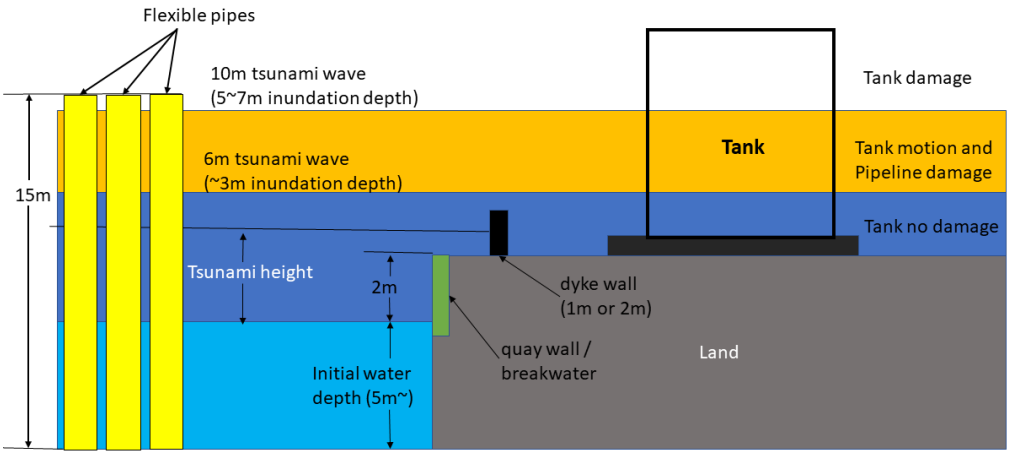

Fig. 3.2 Side view of flexible pipe arrangement with the oil storage tank, dyke wall and quay wall showing the design tsunami height (Adapted and modified from CDPC, 2012)

3.2 Deployment mechanism of the pipes

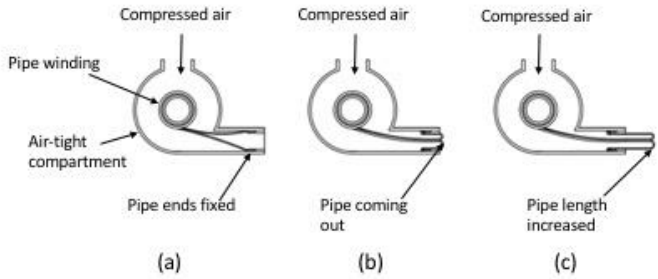

Fig. 3.3 Pipe deployment mechanism

The flexible pipe deployment mechanism is shown in Fig. 3.3. First, the pipe is wound up and one end of the pipe is fixed using a jacket. Then, compressed air is injected into the system. The pipe turns inside out and comes out of the jacket. This machine can unroll pipes for several hundred meters.

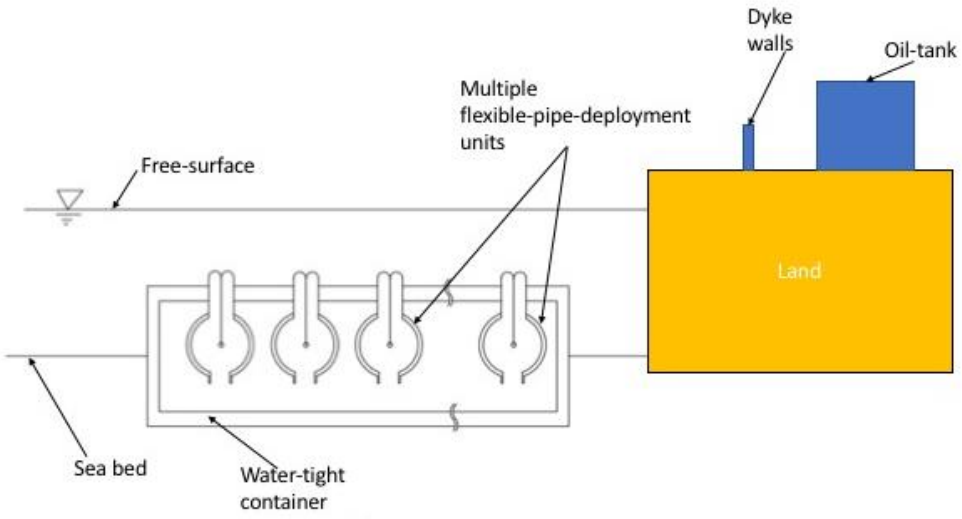

Fig. 3.4 Multiple flexible pipes deployment arrangement

Fig. 3.4 shows the imagination of flexible-pipe-system implementation. A water-tight container will be constructed by the construction of a deep foundation on the sea bed. Multiple flexible-pipe-deployment systems shown in Fig 3.3 will be installed inside this container. When the tsunami alarm comes off, the air pressure in this container would be increased by

injecting high-pressure air or water using an electrical pump or by means of the water pressure of the tsunami. In this way, the flexible pipes would be available for protection when tsunami attacks occur.

3.3 Bending stiffness (EI) of flexible pipes

Fig. 3.5 Fire-hoses having different diameters used in bending stiffness measurements (40mm, 65mm and 100mm diameter)

In the approach of tsunami attenuation presented in this thesis, flexible structures were employed instead of rigid structures in other tsunami countermeasures. Thus, it is important that the flexible pipes have enough bending stiffness (EI) to withstand a Level 2 tsunami without extreme deformations since excessively large deformations would lead to kink or non-linear buckling problems. Therefore, it is important to estimate the EI of full-scale flexible pipes and to choose the design parameters that can give enough EI values.

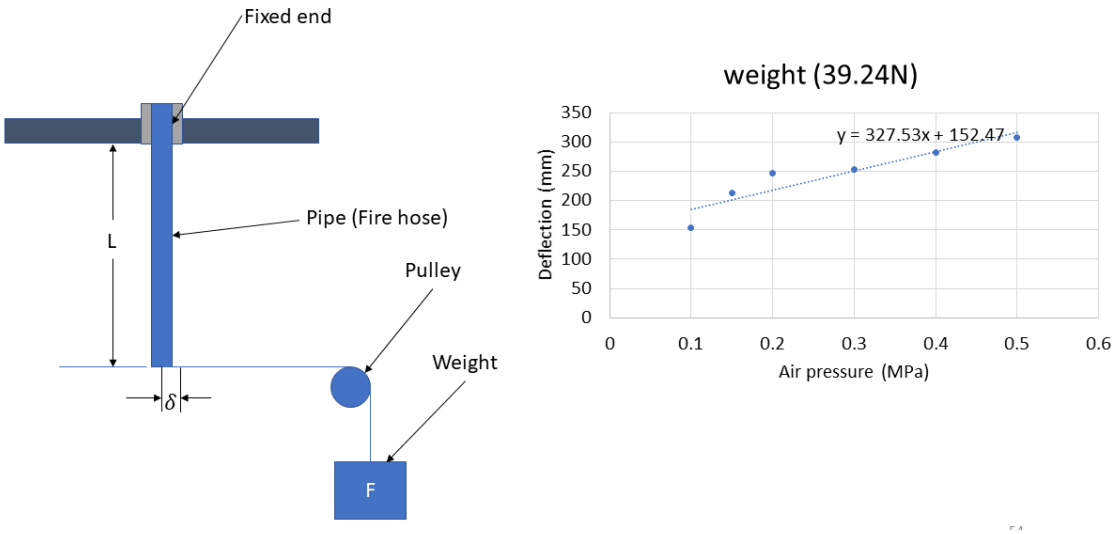

(a) (b)

Fig. 3.6 Experiment for measuring the bending stiffness of double jacket fire hose (a) Cantilever beam assumption (b) Measurement results

Okubayashi (2014) and Nagai (2016) measured the bending stiffness (EI) of 0.1 m diameter double jacket fire hoses which are filled with compressed air of 0.1, 0.2, 0.3, 0.4 and 0.5 MPa pressure assuming that the pipe is a cantilever beam (Fig. 3.6a). In this experiment, the firehose was fixed at one end and attached to a weight by a pulley system as in Fig. 3.6a. By measuring the deformations, EI can be calculated as:

$$\mathrm{EI} = \frac{F_{tip} L^3}{3\delta} \tag{3.1}$$

Where, EI is the bending stiffness (Pa.m^4), F_{tip} is the load applied at the free end of the pipe (N), L is the length of pipe (m) and δ is the deformation of the pipe at the free end (m). In these experiments, L=1 m was used.

One of the results of this experiment is shown in Fig. 3.6b. The bending stiffness (EI) measured for the pipe with 0.1MPa inside pressure was around 152.95Pa m^4. The moment of inertia of a cylindrical structure can be calculated as

$$I = \frac{\pi D^4}{64.0} \quad (3.2)$$

,where D is the diameter of the structure.

However, since the thickness and material of the pipe alone is the same for both scale-model and full-scale pipes. Thus, the relationship between pipe diameter and EI can be expressed as:

$$EI \propto D^3 \quad (3.3)$$

With the assumption that the variation of Young's modulus (E) with the pipe diameter is negligible, the bending stiffness of full scale pipes were estimated. It is assumed that the Young's modulus depends mainly on the inner pressure of the pipe. The interpolation results of EI for 0.2 MPa inner pressure as shown in Table 3.1.

Table 3.1. Estimated bending stiffness of full-scale flexible pipes

Diameter (m)	Inner pressure (Gauge) [MPa]	Inner pressure (Absolute, 10m depth) [MPa]	EI [MPa.m^4]
1	0.2	0.1	0.153
1.5	0.2	0.1	0.516
2.0	0.2	0.1	1.224

3.4 Proposed specifications for flexible pipes

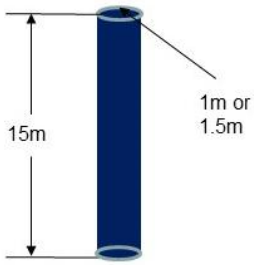

Fig. 3.7 Design dimensions of flexible pipe

The specifications for the flexible pipes were defined by considering the following requirements

1. The length of the pipe should cover the total water elevation including the height of a Level 2 tsunami wave and calm water depth.
2. The bending stiffness of the pipe should be able to withstand the hydrodynamic loads caused by flow velocities corresponding to a Level 2 tsunami.
3. The inner air pressure of the pipe should not be higher than 0.2 MPa , according to the rules of Japan. However, for water injected pipes, more than 1.0 MPa pressure is allowed.

By considering the first requirement, the proposed length of each pipe was 15 m, as illustrated in Fig. 3.7. From the third requirement, the inner pressure for air was defined as 0.2 MPa. For water injected pipes, 1.0MPa pressure was considered. 3 pipe diameters were proposed: 1.0 m, 1.5 m and 2.0 m diameter pipes. The EI values of these cases are estimated as expressed in Table 3.1. Analysis on the deformation of these pipes will be presented in Chapter 7, discussing the feasibility of these design specifications. In Chapter 5 and 6, the effectiveness of these pipes will be investigated by means of experimental approach at various conditions.

3.5 Conclusions

In this chapter, overview of the flexible pipes is presented including a general explanation on the installation and deployment of the pipes. Then the specifications of the flexible pipes are proposed based on the basic requirements for successful implementation and installation of flexible-pipe-system for tsunami attenuation. Analyses on the effectiveness and feasibility of the proposed specifications will be conducted in the later chapters.

Chapter 4

Experimental Setup and Equipment

In order to experimentally investigate the effectiveness of flexible pipes in reducing the wave energy carried by the tsunami, scale-model experiments were carried out in the tsunami wave flume at Osaka University. The detailed features of the wave flume and the measurement devices are explained in Section 4.1 while the specifications of scale-model flexible pipes and energy storage tank are explained in Section 4.2 and 4.3, respectively.

4.1 Tsunami wave flume and measurement devices

4.1.1 Tsunami wave flume and wave generation

Tsunamis are long period shallow water waves with periods of up to several hours. Thus, it is very difficult to scale down the tsunami with its period. Instead, long-period tsunami-like waves are generated by various wave generators including flap type wave generator, plunger type wave generator and gate-open method. Experiments were carried out in the tsunami wave flume of Department of Civil Engineering, Osaka University. The principal dimensions of the wave flume are (44m x 0.7m x 0.9m) and the flume consists of two parts: the dam side and the test side. In this wave flume, gate-open method was used to generate the tsunami-like long period wave. This approach is suitable for tsunami experiments because this allows the larger scale experiments with smaller scale effect (Ramsden, 1993). The schematics of this wave

flume is shown in Figure 4.1. Firstly, the water-tight gate was closed and water is filled into the reservoir side to create a water column of Δh (m) height. The test site of the tsunami tank consists of two slopes: 1/40 slope and 1/100 slope as shown in Fig 4.1. The flexible pipes were placed at 16.8m point measured from water-tight gate (x = 0).

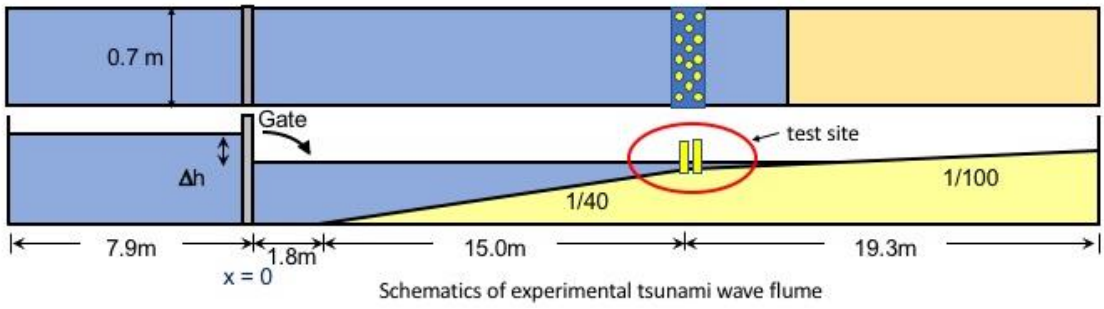

Fig 4.1 Schematics of flexible pipes and tsunami wave flume

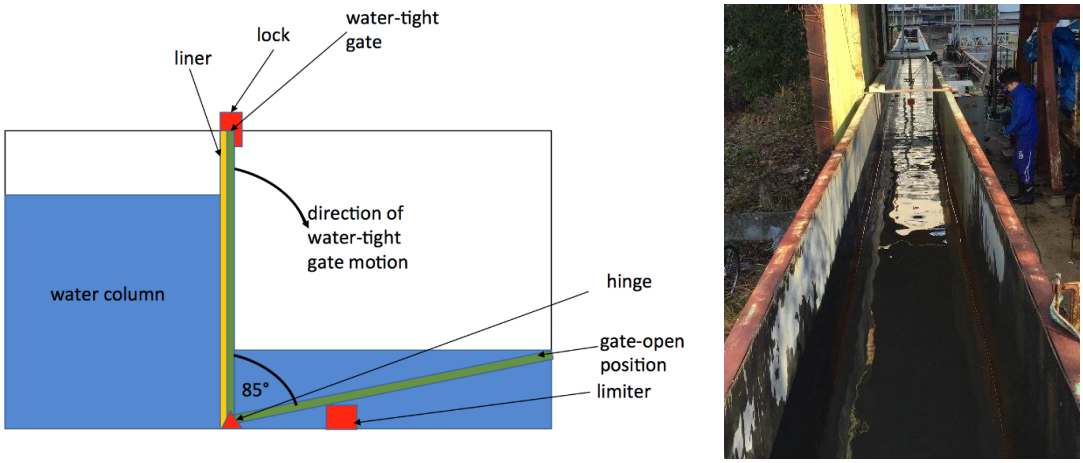

(a) (b)

Fig 4.2 (a) Detailed diagram of gate-opening mechanism (b) photo of tsunami wave flume

When the gate is opened, it rotates in the direction shown in Figure 4.1 due to the static pressure of the water column on the reservoir side. Detailed gate-opening mechanism is shown in Fig 4.2a. The water-tight gate is attached to the base of the wave flume by means of a mechanical hinge. To create the required water column in the dam side, the gate is closed by attaching it to the wave basin top using a lock. After filling water into the dam side, the water-tight door is

opened by opening the lock. The gate rotates about the hinge due to the water pressure on it by the dam side. It rotates for approximately 85 degree until it reaches the motion limiter at the basin floor. This combined flap-dam break method can create a pseudo-tsunami wave that contains a high wave head caused by flapping motion, followed by the mass of water by dam break phenomenon. The overview of the tsunami wave flume is shown in Fig. 4.2b.

Figure 4.3a shows the elevation of a sample wave measured from the free surface by the wave gauge WG01 placed at 6 m from the water gate (x=6, referring to Figure 4.1). The wave is a flow of a massive amount of water a long period wave which is made up of multiple small waves as in Figure 4.3a. According to the measurements at WG01 sensor shown in Figure 4.3b, the period of the incident wave is around 6 seconds. This period is too short for a tsunami experiment. However, in this study, the reduction of transient wave force was considered rather than the steady drag force. Kato, Suzuki and Takeuchi (2014) carried out experiments to investigate the reduction of quasi-steady hydrodynamic force by flexible pipes using uniform flow in a circulating water tank. Therefore, experiments were carried out to test the transient wave force reduction and the incident wave is appropriate for this purpose.

The highest point of this incident wave occurred at the first wave due to the flapping motion of the water-tight gate and its height was observed to be around 0.12 m. As the wave run-up occurs at the 1/40 slope, the wave height gradually increased and finally, wave breaking of the head wave was observed. After the wave breaking, the wave becomes a turbulent bore (Figure 4.3b).

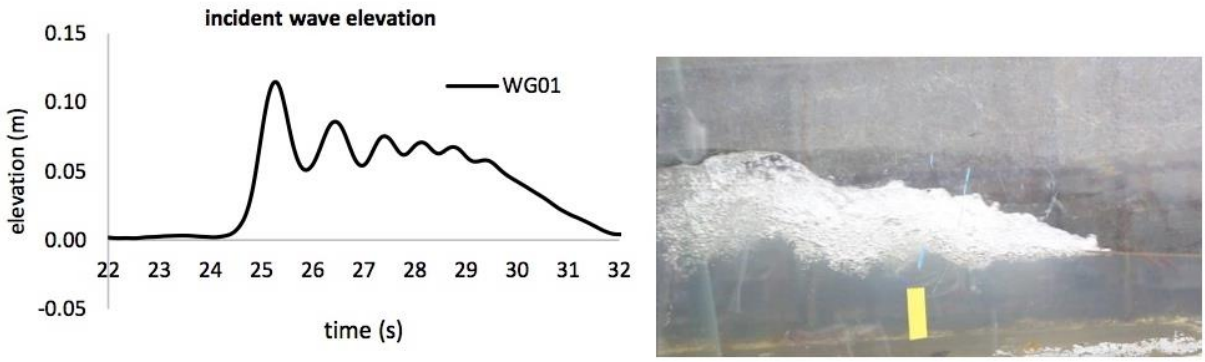

Fig 4.3 (a) Elevation of a sample wave (b) Formation of turbulent bore after wave breaking

4.1.2 Velocity measurement equipment

Two electromagnetic velocity transducers (ACM3-RS transducers) were used to record the unsteady flow velocity in front of and behind the flexible pipes during the wave run up. In Fig. 4.4a, the close-up view of this electromagnetic velocity transducer is shown while the actual setup in the experiment is shown in Fig. 4.4b. It is necessary to initially immerse these sensors by approximately 1cm below the calm free-surface in order to obtain reliable measurements. These sensors are are connected to the personal computer via a digital interface device shown in Fig. 4.5a and 4.5b. The output of the velocity transducers are fed to the interface. This interface can take velocity data from 4 velocity transducers at the same time. However, only 2 transducers were used in the experiments. The outputs of the interface are shown in Fig. 4.5b. The RS-232C serial output from the interface is connected to the computer by RS-232 to USB adapter. The analog output from the interface is used to synchronize the velocity sensors with the force transducer and wave gauges.

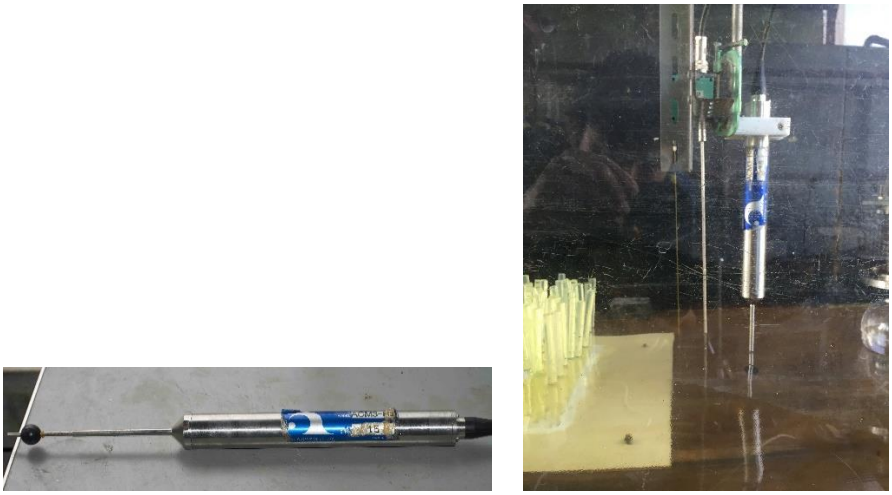

Fig 4.4 (a) Electromagnetic velocity transducer (b) Velocity transducer setup in the experiment

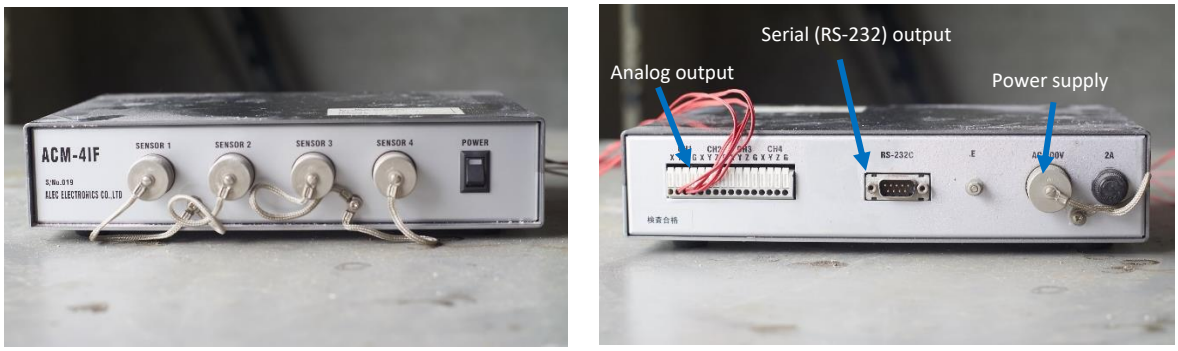

Fig. 4.5 Velocity transducer interface (a) front side, (b) back side

4.1.3 3-component force transducer

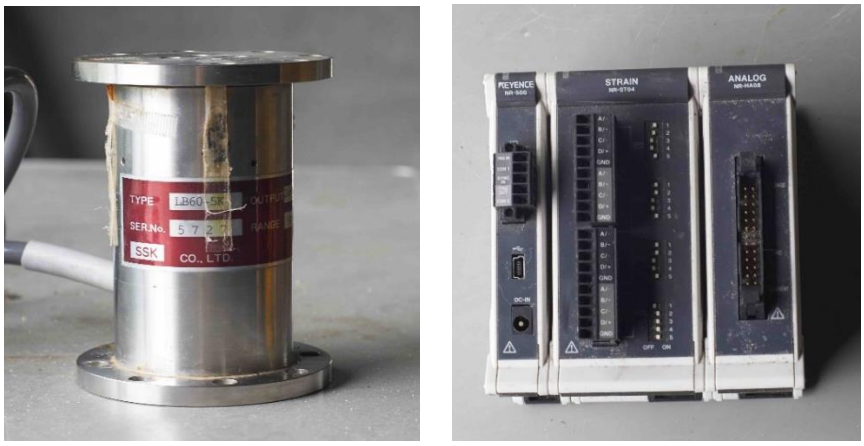

Fig 4.6 (a) 3-component force transducer (b) force transducer interface showing the wiring

The force transducer (shown in Fig. 4.6a) is used to measure the unsteady hydrodynamic force acting on the scale-model oil tank by the tsunami wave. It is a load cell type transducer which can measure translational forces in a three-dimensional coordinate system, i.e., in x, y and z directions. The load cell is connected to a separate interface system (Fig. 4.6b) through which the force data is transformed into electric voltages and fed to the personal computer for recording.

The interface is composed of three parts shown in Fig. 4.6b: NR-500 for the power supply and the data transfer between the interfaces and computer, NR-ST04 for the strain data of the load cell and NR-HA08 as the analog data receiver unit.

Fig. 4.7a Force transducer calibration arrangement

Force transducer calibration was carried out by using the setup shown in Fig. 4.7a. 100g, 200g and 500g weights were placed inside the balance attached to the force sensor by means of a thin rope via a pulley as shown in Fig. 4.7a. The masses of the pulley and rope were neglected. The results of the force sensor calibration are shown in Fig. 4.7b. From this result, the force transducer calibration coefficient was estimated to be 1.1594 kg/volt.

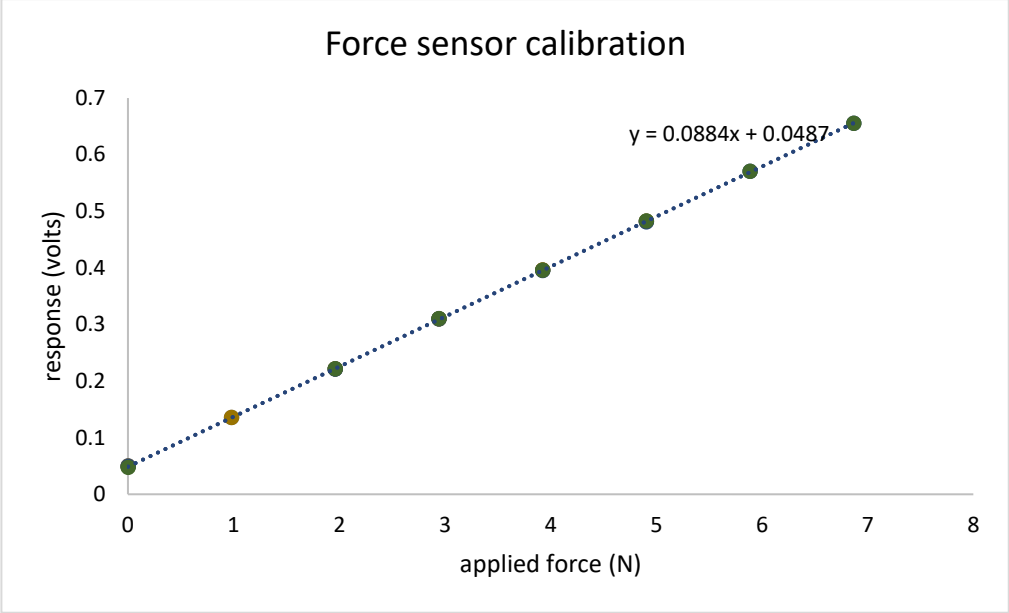

Fig. 4.7b Force transducer calibration results

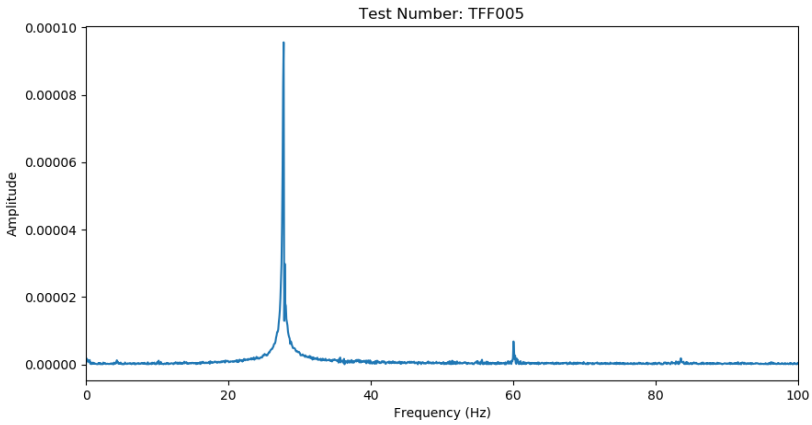

Fig. 4.8a Free vibration test of force transducer only

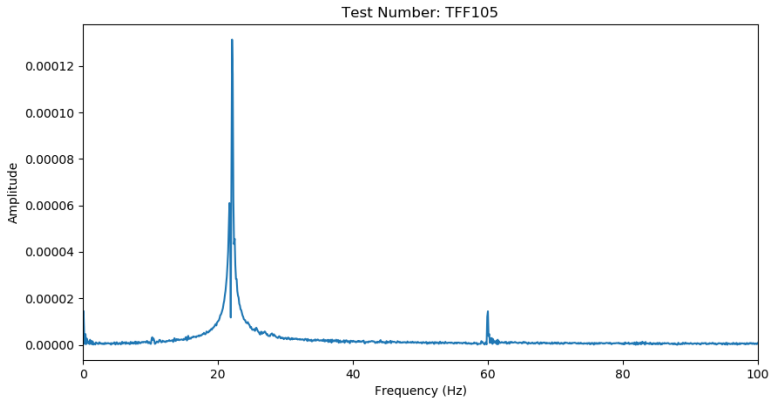

Fig. 4.8b Free vibration test of force transducer attached to cylindrical tank

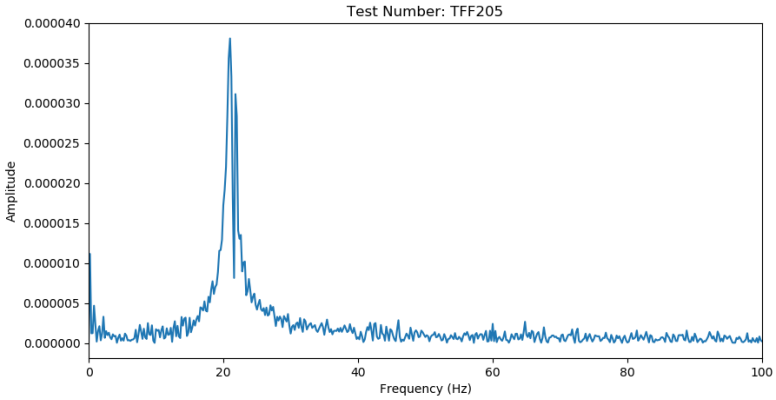

Fig. 4.8c Free vibration test of force transducer attached to spherical tank

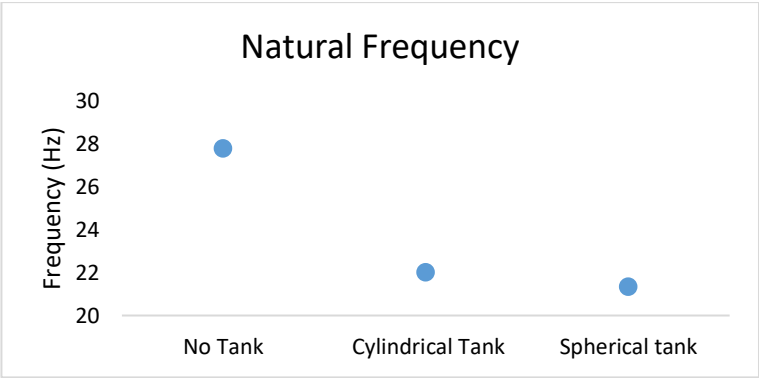

Fig. 4.8d Summary of natural frequencies for force measurement setup

The free vibration tests were carried out with three conditions: no oil-tank attached to the force sensor (TFF001 to TFF010), cylindrical tank attached to the sensor (TFF101 to TFF110) and

spherical tank attached to the sensor (TFF200 to TFF210). The force measurement mechanism (which includes the beams on the tank top, the metal rod and force sensor) is attached to the tsunami wave flume using lobster jaws. Then an impact load is given to the force sensor. For the case with oil-tank attached to the sensor, impact load is given to the tank. The sampling rate for the force data is 10kHz (10,000 samples per second). The sampling time is between 30 and 50 seconds, resulting in 300,000 to 500,000 data points for each test. After each test, 3-minute-waiting time was made before starting another test so that the residual vibrations disappear. This test was carried out 10 times and the FFT was taken by a python program. The results of these tests are shown in Fig. 4.8a, 4,8b and 4.8c.

Since the sampling frequency is 10kHz, the FFT results ranged up to 5kHz. However, the frequencies beyond 100Hz are insignificant and thus, irrelevant for further analysis. Thus, the frequencies up to 100Hz is shown in the figures. The mean natural frequency for the first mode of vibration for force sensor alone is 27.7786Hz. The natural frequency for the first mode of vibration for cylindrical tank and spherical tank were observed to be 22.0Hz and 21.33Hz, respectively. The averages of the results are summarized in Fig. 4.8d.

4.1.4 Wave gauges

Three wave gauges were employed in the experiments in which the reduction in water elevation and momentum flux were estimated. Fig. 4.9a shows the close view of one of the wave gauges. The wave gauges are numbered as WG01, WG02 and WG03. The wave gauges are connected to the amplifier (Fig 4.9b) from which voltages corresponding to the water depth are obtained. The amplifier consists of switches to adjust the gain and fine gain of the amplifier. Zero point can also be readily obtained by choosing the AUTO mode provided by this amplifier.

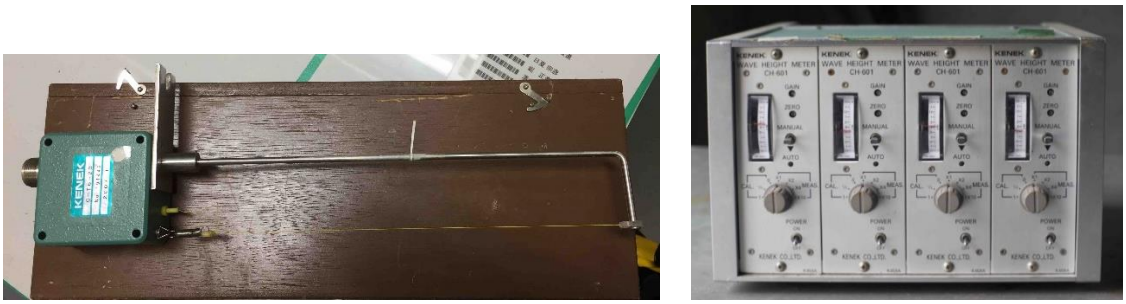

Fig. 4.9 (a) A close view of wave gauge (WG03) showing its container (b) amplifier for wave gauge

The wave gauges were calibrated by changing their immersed depth and recording the voltages in the personal computer. The depth was increased and decreased by immersing and raising up the wave sensor by 1cm at a time. To obtain the best possible calibration results, elevation data was recorded only when the free-surface is calm without apparent oscillations. This was achieved by waiting approximately one minute between each up or down motion of the wave gauge. Three runs of tests were carried out for each sensor and the results are shown in Fig. 4.10 a, b and c. Table 4.1 summarizes the calibration coefficients of these wave gauges.

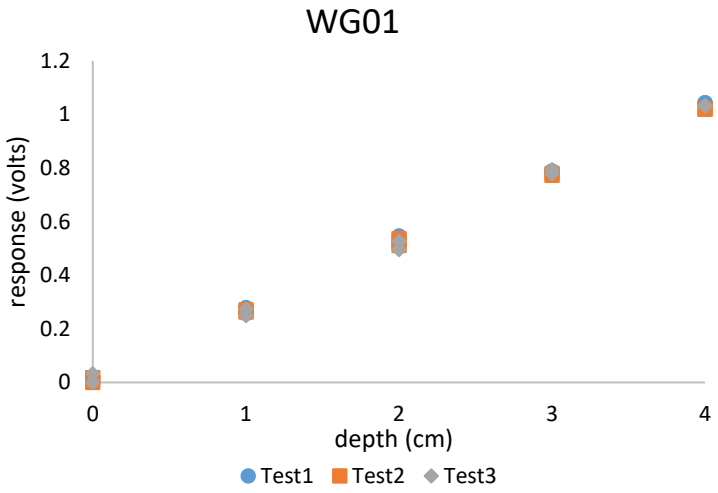

Fig. 4.10a Wave gauge (WG01) calibration results

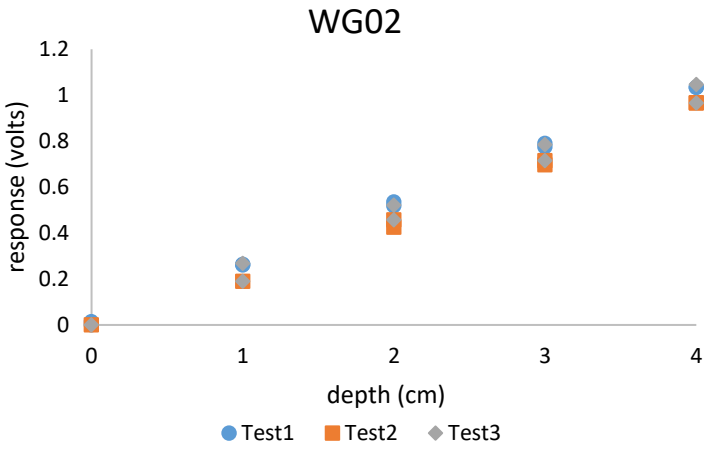

Fig. 4.10b Wave gauge (WG02) calibration results

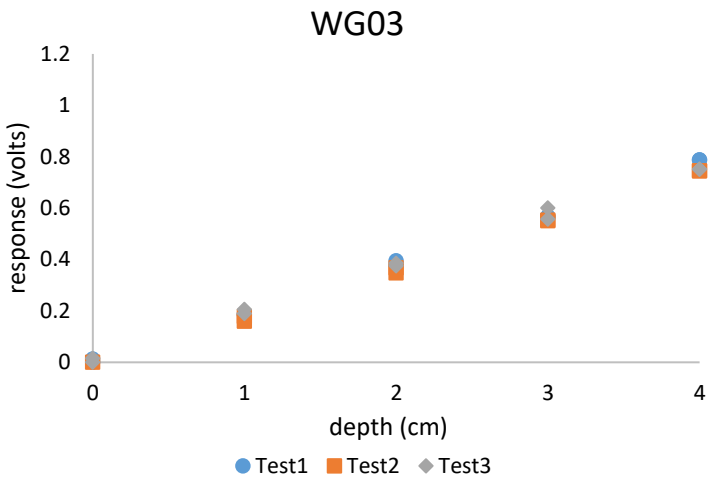

Fig. 4.10c Wave gauge (WG03) calibration results

Table 4.1 Calibration coefficients of wave gauges

Wave gauge	Calibration coefficient (cm/volts)
WG01	3.9202
WG02	3.8862
WG03	5.3769

4.2 Scale model flexible pipes

4.2.1 Comparison of bending stiffness

Three sets of pipes tested in this experiment are shown in Fig. 4.11. The pipes of 1cm diameter were chosen that represent 1.5m full-scale flexible pipes, while 10cm and 20cm in length were considered to investigate the effect of pipe length on impact reduction. The 10cm long pipes represent 15m long pipes in full-scale, while the 20cm long pipes represent 30m long pipes. However, the 15 m long pipes should be preferable due to easier production and faster inflation using compressed air under the emergency condition.

As shown in Fig. 4.11, 1cm diameter holes were drilled on (30cm x 30cm) wooden boards using a Computer Numerical Control (CNC) machine and the pipes were glued inside the holes. This wooden board arrangement was attached to the base wooden board using nuts and bolts. The effect of the board thickness, nuts and bolts on the tsunami flow are neglected in this experiment.

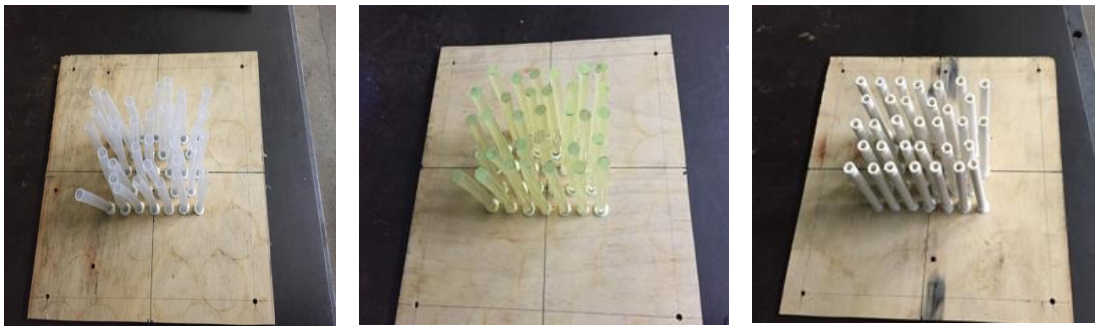

Fig. 4.11 Silicone rubber pipe, urethane rubber pipe and rigid ABS pipes

Table 4.2 Bending stiffnesses of pipes

No.	Type	Bending stiffness, EI (MPa . m^4)
1	Silicone rubber pipe	3.47×10^{-10}
2	Urethane rubber pipe	2.75×10^{-8}
3	ABS pipe	6.96×10^{-7}

Measurements of bending stiffness for silicone rubber pipes and urethane rubber pipes were carried out and the results are shown in Table 4.2. For the ABS pipe, the bending stiffness is relatively high compared to the other types, and therefore in this experiment, these pipes were considered as rigid pipes.

By considering geometric similarity, the relationship between pipe diameter and EI can be calculated using Eq. 3.3 in Section 3.3 with the assumption of constant Young's modulus for both full-scale and model-scale pipes. The bending stiffness of scale model pipes were estimated to be approximately 1.53×10^{-8} if the same material would be used for both full-scale and model pipes. However, it is necessary to choose pipes with lower EI than this estimated value in order to compensate possible scale effects on Young's modulus. Therefore, silicone rubber pipes with 3.47×10^{-10}MPa m^4 were selected to represent full-scale flexible pipes. Pipes with higher EI values were used for comparison.

4.2.2 Arrangement of pipes

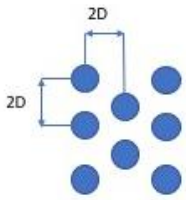

Fig. 4.12 Arrangement of pipes

The distance between the centers of two pipes in a row is 2D where D is the pipe outer diameter. The distance between two consecutive rows is also 2D, as in Fig. 4.12. The porosity (p_n) of the flexible pipe arrangement, in percentage, can be estimated using the following equation on an arbitrary section of the arrangement:

$$p_n = 100\left(\frac{V_v}{V}\right) \tag{4.1}$$

where V_v is the volume of the void in the section, V is the total volume of that section. By using this formula on Fig. 4.12, the porosity of the flexible-pipe-system was approximately 80.4 percent.

4.3 Scale model energy storage tanks

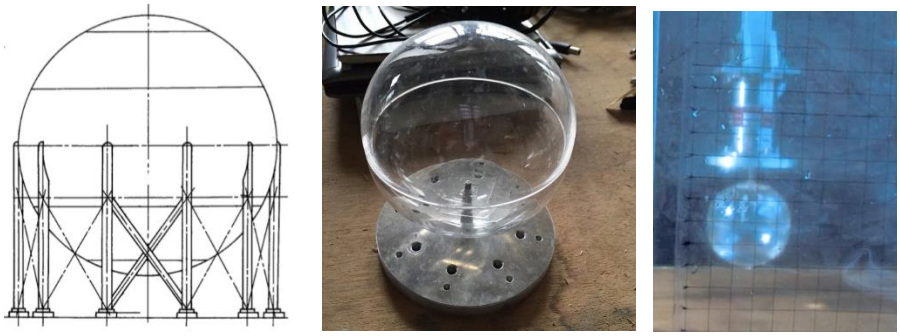

Fig. 4.13 (a) Schematic of full-scale spherical gas tank (b) the scale-model sphere used in the experiment (c) sphere connected to the force transducer

Two types of scale-model tanks were considered in the experiments. The first type is a spherical tank that represents a spherical gas storage tank. Such tanks are supported by metal beams as shown in Fig. 4.13a instead of placing on the ground. In the experiments, the effects of these metal beams were neglected. Thus, the tank was placed approximately 2 centimeters above the calm water free-surface. The scale model sphere was connected to a circular basement by means of a threaded rod (Fig. 4.13b). This basement is connected to the force sensor using 4 pairs of bolts and nuts (Fig. 4.13c).

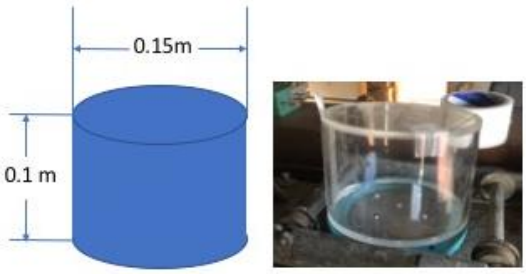

Fig. 4.14 Scale-model cylindrical tank representing a 1767kL oil tank

Table 4.3 Drifted tanks during 2011 Great East Japan Earthquake tsunami (Hatayama, 2014)

Capacity (C) Class (m^3)		$C < 500$	$500 \leq C < 1,000$	$1,000 \leq C < 10,000$	$10,000 \leq C < 50,000$	$50,000 \leq C$	Un-known	Sum
By Capacity Class		110	30	16	1	0	0	157
By Prefecture	Aomori	3	0	0	0	0	0	3
	Iwate	40	4	0	0	0	0	44
	Miyagi	55	19	14	1	0	0	89
	Fukushima	12	7	2	0	0	0	21

The second type of tank is cylindrical tank which represents a medium size cylindrical oil tank which can store 1767kL of oil in full-scale. Such tanks were observed to have drifted during 2011 Great East Japan Earthquake tsunami according to the data tabulated by Hatayama (2014), as described in Table 4.3.

4.4 Conclusions

In this chapter, the details of the experimental equipment are explained, including the tsunami wave flume, sensor calibration and scale model flexible pipes and oil and gas tanks. Tsunami wave flume can generate long period tsunami-like bores, provided that the scale is not larger than 1:100. By carrying out calibrations of the sensors, the experimental equipment can give reliable experimental data which is useful in estimating the full-scale phenomena to a certain extent.

Chapter 5

Analysis on the effectiveness of flexible pipes based on material and orientation

As explained in Section 3.1 of Chapter 3, flexible structures that can be wound up are proposed as one of the methods for tsunami mitigation. Consequently, flexible pipes shall be employed in this approach instead of rigid ones. Therefore, it is necessary to compare the effectiveness in tsunami load reduction of different materials possessing different material properties. In the first part of this chapter, experiments were conducted in tsunami wave basin and results will be presented. The purpose of these experiments is to investigate the effect of bending stiffness (EI) on the reduction of unsteady flow velocity and tsunami force acting on energy storage tanks. To achieve this purpose, in this chapter, comparisons will be made on the experimental results of flow velocity and hydrodynamic force reduction by 3 different materials having different EI values. Moreover, the effect of material properties of the pipes on the detail flow features will be qualitatively assessed using videos taken with high-speed camera.

In the second part, the numerical analysis using CFD was conducted with the assumption of rigid pipes. The purpose of these simulations is to investigate the flow around the pipes in higher details and to estimate the relationship between the width of flexible pipe arrangements and reduction of hydrodynamic forces. CFD results were validated against the experiment results and estimations of force reduction were made for different widths of pipe-arrangement.

5.1 Experimental setup

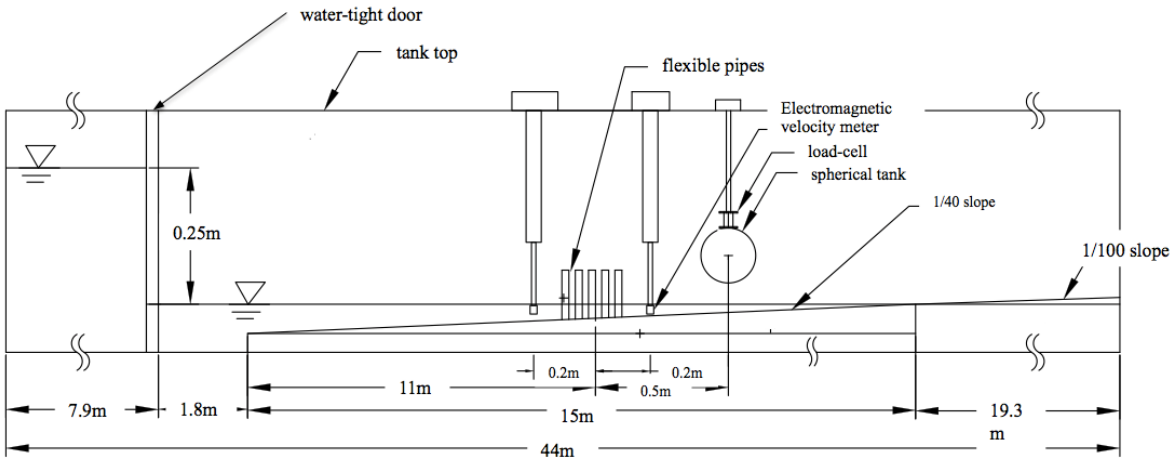

Fig. 5.1 Side view of the general arrangement of experimental setup

The general arrangement of the experimental setup is shown in Fig. 5.1 while the photo showing the details of the experiment is shown in Fig. 5.2. As explained in Section 4.1.1 of Chapter 4, the total length of the tsunami wave basin is 44m while the diameter of the spherical tank used in the experiment is 0.1m (10cm). The difference of water level between reservoir and the experimental tank was set at 0.25m (25cm). Thus, in order to show the whole experimental arrangement focusing on the flexible pipes and the tank model, the schematic in Fig 5.1 is drawn using a different scale ratio for the object dimensions of the flexible pipes and the tank model.

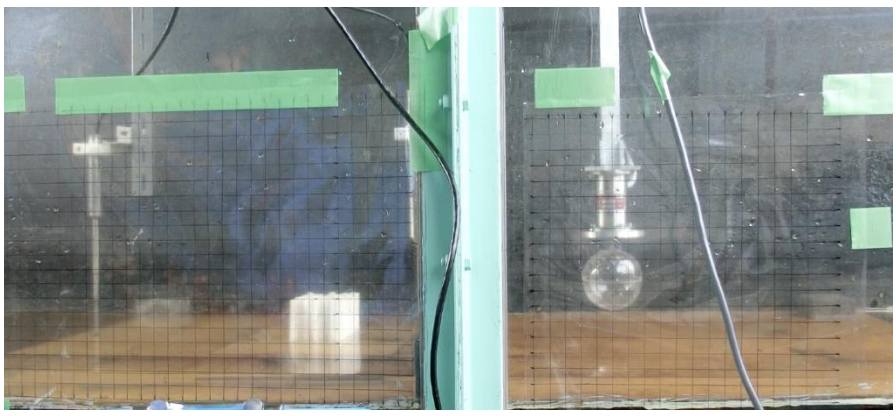

Fig. 5.2 Photo of the experimental setup showing the pipes and spherical tank

The wave was generated by creating a water column on the dam site and manually opening the watertight door. Before opening the watertight door, the water depth in the reservoir side was set at 0.65m whereas the water depth at the other side of the water gate was 0.4m, such that the water column of 0.25m was formed. The surface elevation and flow velocity of a sample wave is shown in Fig. 5a and 5b, respectively. The frequency spectrum of the sample wave is shown in Fig. 5c. From this figure, the frequency of the wave is 0.146 Hz.

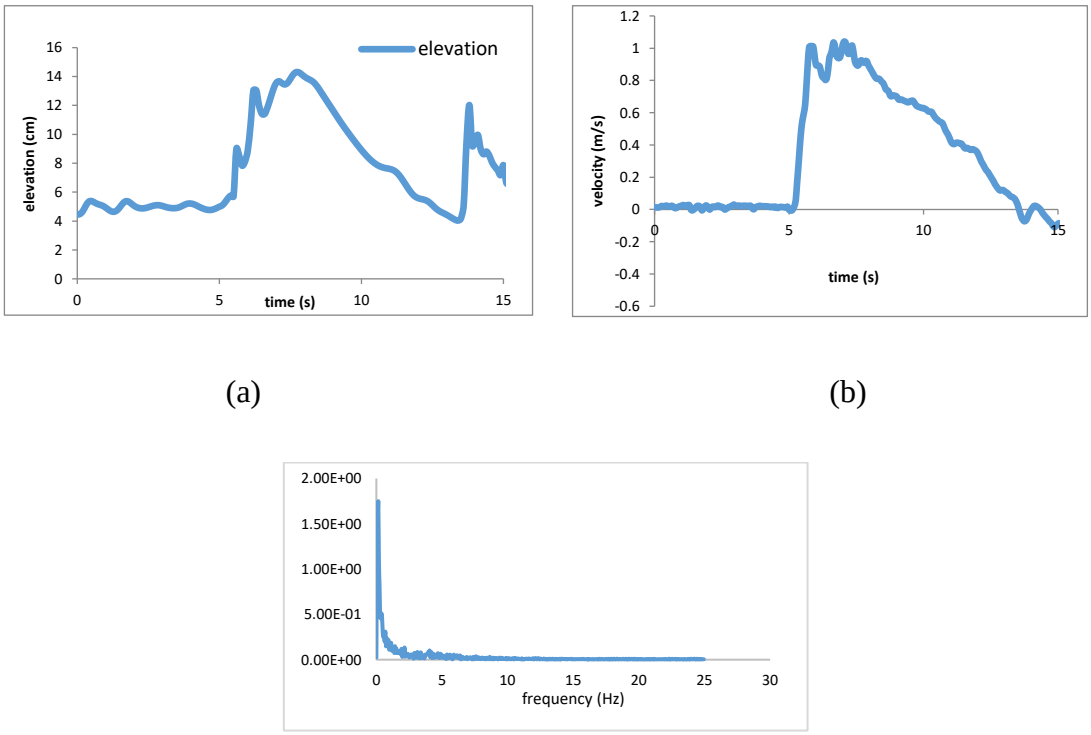

(a) (b)

Fig. 5.3 Measurement results of a sample wave (a) water surface elevation (b) velocity (c) frequency of wave

The pipe location was determined so that the water depth at the pipe location was 0.05 m. Since the pipe length of this study was 0.1 m (10 cm), half-length of the pipes were underwater in the calm condition. The electromagnetic velocity meters were attached at 0.2 m in front of and behind the pipes, respectively. The sampling frequency of both velocity meters were set at 20Hz. The measurement points of the velocity meters were placed 0.02m below the free-surface of calm water condition. The 3-component force transducer presented in Section 4.1.3

was used to measure the hydrodynamic force acting on the spherical tank attached to it. Sampling frequency of force transducer was configured to be 20Hz in order to have the same sample rate as the velocity transducers. The water depth at the scale-model tank was set as 0.02 m (2 cm) while the gap between the water surface and the bottom of the scale-model oil tank was set as 0.02 m (2 cm) above the free-surface.

In actual case, the oil-tanks are supported by pipe braced frames. However, in this study, the buoyant forces by the tsunami flow were not considered. Therefore, only the hydrodynamic forces in the in-flow direction on the oil tank model were investigated, neglecting those on pipe braced frame. Thus, the oil tank model was fixed by a supporting rod in air.

As explained in Section 4.2 of Chapter 4, three types of pipes with different Young's moduli were tested: silicone rubber pipes, urethane rubber pipes and ABS pipes. For the ABS pipe, the bending stiffness is relatively high compared to the other types, and therefore in this experiment, such pipes were selected to represent the rigid pipe. Various parameters of pipes and tanks are listed in Table 5.1.

Table 5.1 Experimental conditions with different materials and orientations

Case	Type of pipes	Pipe length	Number of pipes	Type of tank
Case 1	No pipes	-	-	Sphere
Case 2	Silicone rubber	10cm	33	Sphere
Case 3	Urethane rubber	10cm	33	Sphere
Case 4	ABS (rigid)	10cm	33	Sphere
Case 5	Silicone rubber	20cm	53	Sphere
Case 6	Urethane rubber	20cm	53	Sphere
Case 7	ABS (rigid)	20cm	53	Sphere
Case 8	No Pipes	-	-	Cylinder
Case 9	Silicone rubber	20cm	53	Cylinder
Case 10	Urethane rubber	20cm	53	Cylinder
Case 11	ABS (rigid)	20cm	53	Cylinder

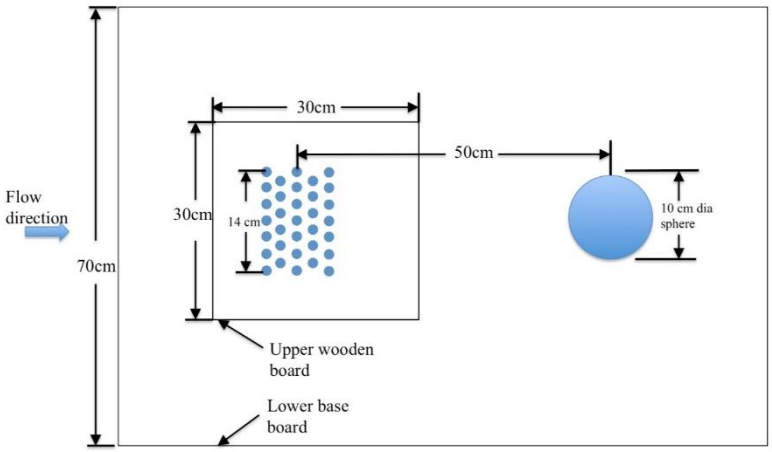

Fig. 5.4 Top view of experimental setup using flexible pipes and spherical tank showing the placement of the pipes on the base

The plan view of the 33 pipes case is shown in Fig. 5.4. The number of pipes in the cross flow direction is 7 and 6 alternatively forming 5 rows of pipes, totalling 33 pipes. The width of the 33 pipes arrangement can cover the cross-sectional area of the sphere while this arrangement cannot cover the cylindrical tank. Therefore, in order to cover the width of the cylindrical tank, the pipes assembly consisting of 11 and 10 pipes in each row were used for the cylinder cases. These arrangements were made of 53 pipes. Only the spherical tank was employed for the 33 pipes case, whereas both sphere and cylinder were tested for the 53 pipes case.

Okubayashi (2014) conducted experiments on the velocity reduction of flexible pipes by measuring the time-averaged velocity inside the wake field behind flexible pipes. In his work, the pipes with EI values similar to urethane pipes in Case 3 were used. Tar (2015) carried out 2D CFD simulations to compute the wake field behind the pipes arrangements having different numbers of rows and validated the simulation results with Okubayashi (2014). Their works suggested that significant improvements in velocity reduction were not observed when the number of rows of pipes is 5 or more. Thus, in this research, 5 rows of pipes were considered.

5.2 Results and discussions

5.2.1 Flow Velocity

Fig. 5.5 illustrates the velocity measurements in front of and behind the flexible pipes. Since the difference in flow velocity between sphere and cylinder is insignificant, only the velocity profiles for the former are presented. Therefore, Cases 1 – 7 are shown. For the reproducibility, 6 runs of experiments were carried out for each case and means and standard deviations of maximum velocity and forces were calculated. The mean values and errors of the maximum velocity measurements are described in Fig. 5.6a and 5.6b. In these figures, the circles showed the mean value of the maximum velocities obtained from each 6 runs of experiments. The standard deviations are shown as the error bars at the top and bottom of each circle.

In Case 1, no pipes were attached and thus, very similar flow velocities were measured by the two sensors. It was observed that the water velocity in front is marginally larger than that behind it because of the wall effect of the baseboard. For the cases for flexible and rigid pipes, relatively smaller velocities were measured behind the pipes because the decrease in velocity inside the wake behind the pipes was relatively large compared to that outside the wake. However, the velocities outside the wake and near the free-surface might be only slightly reduced.

In Case 2, with flexible silicone pipes, the velocity of the head wave was reduced to 0.4 m/s and this velocity was again reduced to nearly zero, caused by the motion of the pipes in the flow direction as well as in the cross-flow direction. After the impact by the head wave, the flow developed again, which was reduced by the oscillations of the flexible pipes in the cross-flow direction. This phenomenon could be seen as small oscillations in the velocity measurements behind the flexible pipes. The urethane pipes used in Case 3 have higher bending stiffness than silicone pipes and therefore, these pipes also showed slight flow induced motions

in the cross-flow direction. However, urethane pipes did not bend in the inflow direction due to their high EI value. Thus, the velocity reduction was lower than the silicone pipes case. The velocity results of rigid pipes are shown in Case 4. Wave breaking occurred at the rigid pipes and thus, the initial velocity was significantly reduced by this arrangement. After the wave breaking, the flow recovered and the velocity increased to 0.5 m/s.

The 20 cm long pipes are tested and the results are shown in Cases 5, 6 and 7. Flexible silicone pipes in Case 5 showed a large amplitude of bending in the inflow direction, compared with the amplitude of oscillatory motion in cross-flow direction caused by vortex induced vibration (Fig. 5.7c). On the other hand, the pipe bending amplitude of the 10 cm long silicone pipes in the flow direction was relatively small compared to the 20 cm long pipes of the same material (Fig. 5.7a). Thus, the velocity reduction by the 20 cm long pipes was smaller than the 10cm silicone pipes because much less flow induced motions of the pipes occurred in the 20cm long pipes compared to the 10 cm pipes.

On the other hand, 20 cm long pipes made of urethane and ABS did not show significant vortex induced vibrations. Instead, the wave height decreased behind these pipes, whereas the wave flowed over 10cm long pipes. Thus, it can be deduced that velocity was reduced equally along the pipe length for longer pipes while the 10 cm long pipes showed very high velocity reductions at the measurement points. In the 10 cm long pipes case, the velocity was significantly decreased inside the wake, while the water passing over the pipes have higher velocities. Therefore, flow velocities measured behind the 20 cm long pipes are higher than those measured behind the 10 cm pipes.

Cases 2, 3 and 4 use 33 pipes, with 7 pipes in each row in the cross-flow direction, while Cases 5, 6 and 7 have 53 pipes with 11 pipes in the cross-flow direction. However, in comparing the 33 pipes case with the 53 pipes case, the velocity inside the wake region behind the pipes did not reduce by increasing the number of pipes in the cross-flow direction.

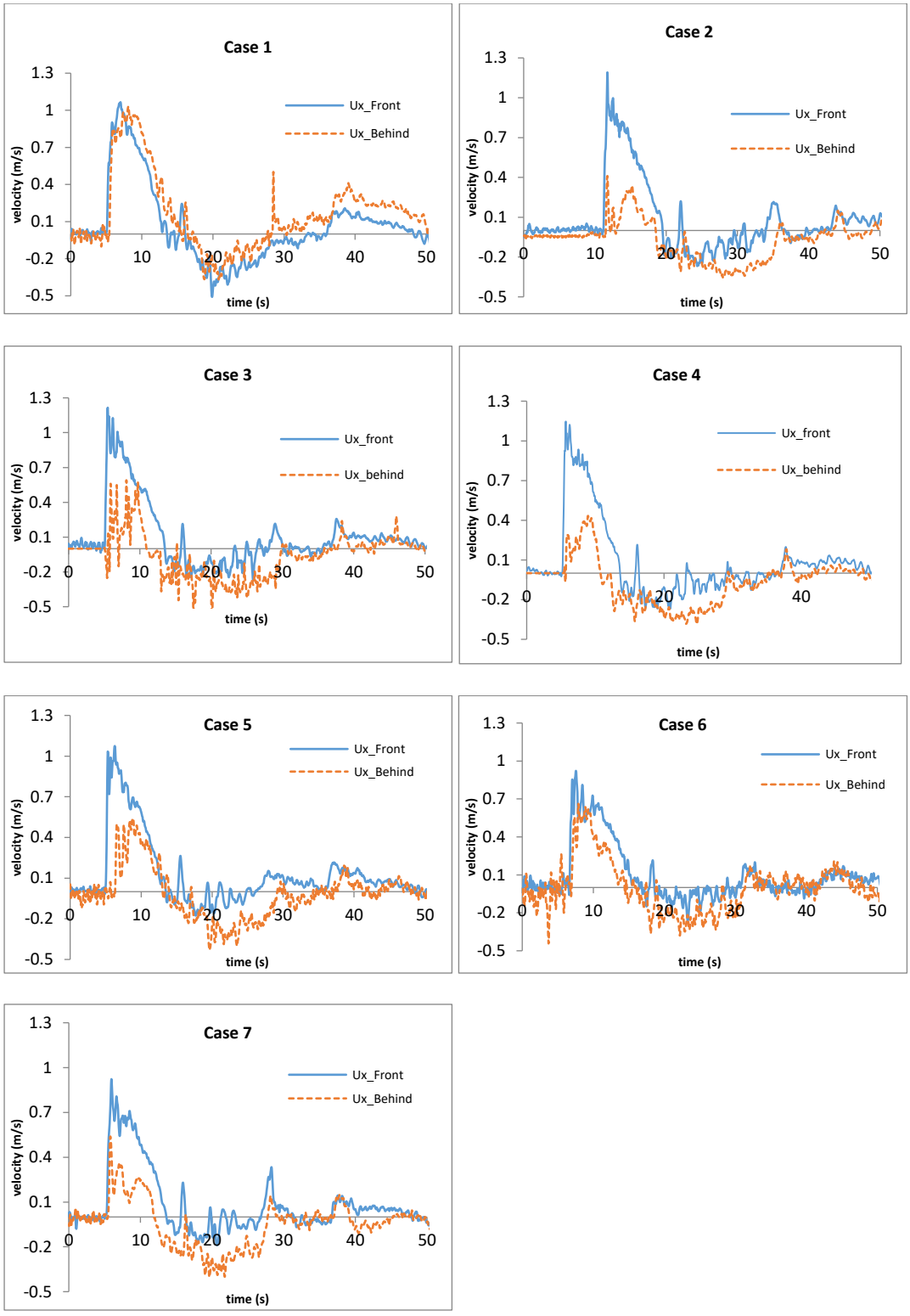

Fig. 5.5 Velocity measurements in front of and behind the pipes: Case 1 (no pipes), Case 2 (33 pipes, Silicone rubber), Case 3 (33 pipes, Urethane rubber), Case 4 (33 pipes, ABS rigid), Case 5 (53 pipes, Silicone rubber), Case 6 (53 pipes, Urethane rubber), and Case 7 (53 pipes, ABS rigid)

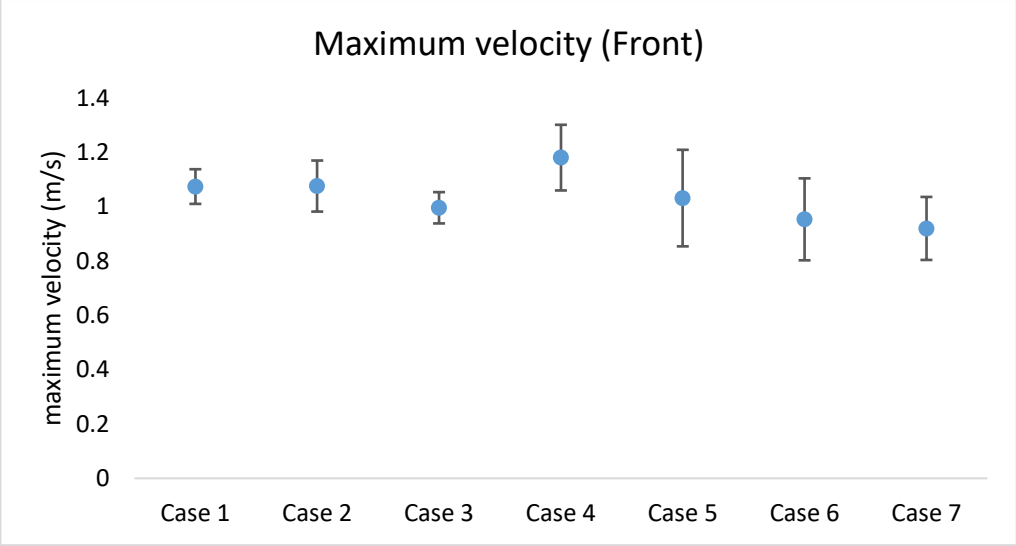

(a)

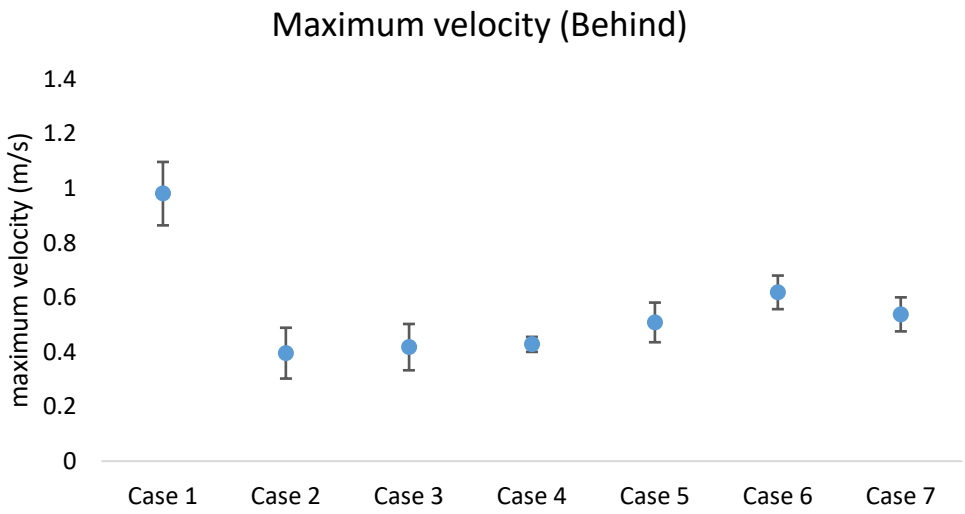

(b)

Fig. 5.6 Mean and standard deviation values of maximum velocities for Cases: 1, 2, 3, 4, 5, 6 and 7 (a) in front of flexible pipes (b) behind flexible pipes

Overall, velocity reduction was caused by energy dissipation due to the drag force of the pipes. For the flexible silicone rubber pipes, this drag was provided by vortex shedding and flow induced oscillations while only vortex shedding was contributed to energy dissipation for more rigid urethane and ABS pipes. Moreover, the velocity measurements behind the pipes were

done inside the wake region. Therefore, as mentioned before, the flows outside the measurement points might have significantly higher velocities than these measured values.

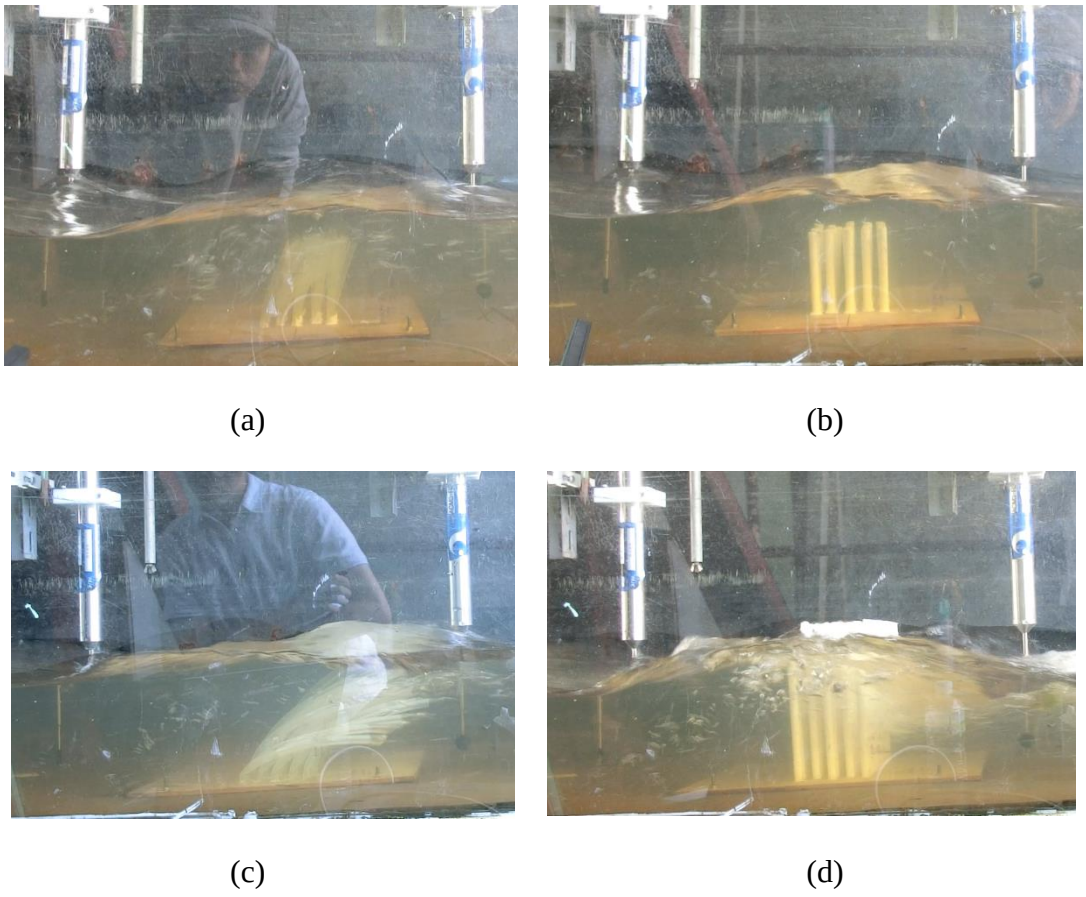

(a) (b)

(c) (d)

Fig. 5.7 Comparison of bending for silicone pipes and rigid pipes under tsunami flow: (a) 10cm long silicone pipes, (b) 10cm long ABS rigid pipes, (c) 20cm long silicone pipes, and (d) 20cm long ABS rigid pipes

5.2.2 Hydrodynamic force on the tanks

The influence of different pipes on the hydrodynamic force reduction is illustrated in Figs. 5.8, 5.10 and 5.13 for the sphere and cylindrical tank, with 33- and 53-pipe arrangements, respectively. Fig. 5.8 shows the comparison of time series of hydrodynamic forces acting on the spherical tank for the cases of 10 cm long pipes as well as no pipes, using the same type of wave. The maximum wave load occurs at the first impact by the tsunami bore. After that peak load, the flow phenomenon is similar to an unsteady oscillatory flow, with varying velocities.

As observed in Case 1 of Fig. 5.8, the peak around 5s shows the impact load by the wave head while the rest part of the force did not show large changes. By the application of flexible pipes, this impact load could be largely decreased as in Cases 2, 3 and 4, by means of wave breaking at the pipes arrangement. Moreover, the drag force caused by the uniform flow could also be greatly reduced by the pipes. There are several small oscillations in the force measurements for silicone pipes in the uniform flow part after the head wave. It is caused by the oscillations in flow velocity due to the vortex-induced motion of these silicone pipes. For pipes with larger bending stiffness, fewer oscillations are observed in the measured forces due to a lack of flow induced oscillations of the pipes. 6 runs of experiments were conducted for each case and the mean values and error were calculated. The mean values of the maximum hydrodynamic forces for Case 1, 2, 3 and 4 are compared in Fig. 5.9.

Force measurements of the spherical tank for 53 pipes, each of 20 cm in length are shown in Fig. 5.10. The force measurements for the 20 cm long silicone pipes in Case 5 showed a minimal difference compared to the 10cm long pipes of the same bending stiffness, because of very large bending amplitudes of pipes under the flow, as shown previously in Fig. 5.7a. Thus, the 20 cm pipes were observed to act as 10 cm pipes for the silicone type and their reduction rates showed a very small difference. Fig. 5.9 shows the mean values of maximum hydrodynamic forces for Cases 5, 6 and 7. These values are compared with the forces measured without flexible pipes (Case 1) in this figure.

The comparison of reduction of the maximum hydrodynamic load is shown in Fig. 5.12a and 5.12b. The reduction of maximum hydrodynamic load is compared between 10 cm and 20 cm pipes. This reduction factor is calculated by the following formula:

$$Force\ Reduction\ (\%) = \frac{F_{no\ pipes} - F_{pipes}}{F_{no\ pipes}} \text{ x } 100 \qquad (5.1)$$

Where,

$F_{no\ pipes}$ = mean value of the maximum hydrodynamic force acting on the model tank for experiments with no pipes and

F_{pipes} = mean value of the maximum hydrodynamic force acting on the model tank for experiments with pipes.

F_{pipes} was calculated for all three types of pipes (silicone rubber pipes, urethane rubber pipes, ABS rigid pipes) from the mean values of the force measurements described in Fig. 5.9 and Fig. 5.11, respectively. The means and standard deviations are shown in Fig. 5.12a for Cases 2 to 7. These values are categorized with the type and length of the pipes in Fig. 5.12b.

The reduction rate was decreased for longer silicone pipes due to larger bending, as explained above. On the other hand, the velocity reduction inside the wake was lower for the 20 cm long urethane and ABS pipes than their 10cm counterparts. Although the wave height reduction rate for the 20 cm long pipes were higher than the 10cm long pipes, the decreased wave height did not reduce the hydrodynamic force on the sphere tank because of its spherical shape. Thus, the force reduction for these pipes also decreased compared to the 10 cm long pipes of the same material.

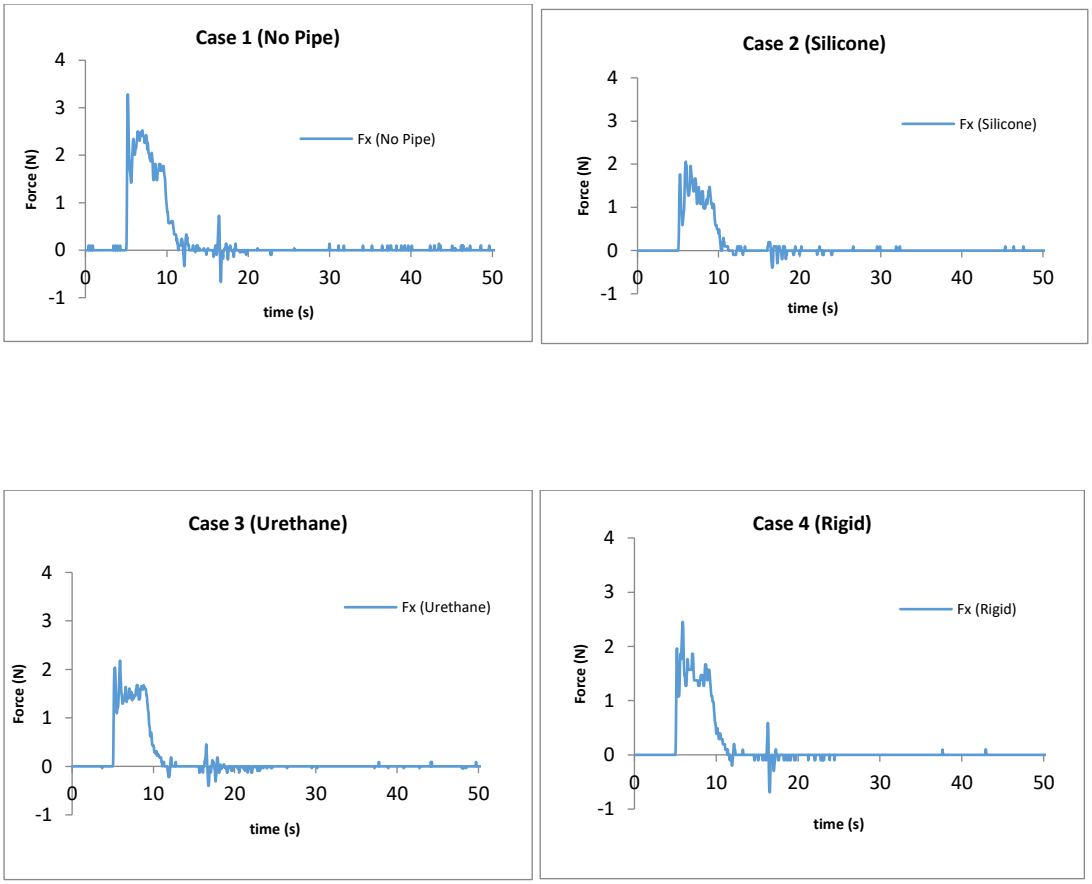

Fig. 5.8 Comparison of hydrodynamic forces for sphere tanks for the cases of 33 pipes, each of 10cm in length

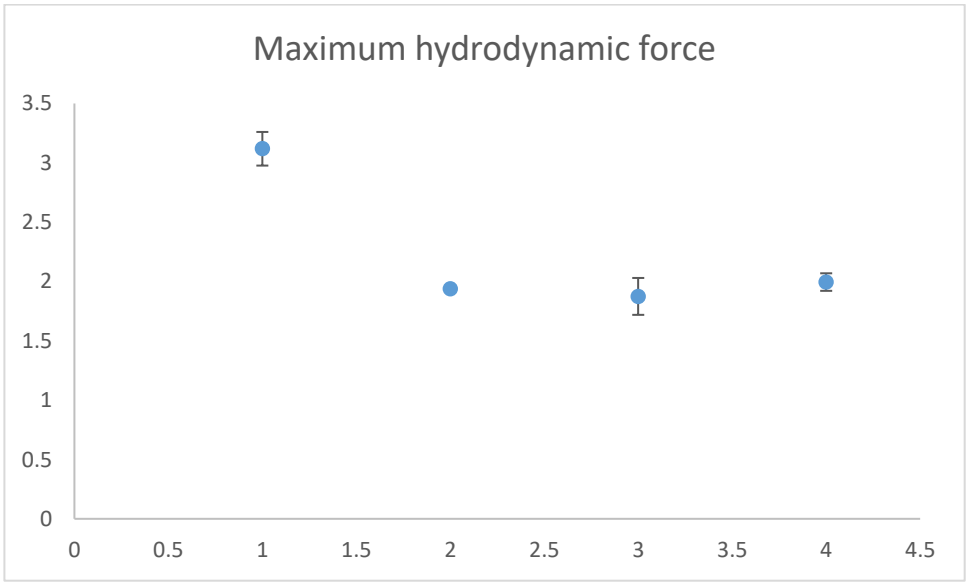

Fig. 5.9 Mean and standard deviation values of maximum hydrodynamic force measurements for Case 1, 2, 3 and 4

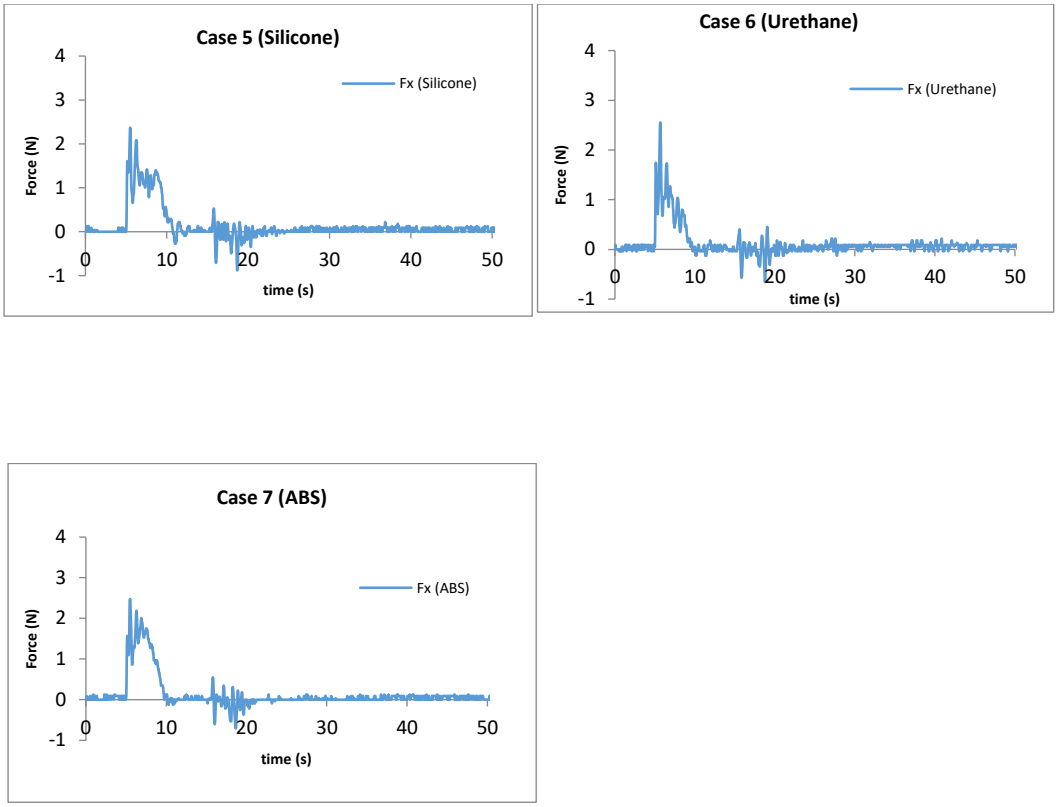

Fig. 5.10 Comparison of hydrodynamic forces for sphere tanks for 53 pipes, each 20cm long for Cases 5, 6, and 7

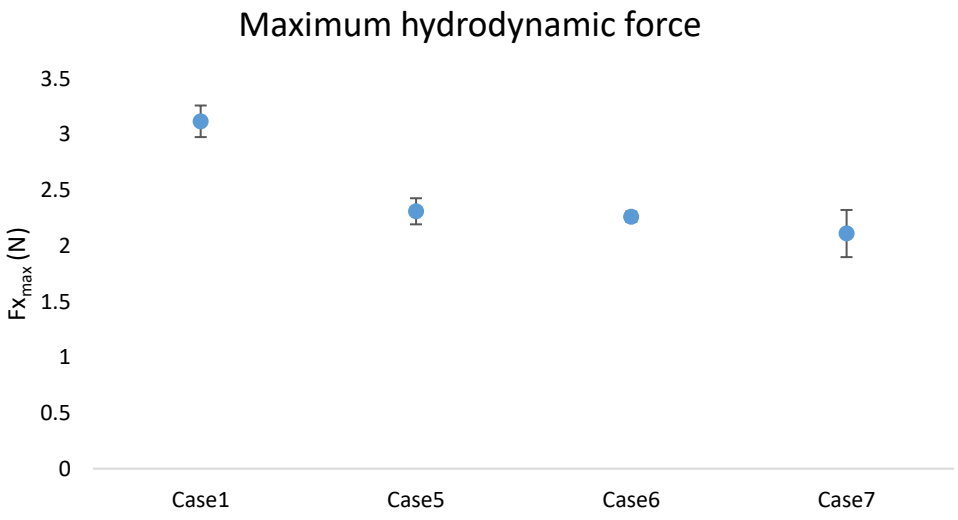

Fig. 5.11 Mean and standard deviation values of maximum hydrodynamic force measurements for Case 1, 5, 6 and 7

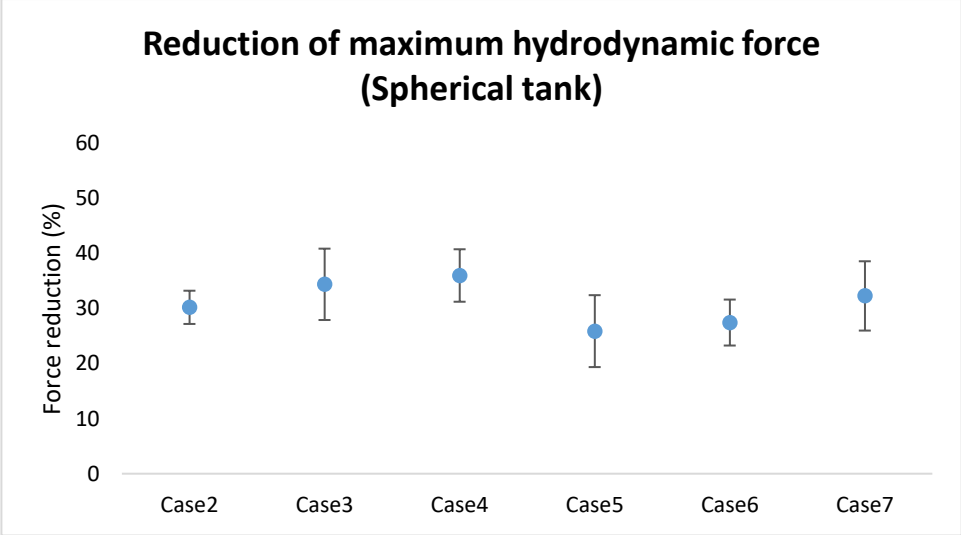

(a)

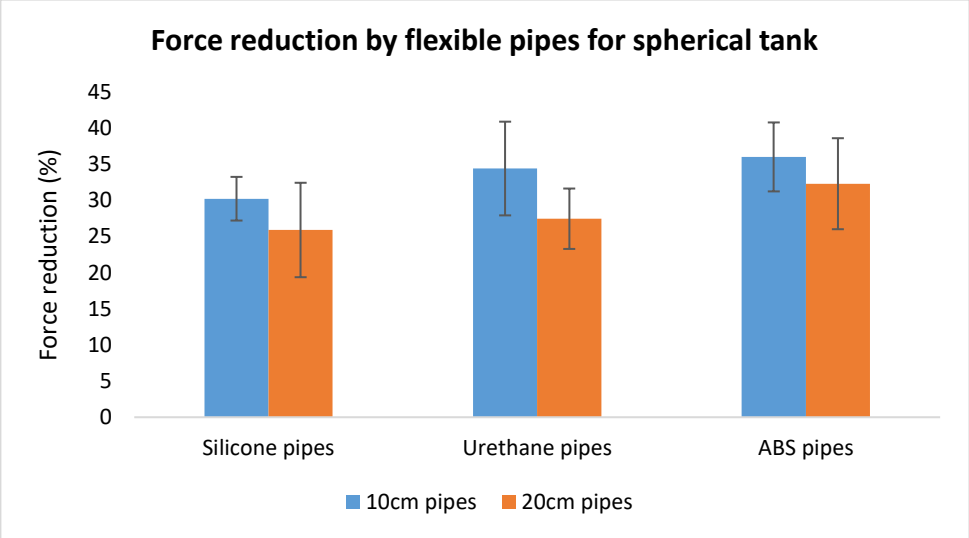

(b)

Fig. 5.12 Comparison of reduction of the maximum hydrodynamic load for 10cm long pipes and 20cm long pipes (a) categorized with case numbers (b) categorized with types of pipes

Hydrodynamic force measurements for the cylindrical tank with 20 cm long pipes are shown in Fig. 5.13. The silicone pipes could reduce, not only the impact load by the head wave, but also the remaining part of the hydrodynamic forces, as can be seen in cases 8 and 9. In this scenario, urethane pipes and rigid pipes could reduce the wave load better than the cases for

the spherical tank using the same pipes. The reason is that the wave height was reduced significantly by these two types of pipes. Therefore, the wetted surface area of the cylindrical tank decreased greatly and thus, hydrodynamic force was also greatly reduced. For the spherical tank, the wetted surface area was not significantly reduced by the reduced water height due to its spherical shape. Therefore, more effective force reduction was observed in the cylindrical tank than the spherical tank. The means and standard deviations of 6 runs for each case are shown in Fig. 5.14 to ensure the reproducibility of the experimental results.

In Fig. 5.15, the comparison of hydrodynamic force reduction between three types of pipes is shown. The same categorization is done similar to Fig. 5.12a and 5.12b. Moreover, the force reduction is also calculated using the formula shown in Eq. 5.1. The effectiveness of the flexible silicone pipes was significantly less than the more rigid urethane and ABS pipes due to a very large bending occurred due to increased length, as compared in Figs. 5.7a and 5.7c for 10cm and 20cm long flexible pipes, respectively.

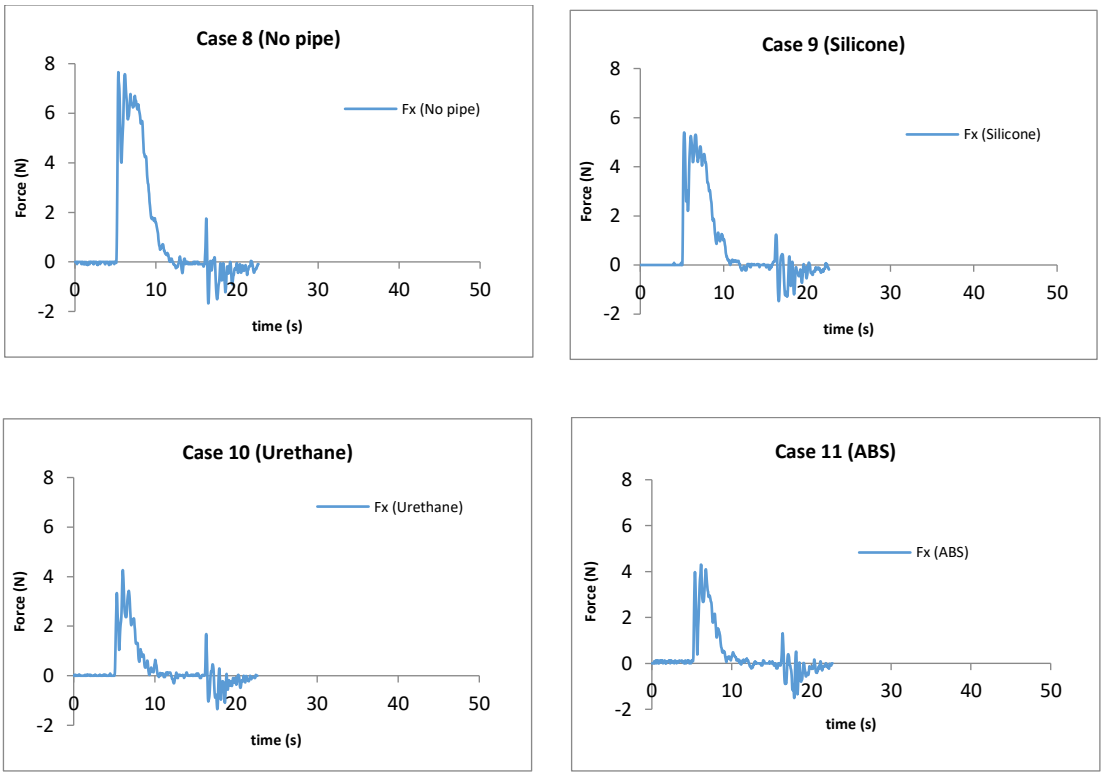

Fig. 5.13 Comparison of hydrodynamic forces for cylinder tank using 20cm long pipes

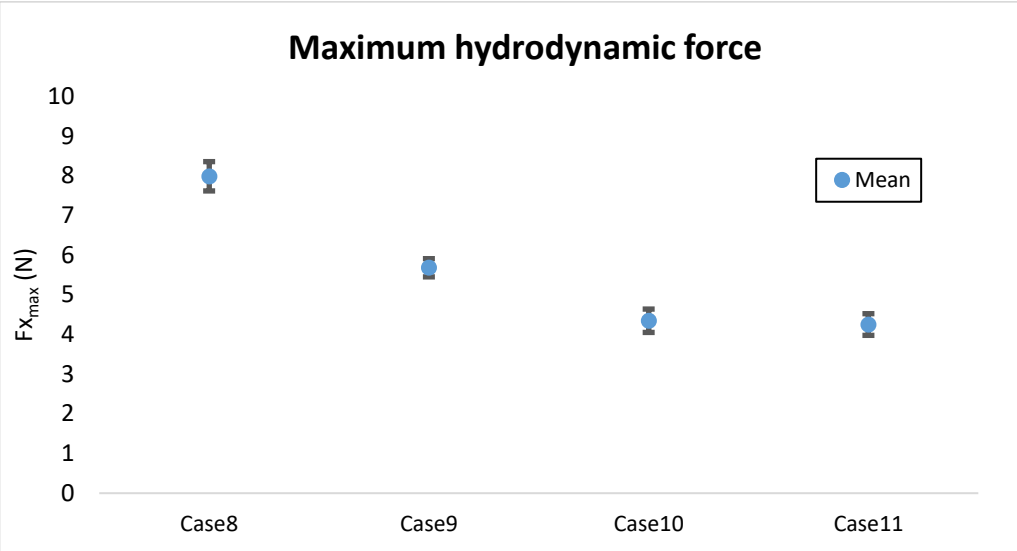

Fig. 5.14 Mean and standard deviation values of maximum hydrodynamic force measurements for Case 8, 9, 10 and 11

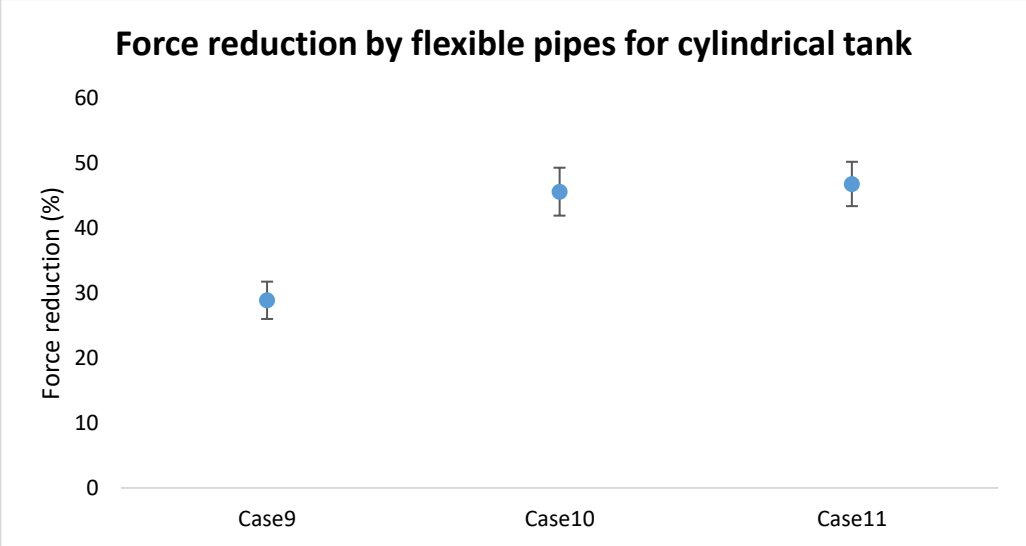

Fig. 5.15 Comparison of reduction of the maximum hydrodynamic force on cylindrical tank categorized with types of pipes

5.3 Simulations of tsunami basin experiments by finite volume framework with Volume of Fluid (VoF) method

Computational fluid dynamics (CFD) was used to simulate wave run-up and unsteady flow around flexible pipes and the oil-tanks. Finite volume method was employed in these simulations. The purpose of these simulations is to investigate the unsteady wave-run up, wave breaking and flow around the flexible pipes with the understanding of more detailed flow phenomena. The simulation conditions were defined to be similar to tsunami wave basin experiments, with the assumption of rigid pipes. In this section, considerations on the flow model, turbulence modelling, computational domain and numerical simulations will be explained.

5.3.1 Numerical model

Open-source CFD toolbox OpenFOAM was employed to solve the following 3D RANS equations. "interFoam" flow solver is an incompressible two-phase flow solver. It uses Volume of Fluid (VoF) method for free-surface capturing. Thus, interFoam solver was chosen in this study. The mass and momentum equations are as follows:

$$\frac{\partial \bar{u}_i}{\partial x_i} = 0 \tag{5.2}$$

$$\frac{\partial \rho \bar{u}_i}{\partial t} + \bar{u}_j \frac{\partial \rho \bar{u}_i}{\partial x_j} = -\frac{\partial p}{\partial x_i} + \frac{\partial}{\partial x_j}\left(\mu_{eff} \frac{\partial \bar{u}_i}{\partial x_j}\right) - g_i x_j \frac{\partial \rho}{\partial x_j} \tag{5.3}$$

where $\bar{u}_i$ (i = 1,2,3) is the flow velocity in x_1, x_2 and x_3 directions of the Cartesian coordinate system, p is the pressure. μ_{eff} represents the effective dynamic viscosity for each phase. μ_{eff} can be expressed as the summation of molecular dynamic viscosity and the turbulent kinetic viscosity as $\mu_{eff} = \mu + \mu_t$, where μ is the dynamic viscosity of the fluid and μ_t is the turbulent dynamic eddy viscosity obtained from turbulence modelling.

ρ is the density at any point in the computational domain calculated as:

$$\rho = \alpha\rho_{water} + (1-\alpha)\rho_{air} \quad (5.4)$$

α is the single phase function of each finite volume cell in which $\alpha = 0$ represents air, and $\alpha = 1$ represents water in that cell. From Eq. 5.4, the density of cells having $\alpha = 1$ equals to ρ_{water} while the fluid density of cells having $\alpha = 0$ equals ρ_{air}. Free-surface is represented by cells with $\alpha = 0.5$. The gravity forces are represented by g_i (i = 1, 2, 3) and $g_1 = g_3 = 0$ and $g_2 = -9.81$, i.e., the gravity is assumed to be in the $-x_2$ direction.

In order to compute the motion of air and water phases, the governing for the phase function α need to be solved. Phase movement is obtained by solving the following equation:

$$\frac{\partial\alpha}{\partial t} + \frac{\partial \bar{u}_i \alpha}{\partial x_i} - \frac{\partial \bar{u}_{c,i}\alpha(1-\alpha)}{\partial x_i} = 0 \quad (5.5)$$

where $\bar{u}_{c,i}$ is the artificial compression term to compress the interface. This term is introduced in OpenFOAM and active only in the interface region due to the term $\alpha(1-\alpha)$.

In this research, the SST $k-\omega$ turbulence model, developed by Menter (1994), is employed for turbulence modelling due to its ability to model flows involving adverse pressure gradients and severe separation like flow around rigid circular cylinders. Menter's SST $k-\omega$ model is a two equation turbulence model based on standard k-ω model with the shear stress transport (SST) formulation. Turbulent kinetic energy (k) and specific dissipation rate (ω) are computed by solving the following two equations.

$$\frac{\partial(\rho k)}{\partial t} + \bar{u}_j \frac{\partial(\rho \bar{u}_j k)}{\partial x_j} = P_k - \beta^* \rho k\omega + \frac{\partial}{\partial x_j}\left[(\mu + \sigma_k \mu_t)\frac{\partial k}{\partial x_j}\right] \quad (5.6)$$

$$\frac{\partial(\rho\omega)}{\partial t} + \frac{\partial(\rho \bar{u}_j \omega)}{\partial x_j} = \frac{\gamma}{\nu_t} P - \beta\rho\omega^2 + \frac{\partial}{\partial x_j}\left[(\mu + \sigma_\omega \mu_t)\frac{\partial\omega}{\partial x_j}\right] + 2(1-F_1)\sigma_{\omega 2}\frac{\rho}{\omega}\frac{\partial k}{\partial x_i}\frac{\partial\omega}{\partial x_i} \quad (5.7)$$

Where, $P = \tau_{ij}\frac{\partial u_i}{\partial x_j}$ and τ_{ij} is the stress tensor written as: $\tau_{ij} = \mu_t\left(\frac{\partial u_i}{\partial x_j} + \frac{\partial u_j}{\partial x_i} - \frac{2}{3}\frac{\partial u_k}{\partial x_k}\delta_{ij}\right) - \frac{2}{3}\rho k\delta_{ij}$.

Additional functions are given by:

$$F_1 = \tanh(arg_1^4),\ arg_1 = min\left[max\left(\frac{\sqrt{k}}{\beta*\omega d}, \frac{500\nu}{d^2\omega}\right), \frac{4\rho\sigma_{\omega 2}k}{CD_{k\omega}d^2}\right]$$

$$CD_{k\omega} = max\left(2\rho\sigma_{\omega 2}\frac{1}{\omega}\frac{\partial k}{\partial x_j}\frac{\partial \omega}{\partial x_j}, 10^{-20}\right)$$

$$F_2 = \tanh(arg_2^2), arg_1 = max\left(2\frac{\sqrt{k}}{\beta*\omega d}, \frac{500\nu}{d^2\omega}\right)$$

$$\gamma_1 = \frac{\beta_1}{\beta^*} - \frac{\sigma_{\omega 1}\kappa^2}{\sqrt{\beta^*}}, \gamma_2 = \frac{\beta_2}{\beta^*} - \frac{\sigma_{\omega 2}\kappa^2}{\sqrt{\beta^*}}$$

The functions $F_1$and F_2 are blended by $\phi = F_1\phi_1 + (1 - F_1)\phi_2$. The closure coefficients are given as follows:

$\sigma_{k1} = 0.85$, $\sigma_{k2} = 1.0$, $\sigma_{\omega 1} = 0.5$, $\sigma_{\omega 2} = 0.856$, $\kappa = 0.41$, $\beta_1 = 0.075$, $\beta_2 = 0.0828$, $a_1 = 0.31$.

The turbulent eddy viscosity μ_t can be obtained from

$$\mu_t = \frac{pa_1k}{\max(a_1\omega, \Omega F_2)} \tag{5.8}$$

Where $\Omega = \sqrt{2\mathrm{W_{ij}W_{ij}}}$ is the vorticity magnitude, with$\mathrm{W_{ij}} = \frac{1}{2}\left(\frac{\partial u_i}{\partial x_j} - \frac{\partial u_j}{\partial x_i}\right)$, recommended by Menter (1994).

5.3.2 Computational domain

The experimental tank consists of 2 slopes for the tsunami run up: a 1/40 and 1/100. However, only the 1/40 slope is used in the simulation because the pipes and model tank in the experiment are placed on the 1/40 slope. Moreover, the depth of the domain was decreased to 0.7m, although the experimental tank depth is 0.9m because the highest water elevation was up to 0.65 m in the experiment, located at the dam-side water-column. Therefore, in order to reduce significant computational cost, the dimensions for the simulation domain were considered as (21.25m x 0.7m x 0.7m). The slope and the step of the tsunami tank were also included in the simulation domain. Fig. 5.16 shows the whole domain displaying the step and slope of the tsunami wave basin being accounted for in the computational domain. The red region represents water while the blue region is the air. The left side of the domain is the reservoir which was initially filled with water to get a water column of 0.25 m. The pipes and the tank were also placed at the same locations in the simulation domain as the experiment as shown in Fig. 5.16. The volume of the water being filled was measured during the experiment based on the capacity of the pump used for filling water into the reservoir and the time taken to fill. This measured volume was used to create the water column on the dam site in the CFD simulations.

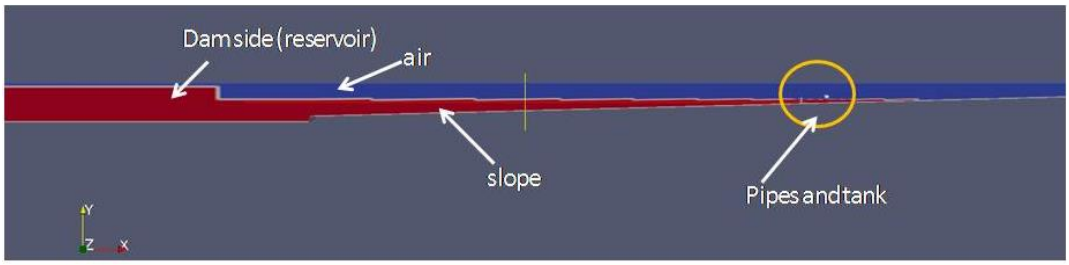

Fig. 5.16 Overview of the computational domain showing the water column in the reservoir and the (1/40) slope

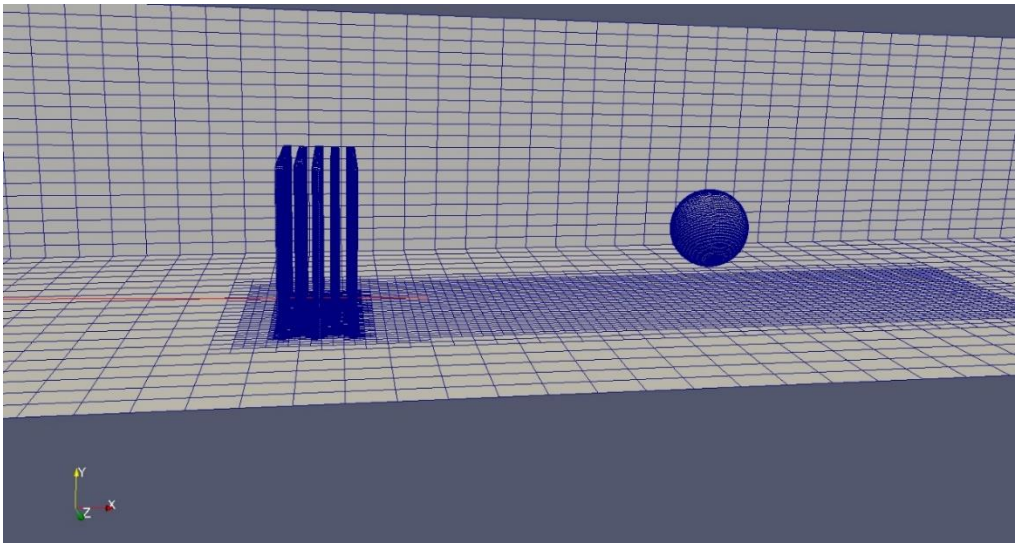

Fig. 5.17 Mesh showing rigid pipes and the sphere

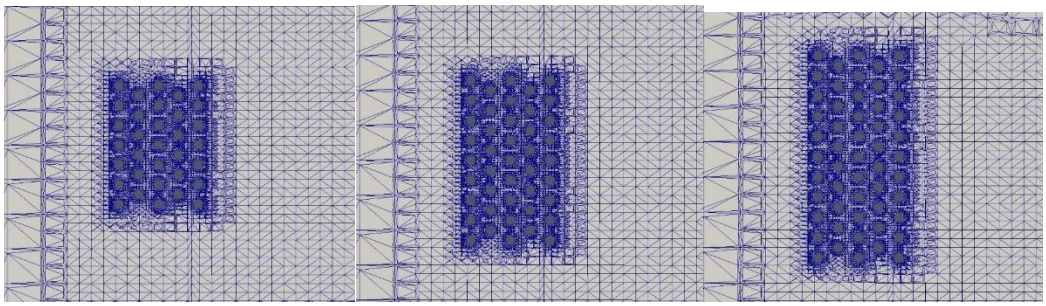

(a) (b) (c)

Fig. 5.18 Computational mesh for (a) 33 pipes, (b) 43 pipes, and (c) 53 pipes cases

The pipes were assumed to be rigid pipes instead of flexible pipes at this stage of work due to unreasonably high computational cost to compute the structural deformations of multiple pipes. While reliable the estimate of flow reduction by flexible pipes in full-scale cannot be obtained by using this numerical model, the phenomena on the flow around flexible pipes can be evaluated by this rigid pipe assumption. Moreover, from the experiments, it was observed that the deformation of flexible pipes far from the tsunami wave head (i.e., pipes in 4^{th} or 5^{th} rows) in the inflow direction were relatively small compared to those nearer to the wave head due to gradually reduced flow velocities (Fig. 5.7a). Therefore, for the case with multiple rows of

flexible pipes, this rigid pipe assumption is enough and it can give insight into tsunami reduction depending on the orientation of pipes.

Meshes were generated for the no-pipe, 33 pipes, 43 pipes and 53 pipes cases with the spherical tank and cylindrical tank, respectively. The mesh for the case of 53 pipes with the spherical tank showing the orientation of the pipes and the sphere in 3D view is displayed in Fig. 5.17. The closed view of the mesh for rigid pipes in the cross section is shown in Fig. 5.18 for 33 pipes, 43 pipes and 53 pipes. The region between the pipes and the oil tank was refined in order to catch the detailed flow features as well as the free surface deformation during the impact on the pipes and the tank by the wave. The base wooden board is neglected in the numerical model.

Non-slip wall boundary conditions were chosen for two ends of the numerical tank and the floor. The rigid pipes and oil tank were also considered as non-slip walls. The side walls of the tsunami tank were assigned as non-slip walls while the boundary condition for the tank top was defined as open to the air with atmospheric pressure being defined on it. Wall-functions were employed for the SST k-ω turbulence model for all non-slip walls.

5.3.3 Numerical schemes

Second order finite volume schemes were chosen for spatial discretization in order to keep a sharp free surface, while the Euler implicit scheme was applied to temporal discretization. The interFoam solver utilizes the VOF method for free-surface capturing for the two-phase flow involving water and air. The fluid properties for the simulation are as shown in Table 5.2. Pressure-Implicit-Splitting-of-Operators (PISO) algorithm was employed for velocity-pressure coupling. Very high air velocities occurred during the impact of the tsunami wave on the structures, leading to the need for very small time steps during the impact. If a constant time step was assigned, the simulation might be unstable during tsunami impact. Thus, the simulation time step was controlled by the CFL condition (Courant number <1) instead of a constant time step. In this work, the overall Courant number for the whole domain was kept below 0.9 while the Courant number for the interface region was kept less than 0.5.

Table 5.2 Fluid properties for the CFD simulation

Fluid Properties		
Phase	Kinematic viscosity (m^2/s)	Density (kg/m^3)
Water	1.00E-06	998.2
Air	1.59E-05	1.205

5.4 Validation of the numerical model

Flow velocities in the CFD simulations were compared to the experimental results recorded by electromagnetic velocity transducers at the same locations of the experimental basin. Hydrodynamic forces acting on oil tanks by the tsunami flow are calculated by integrating the pressure throughout the tank surface.

5.4.1 Comparison of hydrodynamic force between CFD and experiments

Fig. 5.19 shows the comparison of hydrodynamic force acting on the spherical tank between the experiment and CFD. For the no-pipes case, CFD over-predicted the wave force when the wave impact on the sphere occurs, but the difference is smaller after the impact. The over prediction by CFD was contributed to the rough tank walls and the presence of the base wooden board. The floor of the experimental tank is made of wooden board which showed certain roughness. Moreover, the side walls of the tank which were made of steel became rough due to some corrosion. In CFD simulations, these roughness effects were neglected, with the floor and side walls being assumed to be smooth non-slip walls. The motion of the door was also ignored. Thus, the calculated force results are larger than the measurements from the experiments.

In the experiments, when the watertight door was opened, the door moved in a rotary motion towards the calm water surface. This motion of door acted as a wave-maker with a short stroke, generating small waves after the main tsunami wave head. Thus, the generated wave consisted of several much smaller waves. On the other hand, the natural frequency of the measurement system has no significant effect on the force measurements as explained in Section 4.1.3. Thus, several fluctuations were observed in the time history of force measurements due to several small oscillations in the generated wave. In CFD simulation, this effect of the motion of watertight door and the natural frequency of force measurement system were not considered.

Therefore, CFD results of force calculations showed much less vibrations as in Fig. 5.19 (a). In the cases with the pipes, unsteady wave run-up through showed very complex flows, especially for 53 pipes case shown in Fig. 5.19 (c). This flow involves vortex shedding from each pipe as well as from the whole arrangement. Thus, the force acting on the tank showed several vibrations. CFD could predict this result with enough accuracy as compared in Fig. 5.19c. Moreover, force data computed using CFD showed very similar trends as the measured values. To sum up, force calculation results from CFD showed good agreements with experiments.

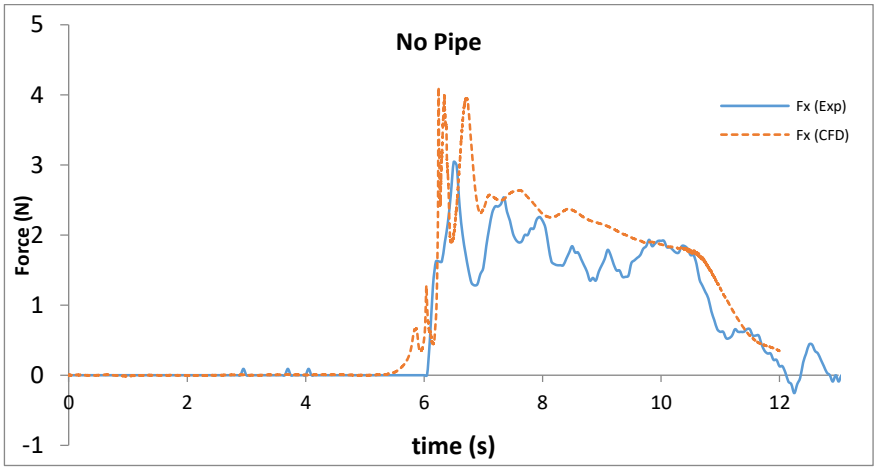

(a)

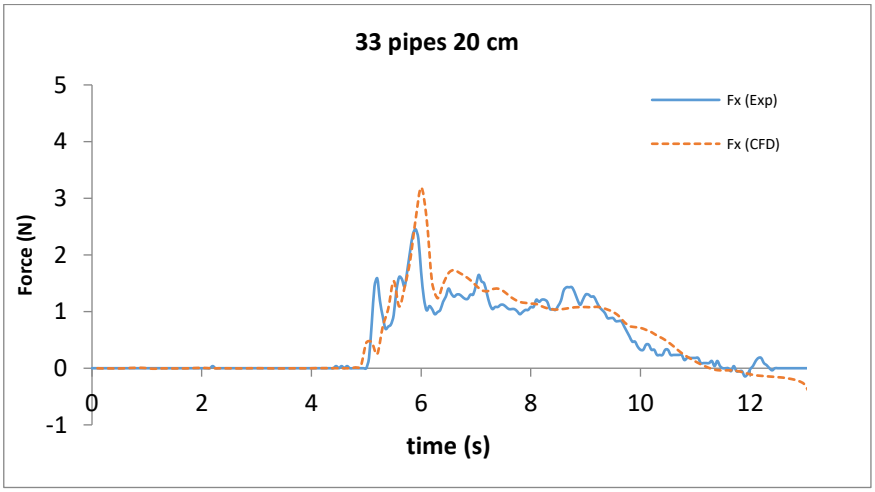

(b)

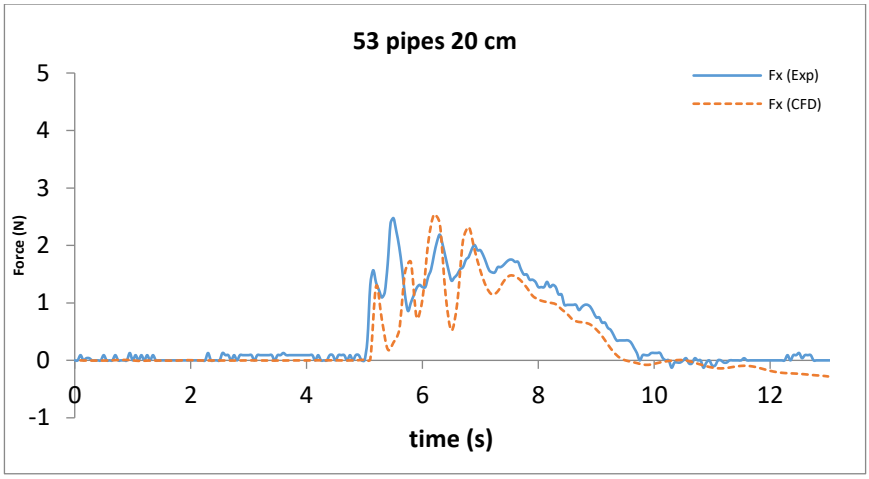

(c)

Fig. 5.19 Comparison of hydrodynamic force between experiments and CFD for (a) no pipes (b) 33 pipes and 53 pipes cases

5.4.2 Comparison of flow velocity

In Fig. 5.20, the velocity computed by CFD is compared with the measurements for no pipes, 33 pipes and 53 pipes arrangements. CFD could predict the flow velocity at the front probes for all cases with moderate accuracy, with the velocity amplitudes being predicted accurately for no pipes and 33 pipes setups. However, there is some difference between numerical results and experiments for the velocity behind the pipes. This is contributed to the roughness of the wooden board and very complex flow features inside the wake behind the pipes. A very fine mesh is necessary to capture the wake behavior and the free-surface, which would lead to very high computational costs.

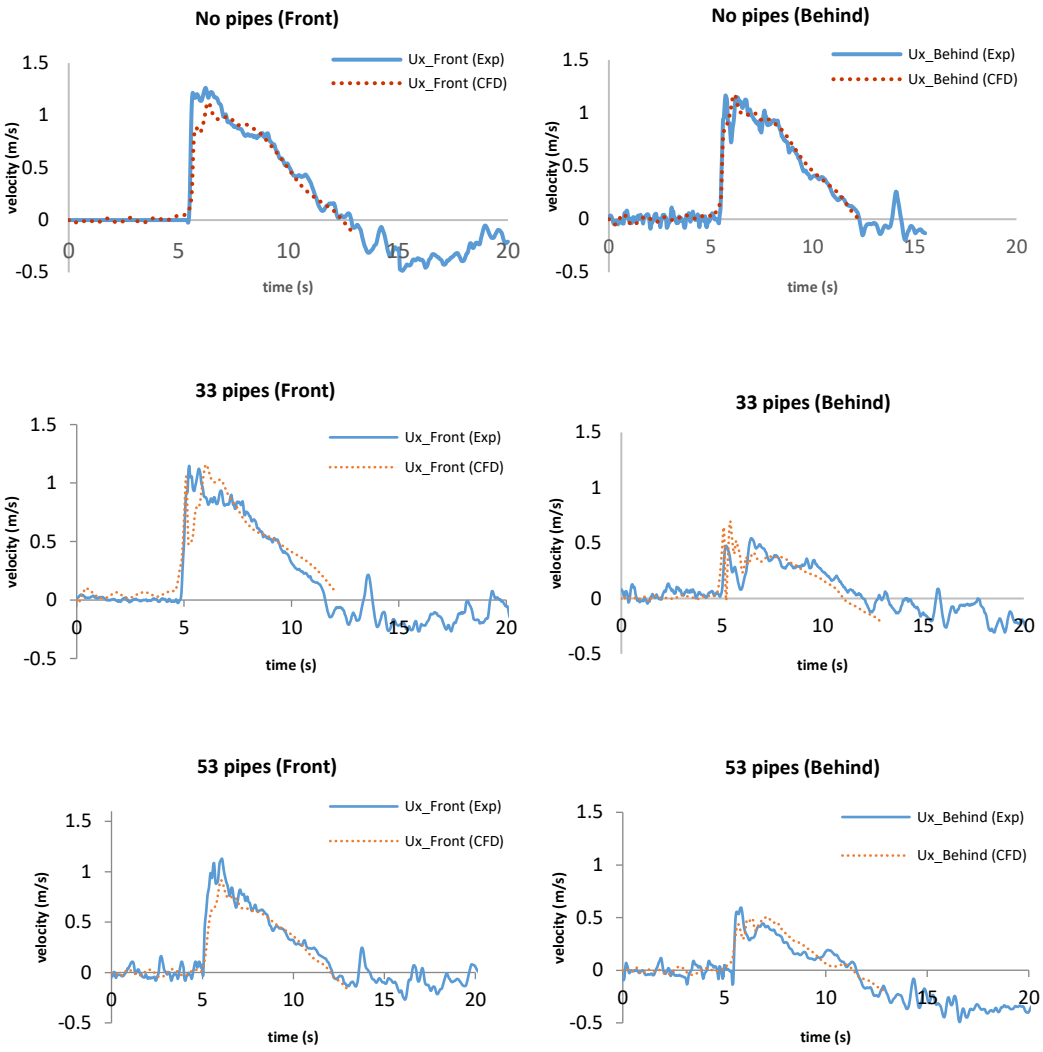

Fig. 5.20 Comparison of the velocity between experiments and CFD (no pipes, 33 pipes and 53 pipes cases)

5.4.3 Wave-profile and wave-breaking

As mentioned previously, a finite volume framework with VoF method was chosen for its ability to simulate wave-breaking phenomenon. To validate the simulation results, qualitative analysis was also carried out by comparing the flow nature between CFD and experiments. Such a comparison is shown in Fig. 5.21. The left figures are CFD output of the tsunami wave and the right figures are photos taken by high-speed camera during the experiment. It was found that CFD could predict the wave run-up well. But after wave-breaking occurred, CFD results became less accurate because the mesh was not fine enough to capture the spray. However, these effects are not very important for this study since the detail study on wave breaking is out of the scope of this study. Overall, the wave shapes computed by CFD showed good agreements with the experiments before and after the wave-breaking.

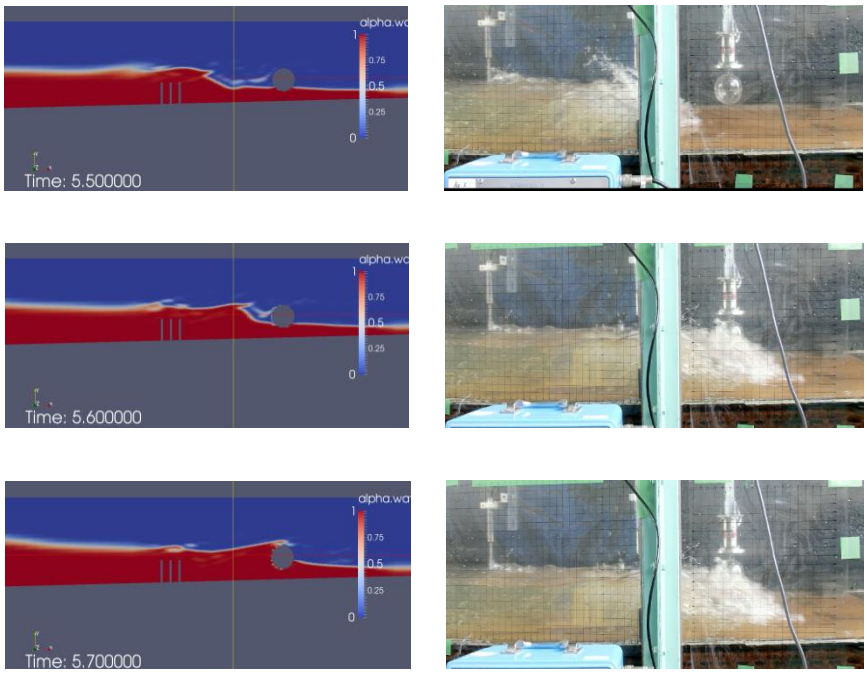

Fig. 5.21 Comparison of wave profile between CFD and experiment at different time steps at t=5.5s, t=5.6s and t=5.7s

5.4.4 Analysis on the influence of the width of arrangement on force reduction

In this section, the effect of width of pipe arrangement on reduction of hydrodynamic load on tank is estimated based on CFD simulations. Fig. 5.22 shows the effectiveness of increased number of pipes in the cross-flow direction using 7, 9 and 11 pipes in cross-flow direction, totaling 33, 43 and 53 pipes, respectively, with the same column number in inflow direction, as previously shown in Fig. 5.18. The force reduction was computed using equation 5.1 from Section 5.2.2 using the maximum hydrodynamic forces obtained from CFD.

The numerical results in Fig. 5.22 suggest that the effectiveness of width in the cross-flow direction with the form of exponential recovery, reaching a constant value. It can be deduced that the reduction will converge at a certain value where the whole area behind the flexible pipes becomes a dead zone, where reverse flow or retarded flow is formed due to the presence of the pipes. Thus, it is suggested that the rows of pipes in the inflow direction should be increased rather than to increase the width of the arrangement to obtain better tsunami damage reduction.

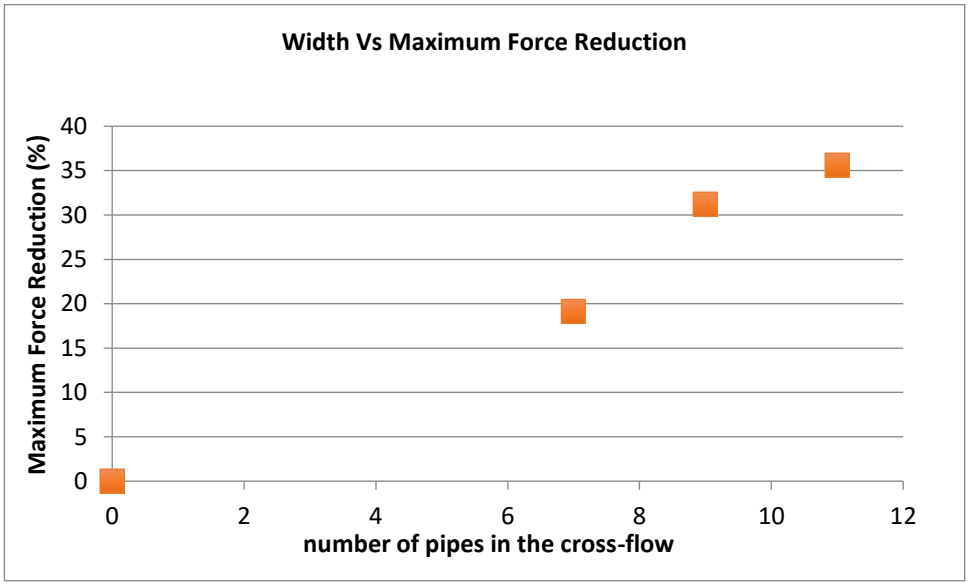

Fig. 5.22 Prediction of the effect of number of pipes in cross-flow direction by CFD

5.5 Conclusions

The effectiveness of flexible-pipe-system in tsunami reduction was assessed for different materials of pipes having different bending stiffness values by comparing the reduction of hydrodynamic load on oil tanks caused by tsunami attack by means of scale-model experiments. Numerical analysis using CFD was carried out to understand the detail flow features around the pipes as well as at the wave head. The tsunami basin experiments suggested that the application of flexible pipes could reduce the hydrodynamic force acting on the oil tanks by the tsunami flow, as well as flow velocity. The maximum tsunami load could be reduced up to approximately 35 percent by using flexible silicone pipes and up to 44 percent by using more rigid pipes such as those made of urethane rubber and ABS. However, the rigid pipes are likely to disturb the marine traffic around the area of installation whereas the flexible pipes would not. According to these results, the use of flexible pipes could be considered as an effective tsunami damage reduction mechanism for oil and gas refineries, located in the areas vulnerable to tsunami attacks. Moreover, such flexible pipes can be used in combination with other countermeasures such as earth-banks to further reduce the tsunami damage on the oil tanks.

A numerical model was created to replicate the tsunami attack on an oil tank with the assumption of rigid pipes. The numerical model was validated by comparing with the experimental data. Numerical results showed good agreement with experiments for flow velocity and hydrodynamic forces. The peak values of hydrodynamic forces computed by CFD agreed with the measurements, and CFD could predict the flow phenomena well. This model can give insight into the flow phenomena around flexible pipes.

As the width of the flexible arrangement in the cross-flow direction increases, the force reduction will increase with the form of exponential recovery, reaching a constant value. Therefore, the number of rows of pipes should be increased in the inflow direction for better

reduction of tsunami force. Such a model can be extended for multiple oil and gas tanks and used to predict the tsunami damage reduction for a large coastal area, such as the Osaka Bay. Further researches including structural analysis of the pipes and detail mechanisms of pipes arrangement as well as study on the reduction of full-scale tsunami force are still necessary to fully understand the feasibility and cost-effectiveness of the use of flexible pipes for tsunami flow reduction.

Chapter 6

Analysis on the effectiveness of flexible pipes under a quasi-2D tsunami flow by experimental approach

This chapter deals with the estimation of tsunami load reduction with the assumption of a quasi-2D flow, eliminating the effects of flow around the pipes arrangement. Thus, a flexible-pipe-system that covers the whole width of the tsunami wave tank was employed. The reduction in momentum flux carried by the tsunami is investigated in the first part of this chapter (Experiments 1). In the second part (Experiments 2), the effect of the distance between the flexible pipes and oil tank is evaluated. In the last part (Experiments 3), the tsunami wave force acting on an oil tank located on an earth bank of a coastal area is studied, with the consideration of a dyke wall near the oil storage facility.

6.1 Experiments 1: Analysis on the reduction of unsteady momentum flux

In these experiments, the reduction of momentum flux carried in the tsunami flow by the flexible pipes is measured. Therefore, the experimental condition with no oil tank was considered in order to eliminate the effects of interaction of oil tank and flexible pipes.

6.1.1 Experiments 1: Experimental setup

The detailed arrangement of sensors and flexible pipes is shown in Fig. 6.1a. This figure was drawn with the scales different from the actual experimental conditions. Three wave gauges

and two electromagnetic flow velocity sensors were employed. The positions in this figure are measured from the water gate (refer to Fig 4.1 in Section 4.1.1 where location of x=0 is illustrated). The wave gauge WG01 was attached at x = 6 m in order to measure the incident wave elevation as a reference value. Water elevation in front of and behind the flexible pipes were measured by WG02 and WG03, respectively. Flow velocity in front of and behind the flexible pipes were measured using electromagnetic velocity meters VS1 and VS2, respectively. All the sensors were synchronized on a same time history using the highest value of WG01 as a reference value. Flexible pipes were placed at x = 16.8 m which is the end of 1/40 slope. As explained in Section 4.1.1, the wave generated by combined flapper-dam-break system consisted of the head wave followed by multiple smaller waves. As the wave train ran up the 1/40 slope, the height of the head wave increased gradually. Finally, wave breaking of the head wave occurred at around x = 10 m and the flow ran up towards the flexible pipes as a turbulent bore.

The location for the pipes were chosen to be at the end of 1/40 slope because at this point, wave breaking already occurred and the flow was a turbulent bore as explained above. Moreover, the water depth at this point is 5 cm which corresponds to 5 m water depth. For actual implementation, the slope of the coastal area might vary with the location along the coast. However, the water depth of 5 to 9 m is envisioned to place the flexible pipes. Thus, the end of 1/40 slope was chosen in these experiments. Flexible silicone rubber pipes explained in Section 4.2.1 were employed in these experiments.

The top view of flexible-pipe arrangement is shown in Fig. 6.1b. 31 and 30 pipes were used for each row and 7 rows were assumed in these experiments. From the experimental results of Okubayashi (2014) and numerical results of Tar (2015), the effectiveness of the pipes was very similar if the number of rows was 5 or above. Since the real-world condition was assumed in the current experiments, 7 rows of pipes were considered.

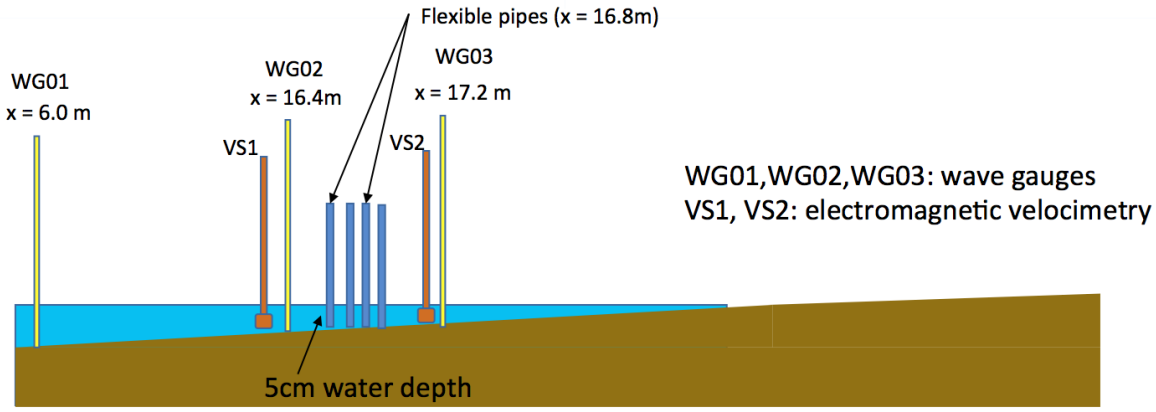

Fig. 6.1 (a) Schematics of experimental setup for Experiments 1

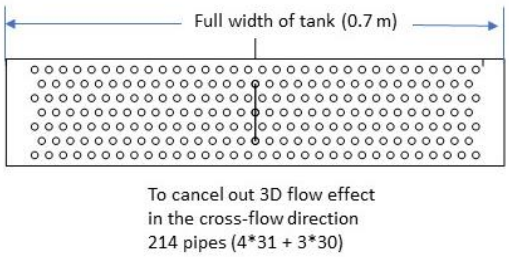

Fig. 6.1 (b) Arrangement of flexible pipes to cover the full width of the tsunami wave tank

6.1.2 Experiments 1: Results and discussions

There is a tendency that the incident waves might differ by a small amount due to the uncertainty of water level in the reservoir. Therefore, at least 5 times of runs were carried out for each scenario. Fig. 6.2a, 6.2c and 6.2d show the elevations of sample waves for the cases with and without the flexible pipes. Fig 6.2a shows the time series of incident wave elevations measured by WG01. The waves generated by using dam break method showed very similar features with a small variation of maximum wave amplitudes. According to Figure 6.2c, the wave elevation measured by front wave gauges (WG02) was higher when there were flexible pipes due to reflection of wave at the pipes due to increased pressure of the wave run-up. This agrees with the experimental results by Huang et al. (2011). On the other hand, measurements

behind the pipes (WG03) in Fig. 6.2d showed that the wave height was reduced by approximately 34 percent by the attachment of flexible pipes. The average reduction of elevation from all test runs is 33.85 percent. It is deduced that this reduction was mainly caused by wave energy dissipation inside the flexible pipes.

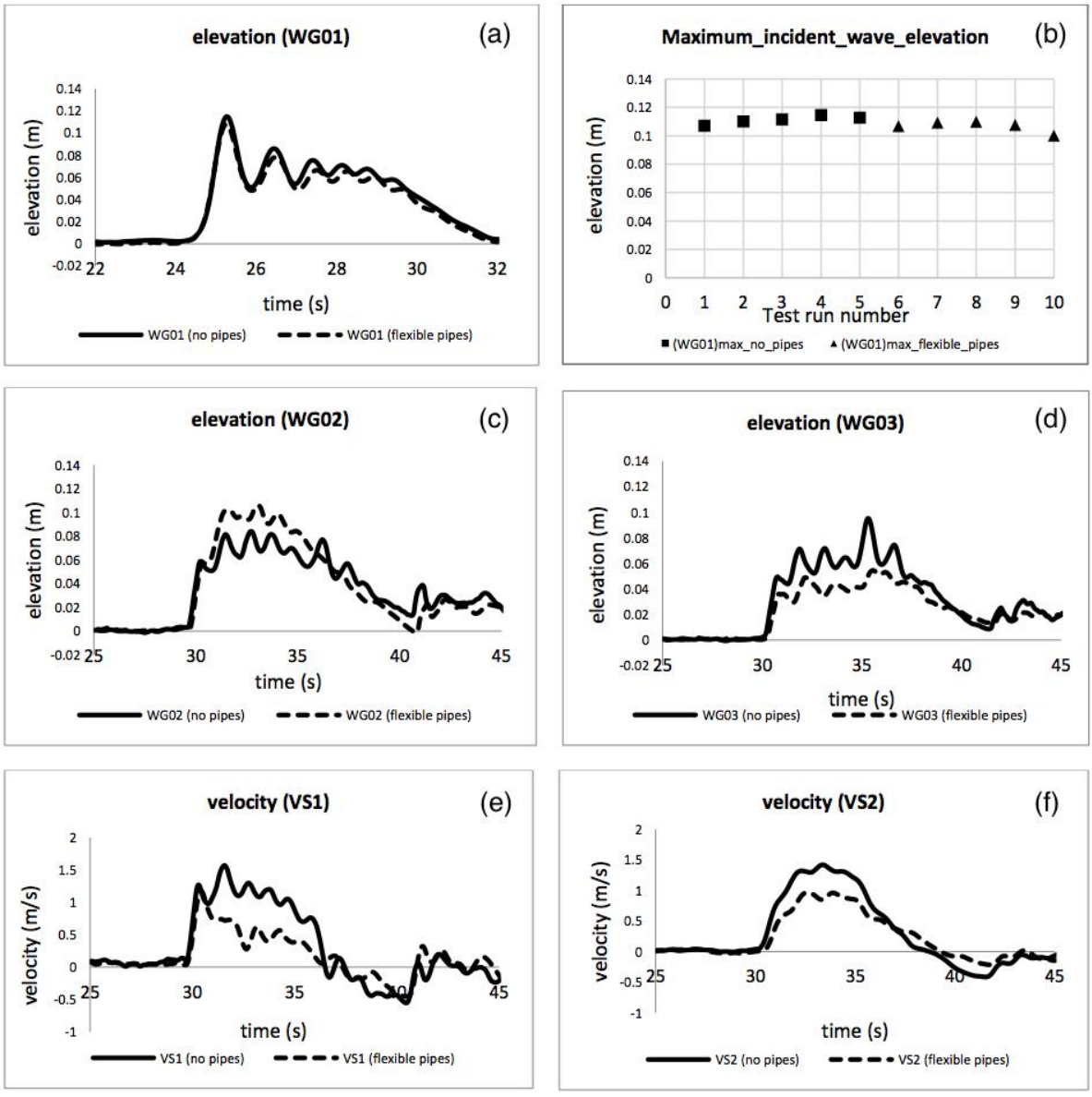

Fig. 6.2 Comparison of wave elevations measured at: (a) WG01 (b) maximum incident wave elevation measured at WG01 (c) WG02 (d) WG03 (e) Comparison of velocity measured at VS1 (f) Comparison of velocity measured at VS2

The time history of velocity measurements at VS1 and VS2 are shown in Fig. 6.2e and 6.2f. The velocity measured at VS1 for the case with flexible pipes was smaller than the case without pipes as in Fig. 6.2e. This is because wave reflection due to the blockage of the flow by the pipes. Fig. 6.2f showed the time series of the velocity measured behind the pipes. The flow due to incident wave was observed between time = 30 and 37 second. After that, the backwash of the tsunami along the slope occurred during the time between 37~45 seconds, with the negative velocities as in Fig. 6.2e and 6.2f. Velocity reduction of the tsunami flow by the flexible pipes were not very clear because the front velocity was also reduced by the blockage effect of the pipes. However, from Fig. 6.2d and 6.2f, it was observed that the use of flexible pipes could reduce both the elevation and velocity of a tsunami flow.

From the measurements of flow velocity and water elevation behind the pipes, unsteady momentum flux per breadth (M) was calculated using the following equation:

$$M = \rho_{water} h u^2 \tag{6.1}$$

where, h is the water height measured at WG03 (Fig 6.2c) and u is the unsteady flow velocity measured by VS2 (Figure 6.2f). It is assumed that the velocity distribution throughout the water depth is the approximately equal to the measured values by VS2. The unsteady momentum flux calculated is shown in Fig. 6.3a.

The results are compared in Fig. 6.3b. The results suggest that momentum flux carried by a tsunami-like long period wave could be reduced by more than 50 percent for sample case. Comparison of peak values of normalized momentum flux for all test runs is shown in Fig. 6.3c. It was clearly observed that more than 50 percent of maximum momentum flux could be decreased by scale-model flexible pipes. Then, the average values and standard deviations can be obtained using these equations:

$$M_{average} = \frac{\sum_{i=1}^{n} M_{\max}}{n}, n = 5 \tag{6.2}$$

$$\sigma = \sqrt{\frac{1}{n}\sum_{i=1}^{n}(M_{\mathrm{i}} - M_{average})^2}, n = 5 \quad (6.3)$$

where $M_{\max}$ is the maximum momentum flux per breadth obtained from Fig 6.3b, $M_{average}$ is the average value and σ is the standard deviation. n is the number of test runs which is 5 for each case. The results obtained are shown in Fig 6.3c. The reduction of maximum momentum flux can be estimated by using data from Fig. 6.3b as follows:

$$M_{reduction} = \frac{M_{average(no\ pipes)} - M_{average(flexible\ pipes)}}{M_{average(no\ pipes)}} \text{x } 100\% = 52.45\% \quad (6.4)$$

The results of Experiments 1 suggested that flexible pipes could decrease up to 52.45% of momentum flux carried by tsunami wave. This result can be extended to estimate the reduction of hydrodynamic forces acting on buildings, structures and oil tanks using Yeh (2007)'s formula. However, it is still necessary to measure the hydrodynamic forces acting on an oil tank in order to understand the effectiveness of flexible pipes in tsunami flow reduction.

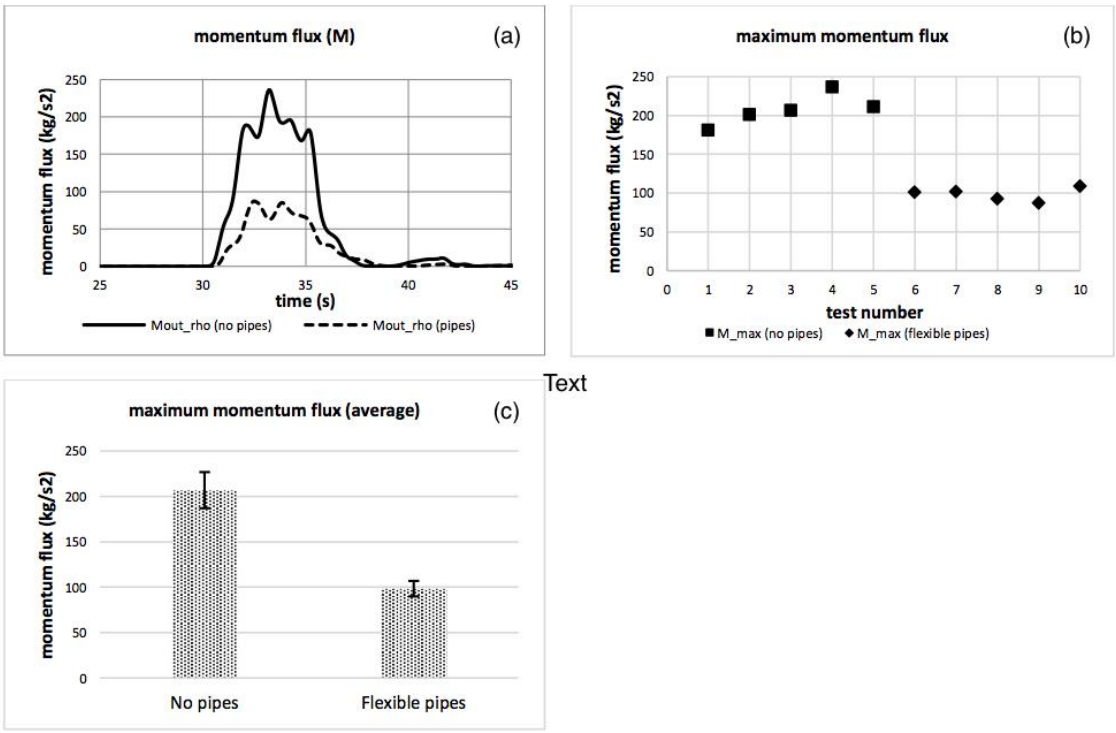

Fig. 6.3 Comparison of momentum fluxes (a) time history of momentum flux (b) maximum momentum fluxes for all test cases (c) average momentum fluxes and error

6.2 Experiments 2: Analysis on the reduction of hydrodynamic forces acting on a semi-submerged cylindrical tank

As mentioned in Section 6.2, it is necessary to assess the effectiveness of flexible pipes in the reduction of hydrodynamic forces on energy storage tanks located in industrial complexes. In Chapter 5, the measured results of hydrodynamic forces acting on a spherical tank and cylindrical tank with and without the presence of flexible pipes were presented. However, at that stage, the pipe arrangement did not cover the whole width of the tsunami basin, causing tsunami wave to flow around the pipes. In order to understand the force reduction phenomenon clearly, it is necessary to cancel out 3D flow phenomena in these experiments. So, in this chapter, the width of the flexible-pipe system was chosen such that can cover the width of the wave basin in Experiments 1 to create a 2D flow effect.

6.2.1 Experiments 2: Experimental setup

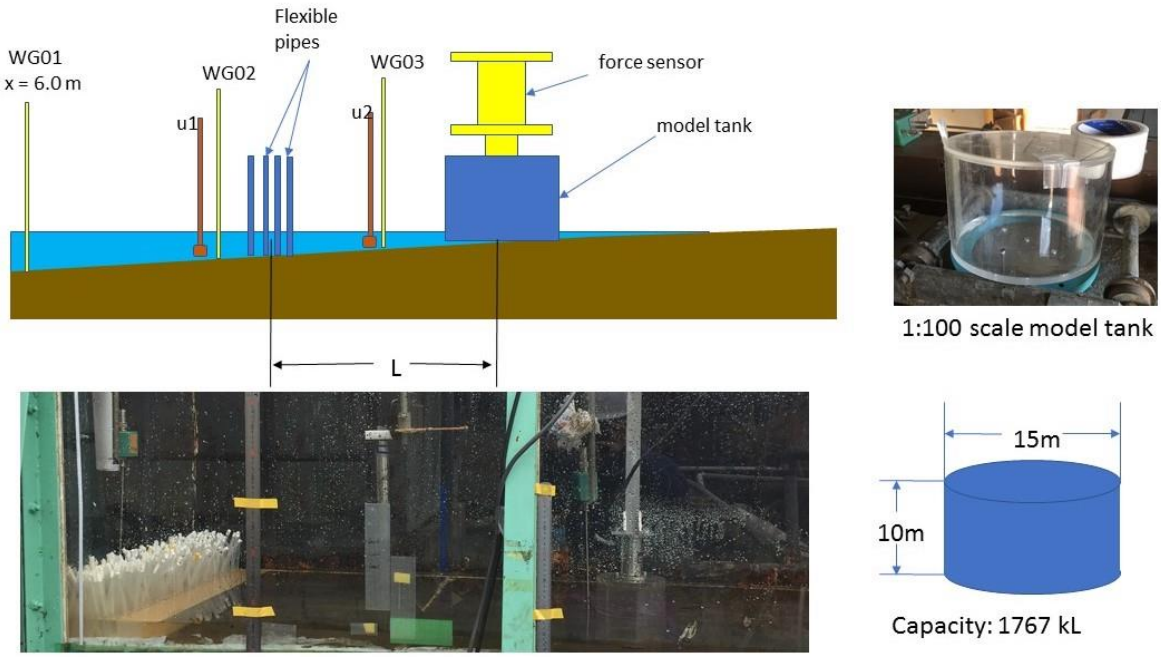

Fig 6.4 Experimental setup side view with (a) model tank (b) cylindrical oil tank in full-scale and model scale

Table 6.1. Different cases of Experiments 2 based on the distance between the pipes and oil tank

Case	L	Flexible pipe
Case 2_1	~	No
Case 2_2	0.35 m	Yes
Case 2_3	0.60 m	Yes
Case 2_4	0.85 m	Yes

Tsunami-like long period wave was generated by means of dam break phenomenon in the same conditions as Experiments 1 explained in Section 6.1. The location of the flexible pipes is the same as Experiments 1 which was illustrated in Fig. 6.1. The detail setup of Experiments 2 is shown in Fig. 6.4.

An acrylic 1:100 model tank of a 1760kL tank in full-scale was used in experiments. According to Zama et al. (2012), 110 tanks of less than 500kL capacity, 30 tanks of between 500kL and 1000kL capacity and 16 tanks of 1000kL to 10000kL capacity were drifted during 2011 tsunami. Thus, the oil tank presented here is relevant to predict the tsunami-induced hydrodynamic load on tank. Similar tsunami load on oil tanks measurements, such as those conducted by Kunimatsu et al. (2015) used the tanks with similar capacity as this work. However, it is necessary to carry out more experiments using smaller oil tank models representing 500kL or 1000kL.

The oil-tank was placed (L) distance behind the location of pipes. The force transducer was attached to the tank from the above as in Fig. 6.4. L was considered to be 0.35 m, 0.60 m and 0.85 m respectively, representing the distance of 35 m, 60 m and 85 m between the pipes and the oil-tanks in full-scale as listed in Table 6.1. The oil-tank was partially immersed in calm water depth of about 2~3 cm, with the gap of 1~2 mm between the tank bottom and the floor

in order not to disturb with the force measurements. However, this 1 mm gap is small enough to neglect the flow through this gap. 3 wave gauges and 2 velocity meters were attached in the same positions as Experiments 1 in Section 6.1. The natural frequency of the force measurement system including the force transducer, model oil tank and metal rod attached to the wave basin was measured. First, the force measurement system was attached to the wave flume in the same setting as the experiments, with the model tank partially immersed in water. Then, natural frequency was measured by giving an impact load to the model tank and by taking Fast Fourier Transform (FFT) on the time history of force measurements. 10 times of measurements were carried out and the average natural frequency was 17.297Hz, with ±0.0515Hz of error which is ±0.3% of the average value and acceptable.

6.2.2 Experiments 2: Results and discussions

Figure 6.5 shows the comparison of time series of water elevation and flow velocity measurements recorded by wave gauge WG03 and velocity transducer VS2, respectively. At least five runs of test were carried out for each case in order to obtain acceptable reproducibility. It was observed that the flow features including the incident wave heights and wave elevations were very similar for each case. As shown in Figure 6.6, the maximum incident wave heights measured at WG01 for all cases varied in an acceptable margin, with the average value of 0.125 m and standard deviation of 0.004 m which is acceptable error of approximately 3%. Then, samples for each test case are selected and presented as in Fig 6.5. Both velocity and elevation showed significant decrease for the cases of flexible pipes attachment (Case 2_2, 2_3 and 2_4).

From the time series of velocity and elevation measurements (Fig. 6.5), both velocity and elevation were observed to increase between time = 15 ~ 22. After this time, backwash occurred, with the velocities being negative while elevations were still positive.

The maximum wave heights measured behind the pipes (WG03_max) are shown in Fig. 6.6. Over 20 percent of reduction was observed in WG03_max. These values are smaller than 33.85 percent reduction observed in Experiments 1 because of the wave run-up to the oil-tank, leading to higher elevation measurements.

Then, the maximum momentum flux was computed using the velocity and elevation values measured by VS2 and WG03, respectively, using the equations showed in Section 6.1.2. First, unsteady momentum flux was calculated by Eq 6.1. Then, the average and standard deviations of the maximum momentum flux for each test run were calculated using Eq 6.2 and 6.3. From Fig. 6.7, the peak momentum flux was observed to decrease by 55%, 48% and 49% for Cases 2_2, 2_3 and 2_4, respectively. The marginally smaller reduction results for Cases 2_3 and 2_4 compared to Case 2_2 is caused by flow re-establishment due to larger distances between the flexible pipes and oil tank.

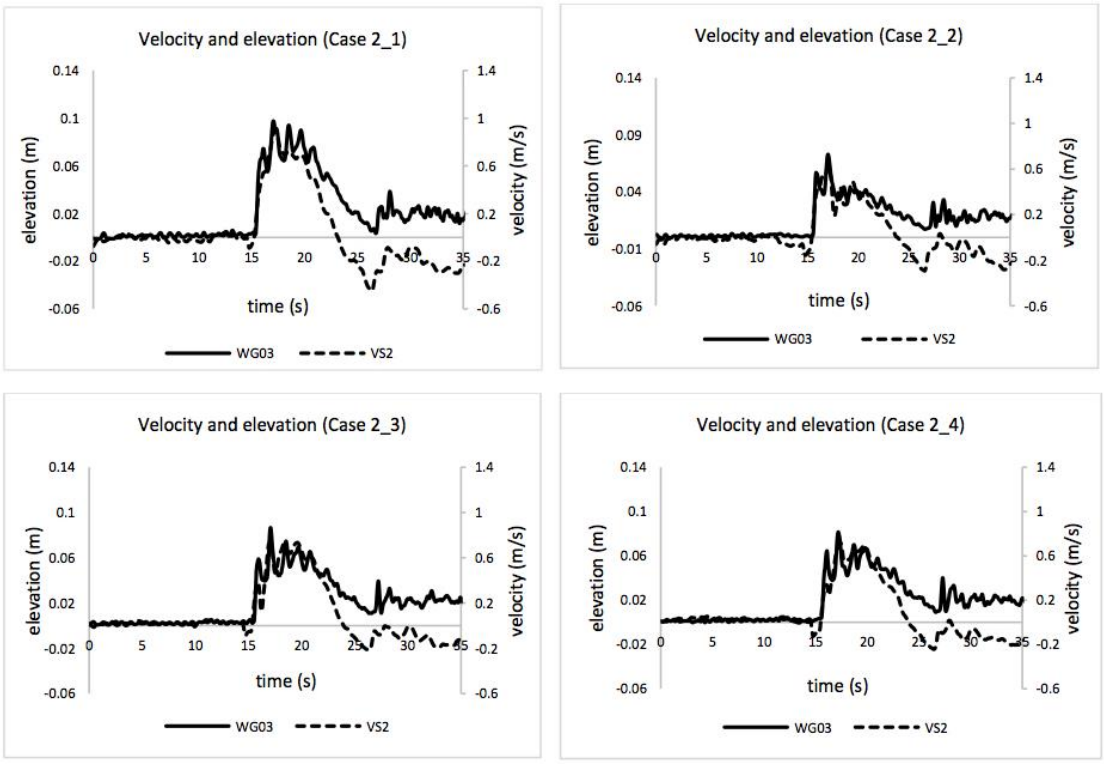

Fig. 6.5 Comparison of flow velocity and elevation measured behind the pipes (solid lines: elevation, dash lines: velocity) for Cases 2_1 to 2_4

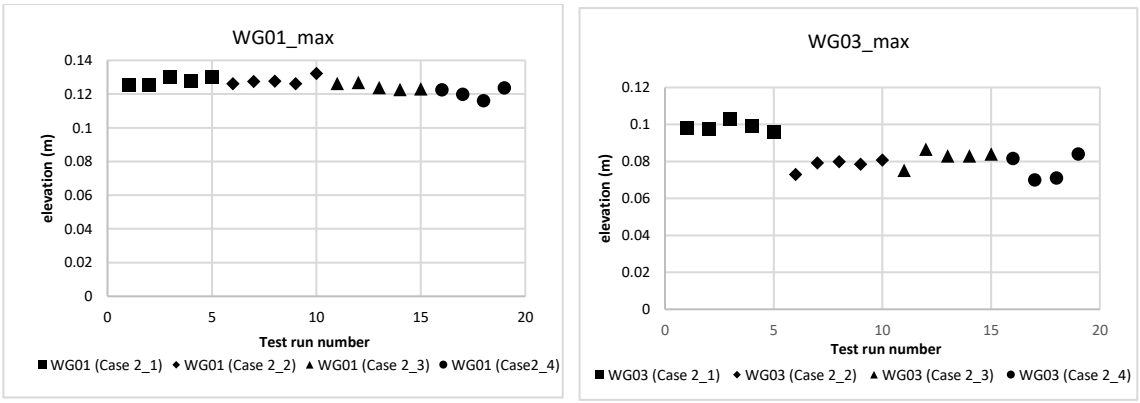

Fig. 6.6 Maximum wave elevations measured at WG01 and WG03

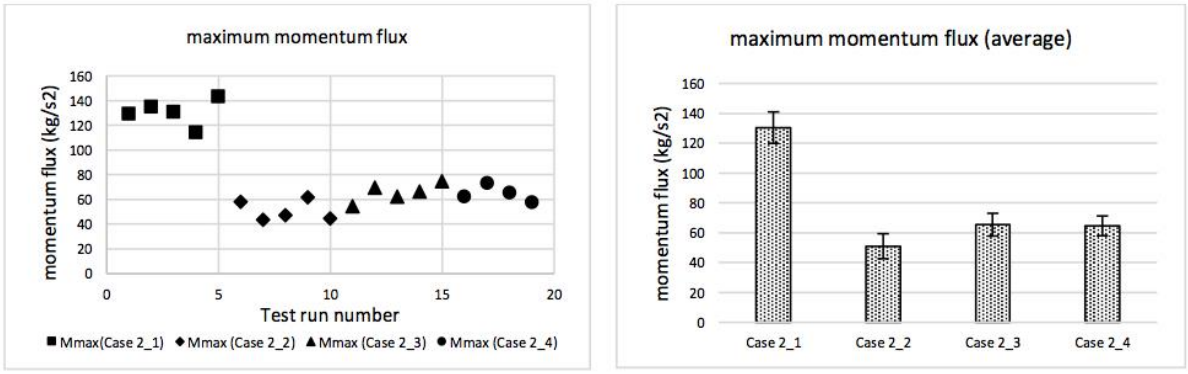

Fig. 6.7 Comparison of maximum momentum fluxes and comparison of average values for each case

Hydrodynamic forces acting on the oil tank in horizontal and vertical directions are compared in Fig. 6.8. As the distance between the flexible pipes and model oil tank increased, reduction rate of the horizontal forces decreased. While reduction of horizontal force was around 40%, the reduction of vertical force was significantly lower compared to horizontal force.

Unsteady hydrodynamic force acting on a cylindrical structure by a surface wave can be estimated using Morison's equation (Morison et al., 1950). Kunimatsu et al. (2015) experimentally studied the usability of Morison's equation in predicting tsunami load on oil tanks. Araki et al. (2016) confirmed the applicability of Morison's formula in tsunami load

estimation by improving Kunimatsu's work. According to Morison's equation, unsteady tsunami force acting on a cylindrical oil tank can be calculated by the following formula:

$$dF = \frac{1}{2} C_D \rho_{water} |u| u D \, dS + C_M \rho_{water} \dot{u} \frac{\pi D^2}{4} dS \quad (6.5)$$

Where, dF is the tsunami force acting on a small segment of the tank in the horizontal direction, C_D is the drag coefficient of the tank, C_M is the inertia coefficient and u and $\dot{u}$ represent unsteady flow velocity and acceleration for each segment, respectively. D is the diameter of the oil tank and dS is the length of a single small segment being considered. Horizontal force acting on the oil tank, $F_{x\_calculated}$ can be obtained by integrating, yielding:

$$F_{x\_calculated} = \frac{1}{2} C_D \rho_{water} |u| u D \eta + C_M \rho_{water} \dot{u} \frac{\pi D^2}{4} \eta \quad (6.6)$$

where, η is the time-dependent wave elevation measured in front of the model tank. C_D and C_M values were chosen using Reynolds' number (Re) and Keulegan-Carpenter number (KC). These numbers are calculated as:

$$Re = \frac{U_{max} D}{\upsilon} \quad (6.7)$$

$$KC = \frac{U_{max} T}{D} \quad (6.8)$$

Where, υ is the viscosity of the fluid and T is the period of wave. U_{max} is the amplitude of the velocity oscillations which is assumed to the maximum velocity measured by velocity transducer, VS2. From the measurements shown in Fig. 6.5, $Re = 1.3\text{x}10^5$ and $Re = 0.96\text{x}10^5$ were obtained while $KC = 48$ and $KC = 40$ were obtained, for no pipes and with pipes cases, respectively. From these results, $C_M = 2.0$ and $C_D = 1.2$ were considered. These values agree with the recommended values by FEMA (2008) and also with the values used by Kunimatsu et al. (2015) and Araki et al. (2016) in their experiments.

The vertical buoyant force by the tsunami was estimated by buoyancy equation:

$$F_{z\_calculated} = \rho_{water} g \eta \frac{\pi D^2}{4} \quad (6.9)$$

where, $g = 9.81\ ms^{-2}$ is gravity constant and η is the elevation measured by WG03.

Comparisons of calculated unsteady horizontal and vertical forces and measured values are shown in Fig. 6.8. The dash lines represent the calculated horizontal and vertical forces using Eq 6.6 and Eq 6.9, respectively while the solid lines represent the measured values. The largest horizontal forces occurred at the second peak for all cases. Morison's equation could predict these largest values well but the first peak values were underestimated. This is due to smaller velocity values during the first peak although the elevation was high, as in Fig. 6.5. Therefore, it can be deduced that the first peaks of horizontal forces were contributed to hydrostatic force acting on the surface of the oil-tank in the inflow direction. This hydrostatic force was caused by difference of water elevation between the front and behind surfaces of the tank during the first peak. Then, the velocity increased and the calculated forces showed good agreements with measured ones.

On the other hand, for the vertical forces calculated by buoyancy force formula in Eq 6.9, the first peaks were larger than measured values. This is because in the buoyant force formula, it is assumed that the elevation on the front and behind surfaces of the tank are the same while in the experiments, the behind elevation was smaller due to pressure drop. Thus, vertical force by simple buoyant formula were overestimated.

As shown in Fig. 6.5, backwash flow occurred, causing negative velocities in the inflow direction. Meanwhile, the elevation was positive and decreasing. Consequently, the horizontal forces were measured to be positive between time = 15 ~ 22 seconds while vertical forces were observed to be positive between time = 15 ~ 27 seconds as in Fig. 6.8. By comparing Fig 6.5 and Fig. 6.8, it can be concluded that Morison's equation could predict such behavior as backwash well.

As shown in Fig. 6.7, the maximum incident wave heights differed by a small margin. In order to eliminate this uncertainty (2.98% error), the maximum horizontal and vertical forces are normalized as follows:

$$F_{x_{normalized}} = \frac{F_{x\_max}}{\frac{1}{2}\rho_{water} g D \eta^2} \tag{6.10}$$

$$F_{z_{normalized}} = \frac{F_{z\_max}}{\rho_{water} g \eta (\frac{\pi D^2}{4})} \tag{6.11}$$

where, F_{x_max} is the maximum horizontal force and F_{z_max} is the maximum vertical force, respectively.

The normalized horizontal and vertical forces are shown in Figure 6.9. The use of flexible pipes could reduce nearly 40% of horizontal force. The reduction rate gradually decreased as the distance between the pipes and model tank increased due to flow re-establishment behind the wake region, causing higher velocities and elevations than inside the wake.

From Fig 6.3c of Section 6.1.2 and Fig. 6.7 of current section, it was observed that around 50% of momentum flux was decreased by the use of flexible pipes. However, only 40% of horizontal force reduction was observed. This difference was caused by overflow of water above the model tank for the no pipes case (Case 2_1), reducing the effective cross-sectional area of the oil tank attacked by tsunami-like wave. This caused the measured forces smaller than those corresponding to momentum flux. On the other hand, for the cases with the attachment of flexible pipes, the elevation was reduced effectively. Consequently, no overflow above the oil tank occurred. Therefore, the effective cross-sectional area as well as measured hydrodynamic force was not reduced for Cases 2_2, Case 2_3 and Case 2_4. It is expected that better results would be obtained by increasing the height of the oil tank. Tank models of different dimensions should be tested as a future work. Vertical force reduction was not significant (less than 10%) compared to horizontal force reduction.

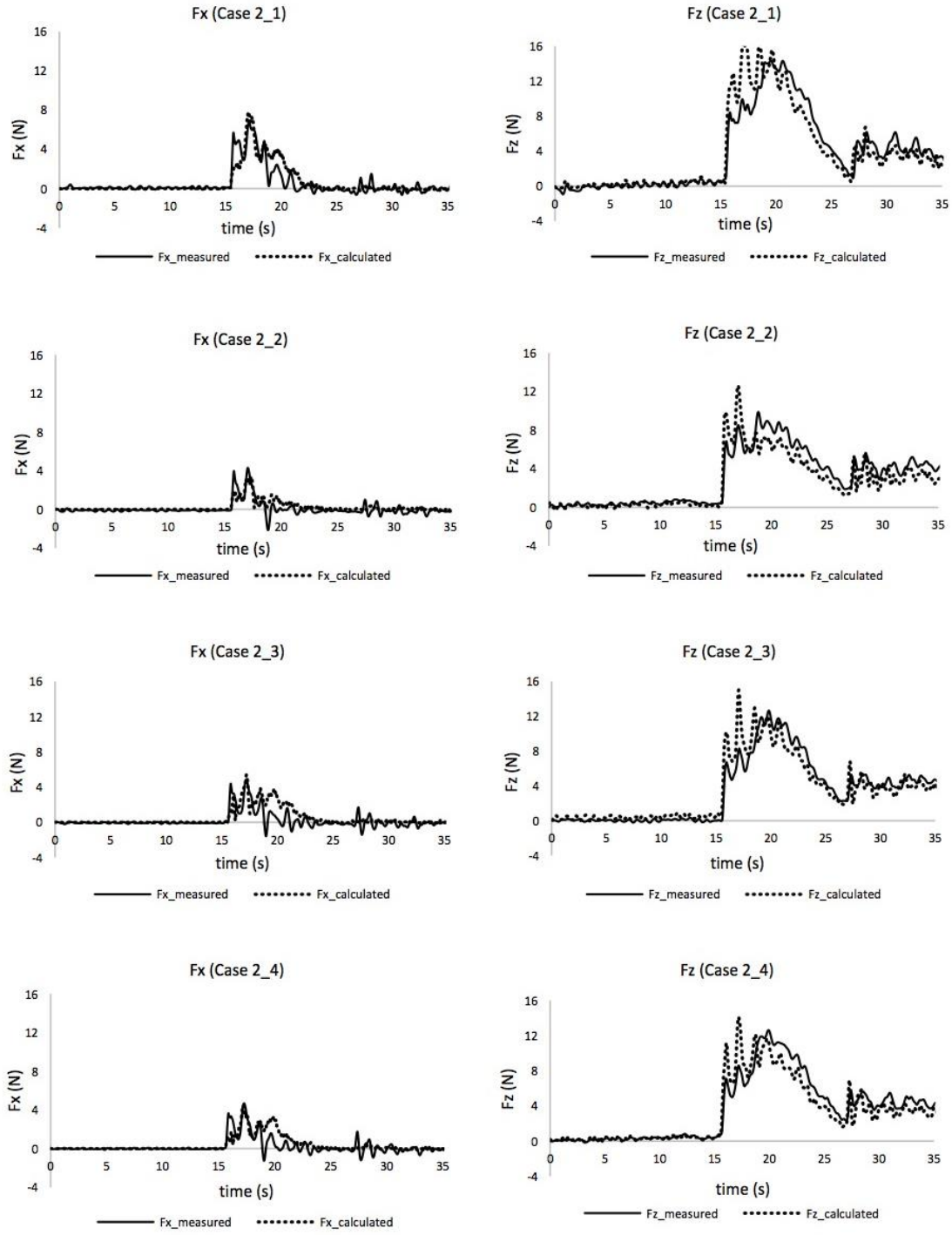

Figure 6.8 Comparison of hydrodynamic forces (solid lines: measured, dash lines: calculated) for Cases 2_1 to 2_4

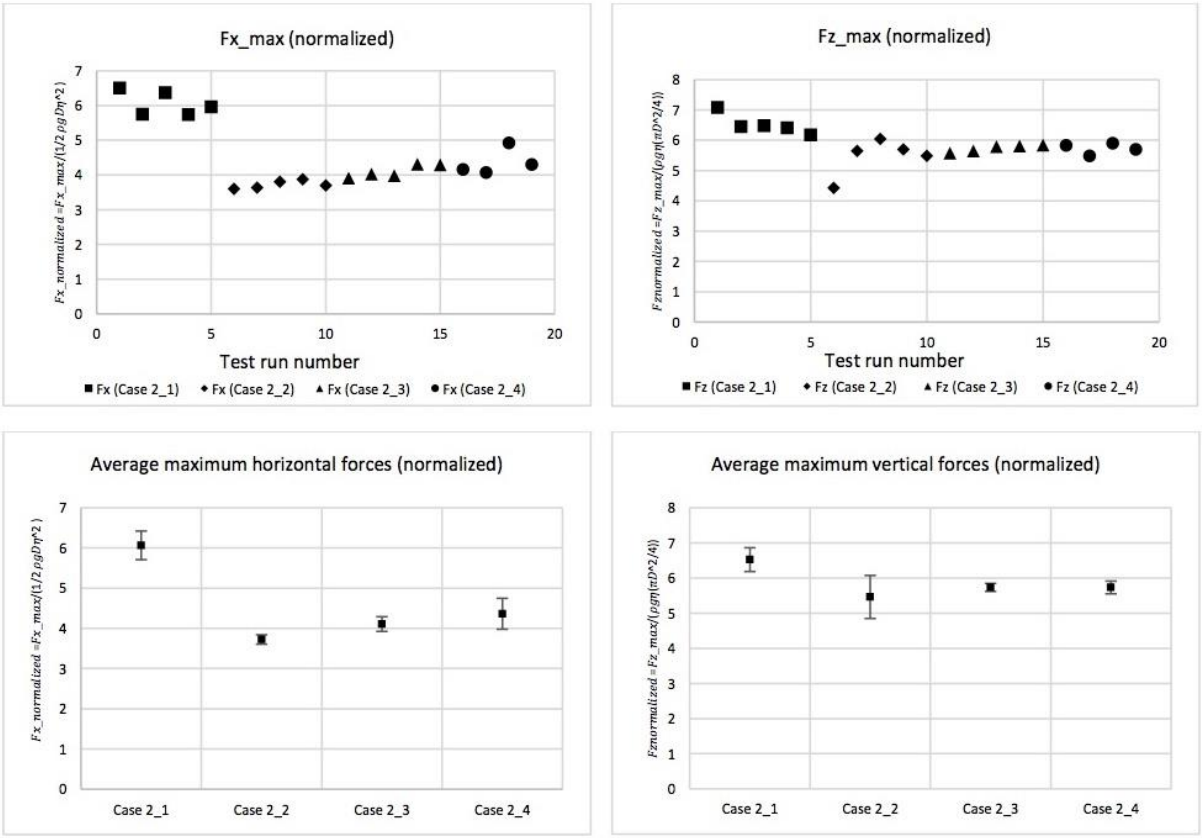

Figure 6.9 Comparison of maximum normalized forces from all test runs and comparison of average values for each case

6.3 Experiments 3: Analysis on the reduction of hydrodynamic forces acting on a cylindrical tank installed on an earth bank with a dyke

In the previous sections, the reduction performance of momentum flux and hydrodynamic forces acting on a semi-submerged oil tank by the pipes was studied. However, in order to understand the real-world phenomena, it is necessary to include the effect of tsunami run-up to the earth-bank. Therefore, a scale-model earth-bank was used in the experiments. The oil tank was considered to be located on this bank. Moreover, the effect of dyke walls around the oil storage tanks is also included.

6.*3.1 Experiments 3: Experimental setup*

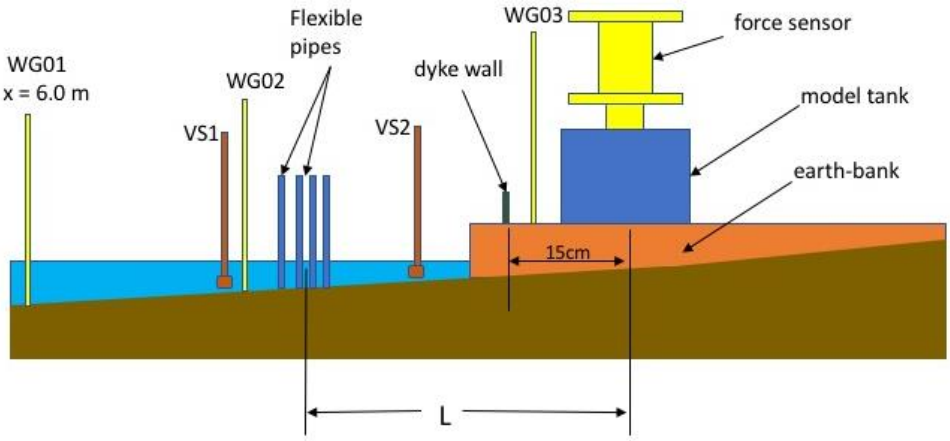

Fig. 6.10 Schematics of experimental setup for Experiments 3

The setup of Experiments 3 is shown in Fig. 6.10. An earth-bank was firmly attached to the floor of tsunami wave flume using bolts and nuts, on which the model oil tank was located. The same scale-model oil tank as Experiments 2 was employed in these experiments. The height of the force sensor was adjusted in a way that the gap between the base of model oil tank and the top of earth-bank is approximately 1 mm, in order to avoid strong flows between these two surfaces. The height of the bank is 10 cm while the water depth was 5 cm.

A 1 cm high scale-model dyke wall was attached to the scale model earth-bank such that the dyke wall covers the whole width of the wave flume. The wave gauge WG03 was placed between the dyke wall and the oil-tank instead of the previous position in Experiments 2 in order to eliminate the effect of earth bank on the water surface elevation. However, the velocity sensor VS2 was placed at the same position as Experiments 2 because it is necessary to initially place this sensor underwater for proper functioning.

Table 6.2. Different cases of Experiments 3 based on the distance between the pipes and oil tank

Case	**L**	**Flexible pipe**	**Dyke wall**
Case 3_1	~	No	No
Case 3_2	0.35 m	Yes	No
Case 3_3	0.60 m	Yes	No
Case 3_4	0.85 m	Yes	No
Case 3_5	~	No	Yes
Case 3_6	0.35 m	Yes	Yes
Case 3_7	0.60 m	Yes	Yes
Case 3_8	0.85 m	Yes	Yes

8 experimental conditions of were investigated as summarized in Table 6.2. L is the distance between the flexible pipes and the centre of oil tank as shown in Fig. 6.10. For consistency, this distance L was kept the same as the previous experiments in Section 6.2.

6.3.2 Experiments 3: Results and discussions

In Experiments 3, the effect of the earth-bank on the flow velocity was relatively large compared to flexible pipes. Consequently, the measurement results of electromagnetic velocimetry VS2 showed relatively smaller flow velocities compared to Experiments 2. Therefore, only wave elevation was used to discuss the effectiveness in tsunami reduction by the flexible pipes and the dyke wall.

Firstly, the effect of the distance between flexible pipes and an earth-bank on the flow phenomena is discussed. Fig. 6.11a shows the run-up of the wave for the case with no

application of flexible pipes. Wave breaking occurred and the wave became a turbulent bore as illustrated in Fig. 4.3b. By the time the head of the bore hits the earth-bank, splash occurrs and then the bore continus to run-up the bank as in Case 3_1 illustrated in Fig. 6.11a. For Case 3_2, the tsunami bore ran up the flexible pipes and crossed over the pipes, directly reaching to the top of earth-bank, without attacking the vertical wall of the earth-bank (Fig. 6.11b). Therefore, in this case, the effect of earth-bank was not apparent, causing similar flow patterns as the no-pipes case. Thus, only approximately 10 percent reduction was observed in the time histories of wave elevation shown in Fig. 6.12.

On the other hand, when the pipes were installed farther away from the earth-bank as in Case 3_3 and Case 3_4 (shown in Fig. 6.11c and 6.11d, respectively), the wave head that passed over the pipes was observed to attack the earth-bank. At this time, the momentum was decreased by both the flexible pipes and the earth-bank. Therefore, better reductions in wave elevation were observed.

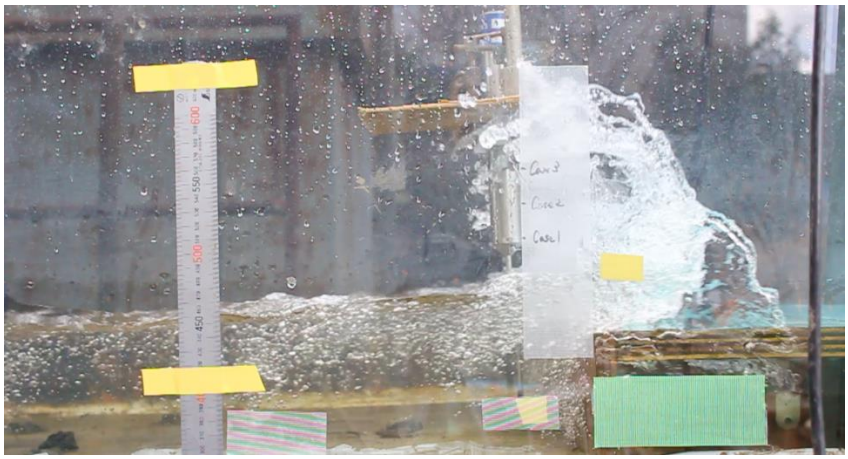

(a)

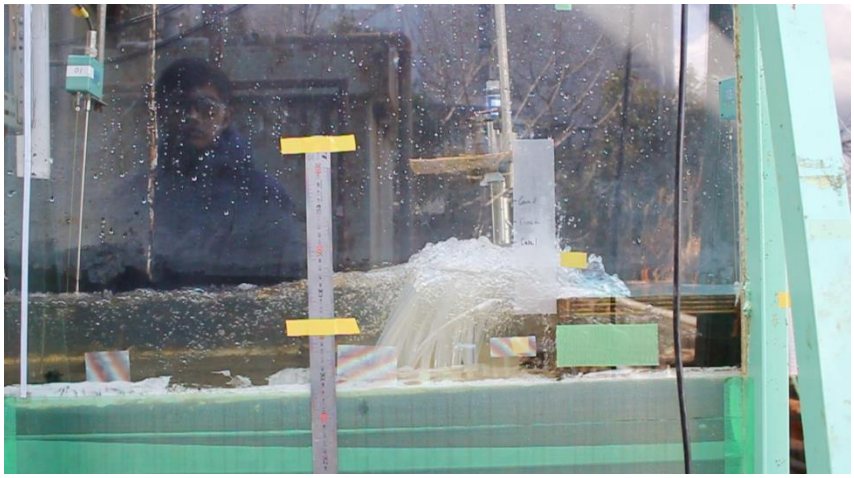

(b)

(c)

(d)

Fig. 6.11 Photos of Experiments 3 with no attachment of dyke wall, comparing the effect of flexible pipe locations (a) Case 3_1 (b) Case 3_2 (c) Case 3_3 (d) Case 3_4

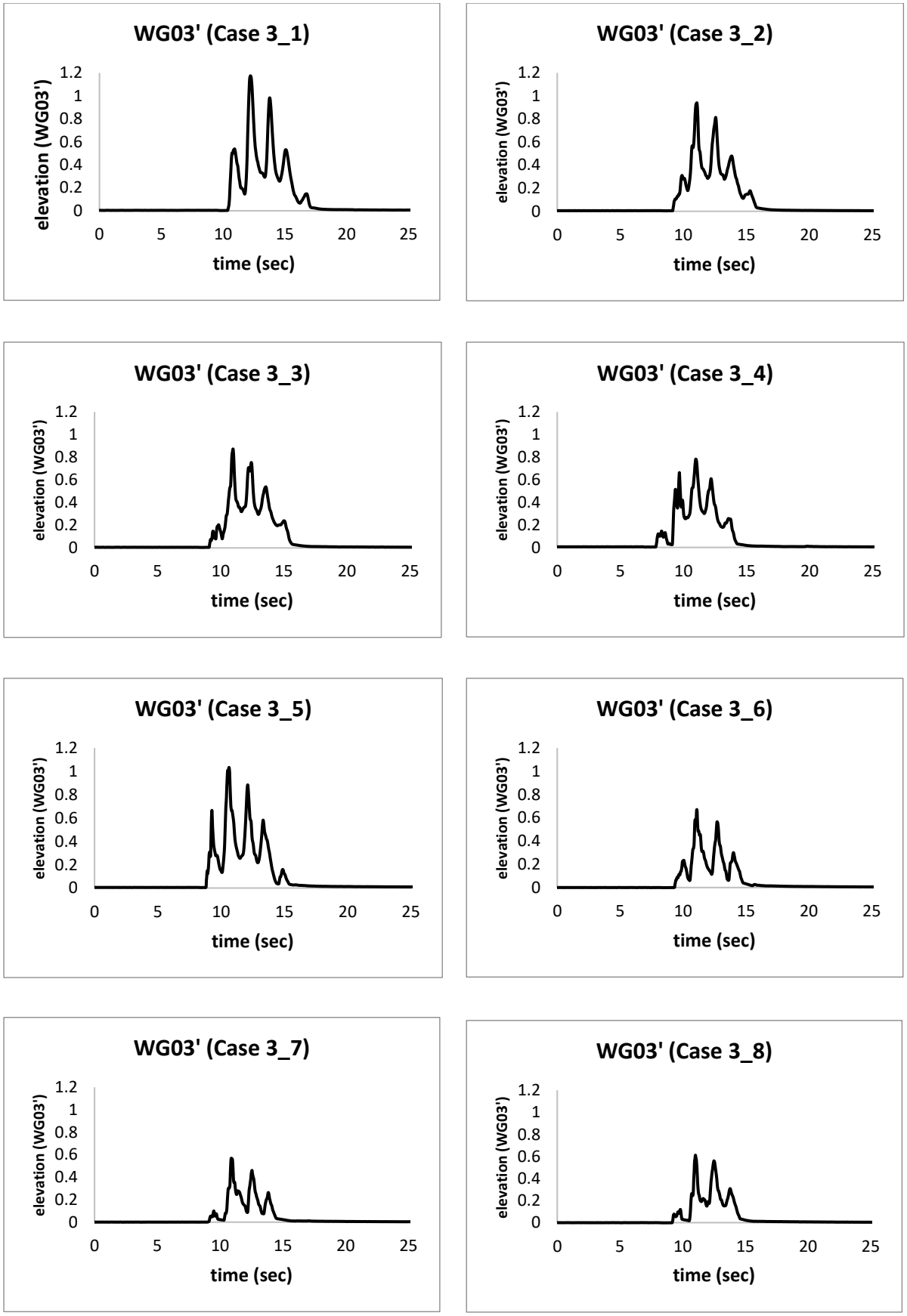

Fig. 6.12 Comparison of elevation behind the pipes and dyke wall (measured at wave gauge WG03)

Fig. 6.12 shows the time series of non-dimensional water elevation recorded by WG03 on top of the earth bank calculated as:

$$WG03' = \frac{2\ WG03}{\max(WG01)} \tag{6.10}$$

,where max(WG01) is the maximum incident wave elevation measured by wave gauge WG01. This non-dimensionalization is necessary to cancel out the error in the incident wave heights.

By attaching the flexible pipes at 35cm in front of the tank as in Case 3_2, the first wave head was marginally reduced. However, no significant reduction in elevation was observed for the rest of the wave. This is due to the tsunami bore flowing over the pipes and ran up the earth-bank directly as explained in Fig. 6.11b. For larger distances between the flexible pipes and the earth wall, better reductions were observed as shown in Case 3_3 and Case 3_4 of Fig. 6.12, with the first wave almost eliminated in these cases. Cases 3_5 of this same figure shows the elevation when a dyke wall is attached with no installation of flexible pipes while Case 3_6, 3_7 and 3_8 show the results for experiments with both dyke wall and flexible-pipe arrangement included. By comparing Case 3_1 and 3_5, the dyke wall alone showed no significant wave elevation reduction. Since the dyke wall height is 1 cm, the wave easily flowed over the dyke wall without decreasing its surface elevation. However, it is assumed that overall momentum flux showed reductions by decreasing the flow velocity. By comparing Case 3_6, 3_7 and 3_8 to Case 3_1, the combined effect of flexible pipes and dyke wall could reduce maximum elevation by approximately 40 percent while the whole time histories showed the wave trains were significantly dissipated with some waves nearly eliminated.

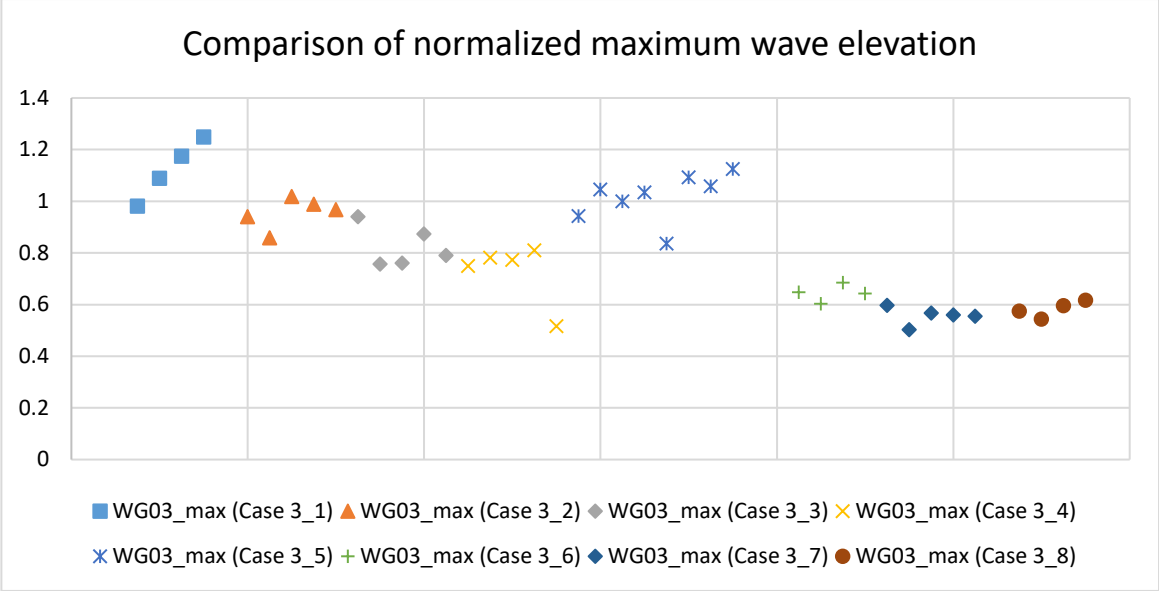

Fig. 6.13 Comparison of normalized maximum wave elevation

The comparison of normalized maximum elevations are shown in Fig. 6.13. These elevations were also normalized by using Eq. 6.10. The case with dyke wall without flexible pipes (Case 3_5) showed high elevations slightly higher than Case 3_2 in which the effectiveness of the pipes was not significant. However, with the attachements of flexible pipes, the maximum wave elevations were observed to decrease by more than 40 percent.

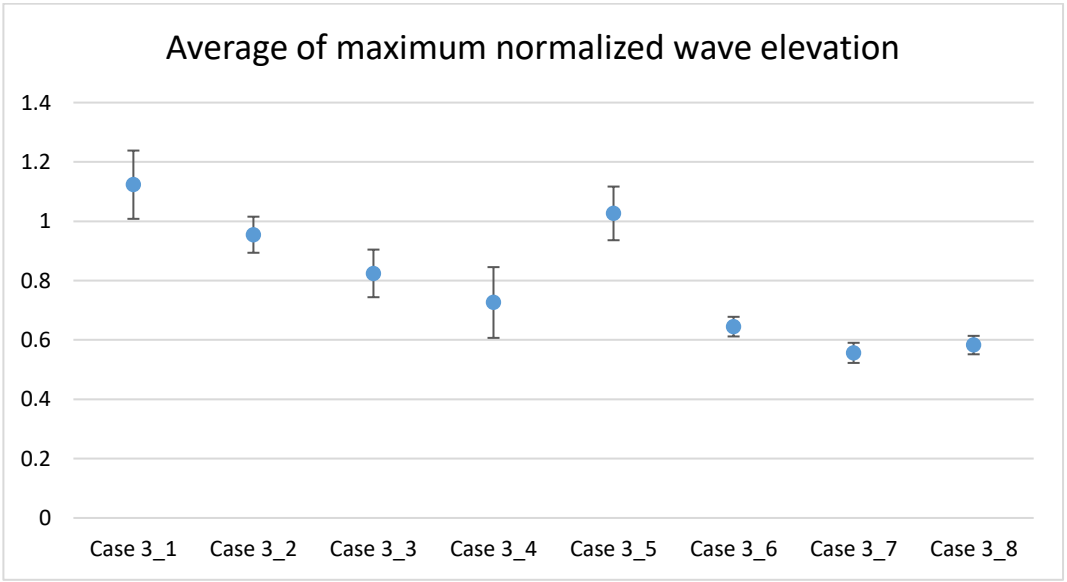

Fig. 6.14 Average values of maximum normalized wave elevation

The average values of maximum normalized wave elevations are summarized in Fig. 6.14. The wave reduction increased as the distance between the pipes and the earth bank due to the interaction explained in Fig. 6.11. By the installation of dyke wall, elevation was further reduced; up to 50 percent of maximum wave elevation could be reduced by the combined effect of flexible pipes, earth wall and the dyke walls.

Comparison of time histories of horizontal forces is shown in Fig. 6.15. From the time histories of horizontal force, it was observed that the shape of the horizontal force is similar to water elevation in Fig. 6.12. In Case 3_1, the horizontal force was comprised of four smaller consecutive waves. Although the wave forces were reduced by using flexible pipes alone (as in Case 3_2) or dyke wall alone (Case 3_5), the wave pattern was similar to no countermeasure case (Case 3_1). However, when these two countermeasures were combined, the smaller first and fourth waves could be eliminated while the middle wave crests were reduced by over 50 percent as in Case 3_7 and Case 3_8.

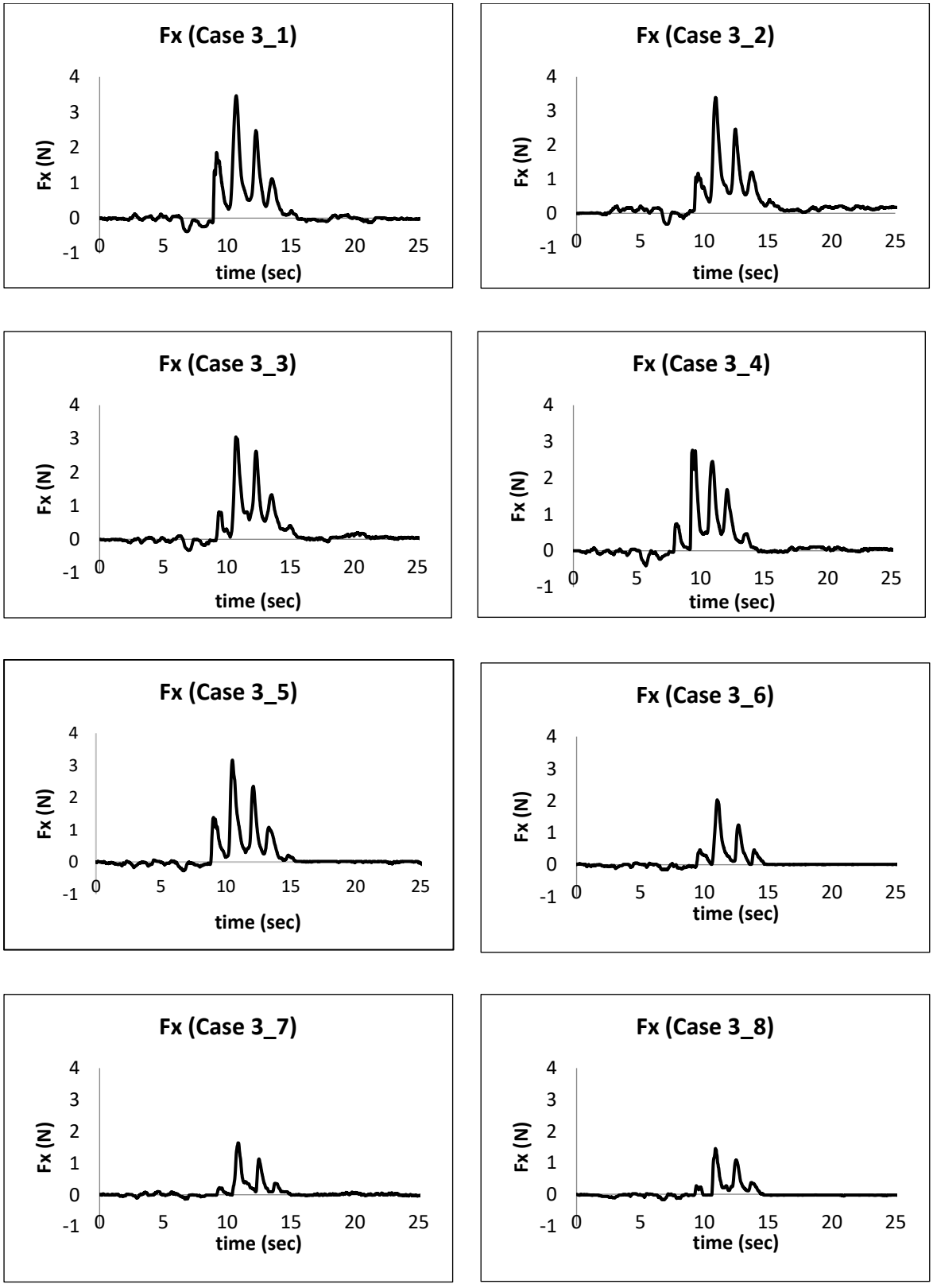

Fig. 6.15 Comparison of hydrodynamic dynamic forces acting on the cylindrical oil tank in horizontal direction

The normalized maximum horizontal forces are summarized in Fig. 6.16 and 6.17. These forces were normalized by using Eq. 6.10 of previous section in order to eliminate the effect of difference in incident wave conditions. From Fig. 6.17, 25 percent of force reduction was observed by flexible pipes alone. Another 25 percent could be further reduced by the dyke wall.

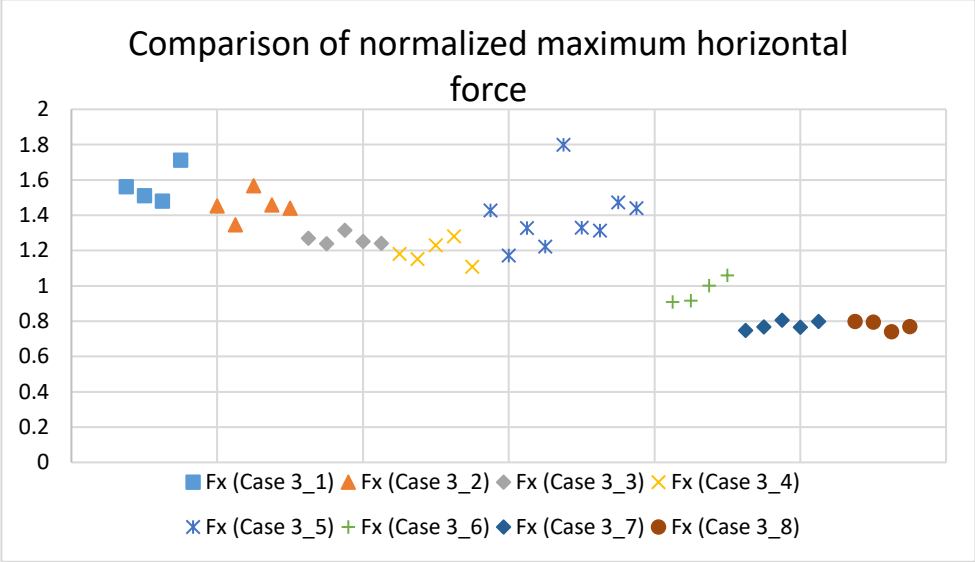

Fig. 6.16 Comparison of normalized maximum horizontal force acting on the oil tank

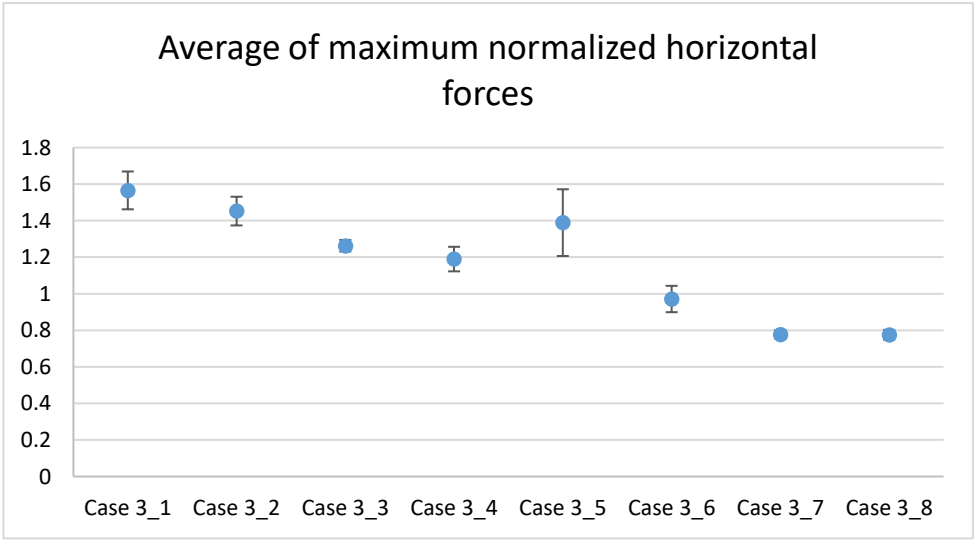

Fig. 6.17 Average values of maximum normalized horizontal forces

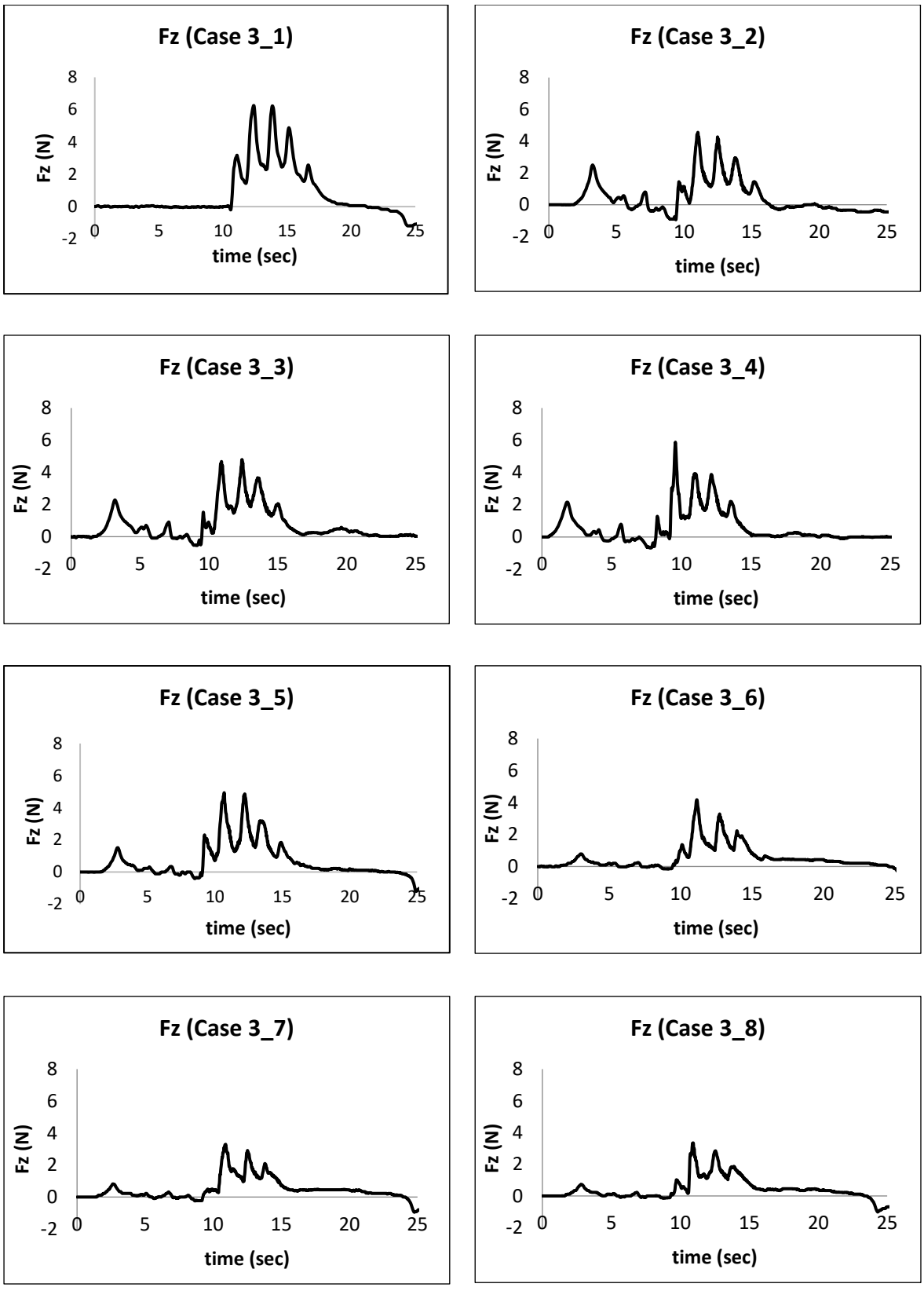

Fig. 6.18 Comparison of hydrodynamic forces acting on the cylindrical oil tank in vertical direction

Time histories of vertical forces acting on the oil tank are shown in Fig. 6.18. Although wave force reduction was observed, the reduction rate was lower than horizontal forces for both flexible pipes and dyke walls. The pattern of wave force in vertical direction was similar to that of wave elevation because the dominant vertical force is the buoyant force. Thus, the reduction showed similar patterns. On the other hand, the horizontal force depends on both wave elevation and flow velocity. Since the flexible pipes reduces both wave elevation and flow velocity by wave dissipation, the horizontal force reduction was more significant than vertical force reductions.

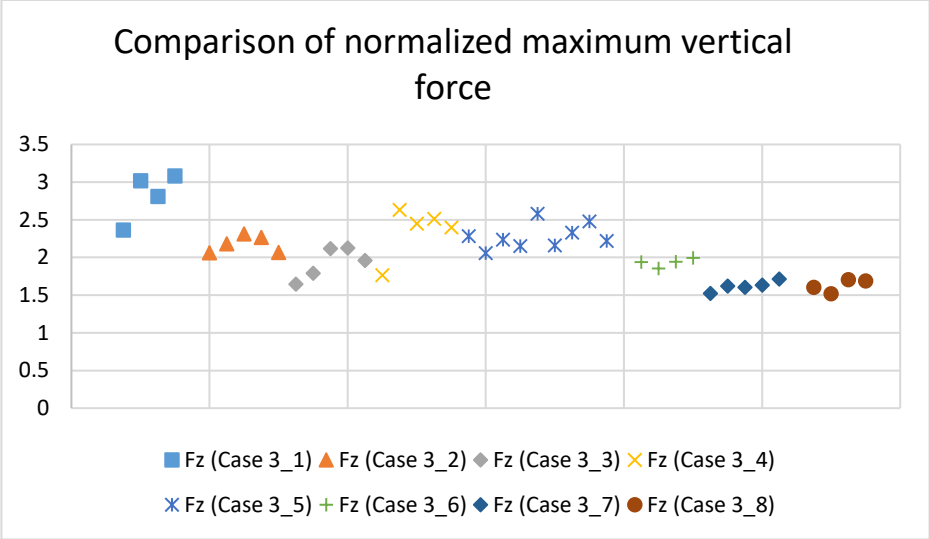

Fig. 6.19 Comparison of normalized maximum vertical force acting on the oil tank

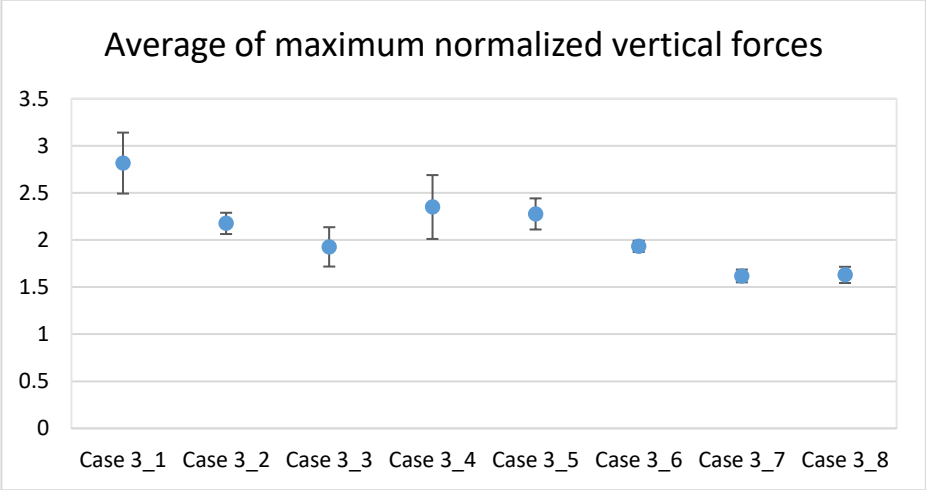

Fig. 6.20 Average values of maximum normalized vertical forces

Fig. 6.19 and 6.20 summarize the maximum normalized vertical forces. From these figures, up to 35% of vertical force reduction was observed. However, since the main focus of this work is in reduction of horizontal hydrodynamic forces action on the tank, 50 percent reduction of horizontal force was acceptable although the reduction of vertical force was observed to be relatively smaller.

6.4 Conclusions

Three kinds of experiments were conducted to assess the wave momentum reduction of flexible pipes with a quasi 2D assumption by cancelling out 3D effects by using a flexible-pipe arrangement that covers the width of the tsunami wave flume. From Experiments 1, it was observed that the unsteady momentum flux could be reduced up to 50 percent. This results can be used to estimate the reduction of tsunami drag force on a general structure such as a residential area or an industrial zone. From Experiments 2, Morison Equation was found to be useful in estimating the unsteady horizontal force acting on energy storage tanks by a tsunami wave. It was observed that 40% of hydrodynamic force acting on the cylindrical oil tank decreased when flexible pipes were installed. Better results are expected for different sizes of model tanks. From Experiments 3, the interaction of the flexible pipes location and the earth bank could be observed. The change in run-up pattern led to different water elevations and different hydrodynamic forces on the scale-model tanks. The combined effect of flexible pipes and dyke wall could reduce horizontal force by nearly 50 percent. These results can be used in consideration of the location of the flexible pipes and the design of the energy storage facilities which are vulnerable to tsunami attacks.

From these series of experiments, it can be concluded that flexible pipes were effective in tsunami damage reduction by decreasing the wave elevation, momentum and wave forces. The attachment of dyke walls could significantly improve this effectiveness.

Chapter 7

Numerical study on the deformation of flexible pipes under the tsunami load

This chapter deals with the analysis on the feasibility of flexible pipes for practical implementation by means of structural analysis. One of the main requirements for the practical implementation of flexible pipes system is the estimation of the pipes deformations under the tsunami load. If the deformations are large, the effective projected area of the pipes will largely decrease in such a way that the effectiveness in flow reduction would become very low. Thus, it is necessary to properly estimate the deformations under tsunami.

The deformation of a full-scale pipe is estimated by Absolute Nodal Coordinate Formulation (ANCF) method based on the extrapolated bending stiffness (EI) values from experiments. In this approach, hydrodynamic forces acting on the flexible pipe are computed using drag force and inertia force formulas. The structural solver with ANCF uses these forces and computes deformations of the pipe. Therefore, it is necessary to estimate the drag coefficients of a cylindrical structure.

In the first part of this chapter, the drag coefficients of a flexible pipe is investigated numerically by considering flow induced oscillations using a 3D computational fluid structure interaction technique. In the second part, the deformation of scale model silicone pipes used in Chapter 6 is computed based on the drag coefficients obtained from the first part of this chapter.

Finally, the deformation of full-scale pipes under the flow velocities corresponding to Level 2 tsunami will be predicted.

7.1 Numerical study on the fluid structure interaction of a finite length cylinder

As previously mentioned, it is important to use proper drag coefficients for circular cylinders in the computation of flexible pipe deformation. Flow around a circular cylinder has been a problem of interest for researchers and engineers working on fluid dynamics problems. Zdravkovich (1997) compiled the experimental results of flow around rigid 2D cylinders, including the laminar to turbulence transitions, drag coefficients and vortex patterns. For the flexible pipes in the full-scale and (1:100) model-scale, the Reynolds numbers are in the order of 10^6 and 10^3, respectively. The corresponding drag coefficients for 2D rigid circular cylinders are around 1.2 and 0.8, respectively. However, if flow induced oscillations such as vortex induced vibrations occurred, the drag coefficients might vary from the above values. Therefore, it is necessary to investigate the flow around a flexible circular cylinder as an unsteady 3D fluid-structure problem.

Vortex shedding and vortex induced vibration (VIV) of circular cylinders have been a field of interest for several researchers. For instance, Williamson (1996) measured the drag and lift coefficients as well as the Strouhal numbers of rigid quasi-2D cylinders at Reynolds Number ranges (100 – 460). Huera-Huarte and Bearman (2009) experimentally studied the wake structures and vortex-induced vibrations of a long flexible cylinder. On the numerical side, various methods have been employed to investigate the vortex-induced vibration phenomena, including Arbitrary-Lagrangian-Eulerain (ALE) framework with finite element solvers for both fluid and solid (Zhao and Cheng, 2014 and Mittal and Navrose, 2013), finite volume method with multiple 2D strips (Wan et al., 2017) and vorticity-velocity formulation with overset grid (Marshall and Renjitham, 2012). These approaches only employ 2D or 3D cylinders with fixed ends.

7.1.1 Finite volume framework for 3D fluid structure interaction

The purpose of this study is to estimate the drag coefficient of a finite length 3D circular cylinder fixed at the bottom end to a non-slip floor. This problem can be distinguished into two parts: computation of the pipe as a cantilever-beam-like structure and computation of the flow physics around a finite length fixed cylinder.

Since the pipe has a large tendency to suffer from severe bending motion in the inflow direction as well as the cross-flow direction, it is necessary to use a fully 3D CFD method with an unstructured flow solver with mesh deformation supportn. In this work, finite volume framework was employed for both fluid and structure solvers.

7.1.1.1 Governing equations of fluid and solid solvers

In this research, the fluid was assumed to be an incompressible single-phase Newtonian fluid. The governing equations for this fluid are unsteady Navier-Stokes equations for an incompressible fluid:

Mass conservation of fluid:

$$\nabla \bullet v_f = 0 \,, \tag{7.1}$$

Momentum conservation of fluid:

$$\rho_f \frac{\partial v_f}{\partial t} + \rho_f (\nabla v_f)(v_f - v_m) = \nabla \cdot \sigma_f \,, \tag{7.2}$$

where the stress tensor σ_f can be expanded as:

$$\sigma_f = -p_f I + \rho_f \upsilon_f (\nabla v_f + (\nabla v_f)^T) \tag{7.3}$$

where v_f is the fluid velocity while v_m is the mesh velocity. The density and kinematic viscosity of the fluid are ρ_f and υ_f, respectively. These equations are discretized in OpenFOAM framework using second order finite volume schemes. Foam-extend 3.2 was used in this work.

Gauss Linear discretization schemes were employed for discretizing the spatial terms. Pressure Implicit with Separation of Operators (PISO) algorithm was used for the pressure-velocity coupling to solve the transient incompressible flow. Mesh motion is calculated by solving the Laplace equation of displacements at the interface computed by the solid solver:

$$\nabla \bullet (\gamma \nabla u_m) = 0 \,, \tag{7.4}$$

where u_{m} is the point velocity vector field of the mesh and γ is the variable diffusivity coefficient. The diffusivity coefficient γ is computed by quadratic inverse distance method due to its higher stability than other approaches such as linear inverse distance or exponential inverse distance methods (Jasak and Tukovic, 2006) as following:

$$\gamma = \frac{1}{l^2} \,, \tag{7.5}$$

where l is the distance from the moving boundary. By solving for u_m, the point displacement field for each time step can be obtained as:

$$x_{new} = x_{old} + u_m \Delta t \,, \tag{7.6}$$

where x_{new} and x_{old} are the position vector fields for new and old time-steps, respectively while Δt is the time step.

For the structural part, finite volume based solver with total Lagrangian Approach (Cardiff, 2012 and Jasak and Tukovic, 2007) was employed. Linear elastic solid was assumed. However, for the solver, non-linear approach was chosen due to the tendency of large deformations. The governing equations for constitutive model using total Lagrangian approach are as follows:

Momentum conservation of solid:

$$\int_{\Omega_S} \rho_S \frac{\partial \delta v_S}{\partial t} d\Omega_S - \oint_{\Gamma_S} n_u \bullet (2\mu + \lambda) \nabla \delta u_S \Gamma_S = \oint_{\Gamma_S} n_u \bullet q d\Gamma_S + \int_{\Omega_S} \rho_S \frac{\partial \delta f_b}{\partial t} d\Omega_S \tag{7.7}$$

where tensor q includes non-linear deformations and traction terms for coupling with fluid:

$$q = \mu(\nabla \delta u_S)^T + \lambda tr(\delta u_S) I - (\mu + \lambda)\nabla \delta u_S + \mu \nabla \delta u_S \bullet (\mu \nabla \delta u_S)^T + \frac{1}{2}\lambda(\nabla \delta u_S : \nabla \delta u_S) I + \sum_S \bullet \nabla F^T + \delta \sum_S \bullet \nabla F^T \quad (7.8)$$

where the second Piola-Kirchhoff stress tensor for St. Venant-Kirchhoff material is defined as:

$$\sum_S = 2\mu E + \lambda tr(E) I \,, \quad (7.9)$$

where the Green Lagrangian strain tensor E is defined as:

$$E = \frac{1}{2}[\nabla u_S + (\nabla u_S)^T + \nabla u_S \bullet (\nabla u_S)^T] \,, \quad (7.10)$$

where v_s is the velocity vector field , u_s is the displacement vector field of the solid defined as:

$$u_S = r_{new} - r_{old} \,, \quad (7.11)$$

where r_{new} and r_{old} are the position vector fields of the current and initial configurations, respectively.

λ and μ are Lamé coefficients. F is the deformation gradient tensor which can be written as:

$$F = I + (\nabla u_S)^T \,, \quad (7.12)$$

where I is the unit tensor.

Equations 7.1 and 7.2 were discretized in finite volume domain using second order Gauss Linear schemes. Temporal terms in both fluid and solid solvers are discretized using implicit second order Euler backward difference schemes due to their stability and second order accuracy although the computational cost was higher than first order schemes.

7.1.2 Partition algorithm with Aitken relaxation

7.1.2.1 Partition algorithm

The fluid and solid solvers were coupled by means of a strong coupling algorithm shown in Fig. 7.1. For each time step, firstly, fluid mesh motion is computed by solving Eq. 7.4 by mesh motion solver. In this research, velocityLaplacian mesh motion solver provided by OpenFOAM was used to solve the mesh motion equation with quadratic inverse distance approach (Eq. 7.5 and 7.6). Then, the flow field is solved by a transient PISO solver and pressure and viscous forces are computed for the moving boundary. These forces are fed to the total Lagrangian solid solver via Eq. 7.8. After solving the momentum equation of the solid (Eq. 7.7), the displacement vector field is obtained. By comparing this computed displacement field with the previous iteration step, residuals are calculated and convergence is checked. When converged, next time step is computed in the same procedure. If the convergence criteria is not resolved, the displacement field computed by the solid solver is relaxed and the procedure is restarted from the point of the fluid mesh motion solver until the convergence is arrived or the iteration count is larger than a pre-defined value. This algorithm is a kind of fixed-point under-relaxation scheme with dynamic relaxation. The relaxation factor is computed by Aitken's relaxation algorithm due to its good convergence at surprisingly low computational cost (Kuttler and Wall, 2008).

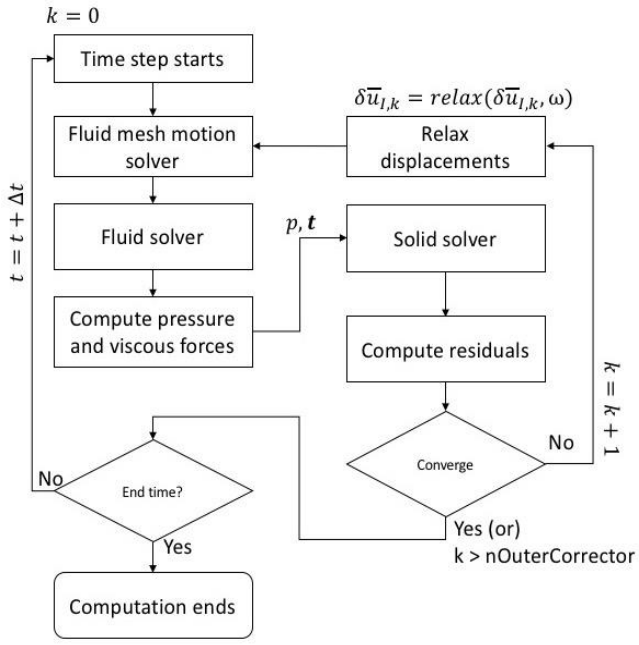

Fig. 7.1 Flow chart of partition algorithm

7.1.2.2 Aitken relaxation scheme

As shown in Fig. 7.1, the displacements are relaxed by using a relaxation factor ω_k. The relaxed displacement for the fluid domain $\delta u_{f,k}$ and relaxation factor ω_k are calculated as:

$$\delta u_{f,k} = \delta u_{f,k-1} + \omega R_k , \tag{7.13}$$

where $\delta u_{f,k}$ is the relaxed displacement for the fluid mesh for current time step, $\delta u_{f,k-1}$ is the displacement vector field of fluid for previous time step.

$$\omega_k = -\omega_{k-1} \frac{R_{k-1}(R_k - R_{k-1})}{\left\| R_k - R_{k-1} \right\|^2} , \tag{7.14}$$

where ω_{k-1} is the relaxation factor from previous time step. The residuals are computed from previous two time steps as:

$$R_k = \delta u_{S,k} - \delta u_{f,k-1} \tag{7.15}$$

$$R_{k-1} = \delta u_{S,k-1} - \delta u_{f,k-2} , \tag{7.16}$$

where $\delta u_{S,k}$ and $\delta u_{S,k-1}$ are the displacement vector fields generated by the solid solver for k^{th} and k-1^{th} time-steps while $\delta u_{f,k-1}$ and $\delta u_{f,k-2}$ are the displacement fields of fluid mesh for k-1^{th} and k-2^{th} time steps, respectively. According to the comparisons of Gatzhammer et al. (2012), quasi-Newton least squares (QLNS) coupling algorithm showed faster and more stable convergence than fixed-point iteration with Aitken adaptive relaxation approach. However, during this research, by comparing the simulations between QLNS and Aitken, Aitken showed more stable coupling with faster convergences.

7.2 Results and discussions of 3D fluid structure interaction analysis

7.2.1 Finite Length 3D Rigid Circular Cylinder

7.2.1.1 Numerical model

Before carrying out the simulations for flexible cylinder, rigid cylinder simulations were carried out. The computational domain is shown in Fig. 7.2. The cylinder diameter is 0.015m which is a 1:100 scaled-down model of full-scale pipes having 1.5m diameter. The inlet is a uniform flow with a fixed velocity while the outlet is a zero gradient velocity outlet with zero pressure. The cylinder and the bottom wall are non-slip walls whereas the other walls are slip walls.

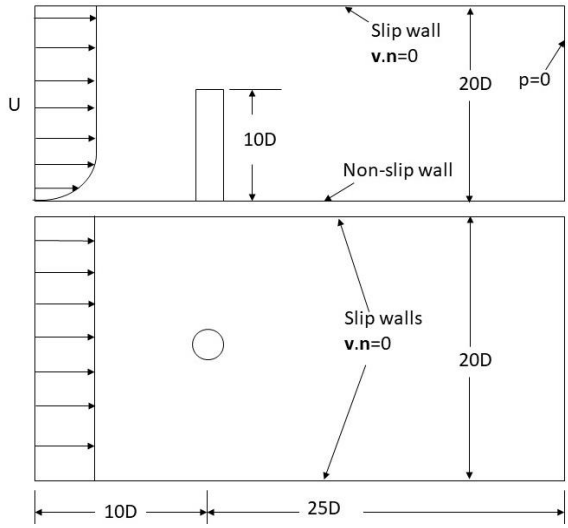

Fig. 7.2 Computational domain

7.2.1.2 Mesh convergence test

Computational mesh for the fluid domain was generated using OpenFOAM's native unstructured-mesh generator snappyHexMesh. 3 meshes of different coarseness were tested as a mesh convergence test. The parameters used in this test are shown in Table 7.1. The cylinder diameter and inlet velocity are defined in a way such that these values correspond to 1:100 scale model of full-scale situation. The density of fluid is similar to that of water while the

kinematic viscosity is different in order to keep Reynolds' numbers below 1000. The time step is set at $5x10^{-4}$ in order to satisfy the CFL condition. Turbulence modeling is not applied due to high computational cost although the wake became partially turbulent at Re = 750.

Table 7.1 Simulation parameters for mesh convergence test

Fluid Parameters	Value	Unit
Inflow velocity, U	0.5	m/s
Cylinder diameter,D	0.015	m/s
Aspect Ratio, L/D	10	
Fluid density, ρ_{fluid}	1000	kg/m^3
Kinematic viscosity, ν_{fluid}	$1x10^{-5}$	m^2/s
Δt	$5x10^{-4}$	s
Re	750	

Table 7.2 Summary of mesh convergence test results

Mesh	Cell Count	Re	C_D	C_L (rms)	St
Coarse	325101	750	0.813	0.011	0.145
Medium	1585283	750	0.849	0.039	0.172
Fine	2707669	750	0.851	0.041	0.172
Experiment (Anderson,2005)	-	1000	0.9	-	-
Experiment (Heseltine, 2003)	-	20000	0.9	0.8	0.17

The drag and lift coefficients, C_D and C_L are computed using the formulas:

$$C_D = \frac{F_D}{\frac{1}{2}\rho_{fluid} S U^2} \tag{7.17}$$

$$C_L = \frac{F_L}{\frac{1}{2}\rho_{fluid} S U^2}, \tag{7.18}$$

where S is the projected area of the cylinder defined as $S = DL$, where D is the cylinder diameter and L is the cylinder length, respectively. F_D and F_L are drag and lift forces obtained by integrating the pressure and viscous stress fields around the cylinder surface.

Strouhal number is calculated from the vortex shedding frequency f_v, using:

$$St = \frac{Df_v}{U} \tag{7.19}$$

The vortex shedding frequency f_v was calculated by taking the Fast Fourier Transform (FFT) of fluctuating lift coefficients.

The results of mesh convergence test are shown in Table 7.2. From this test, the drag coefficients of medium and fine mesh showed good agreements with Anderson (2005). On the other hand, Strouhal number was compared to Heseltine's measurements (2003) of finite length cylinder of aspect ratio 9 at higher Reynolds numbers.

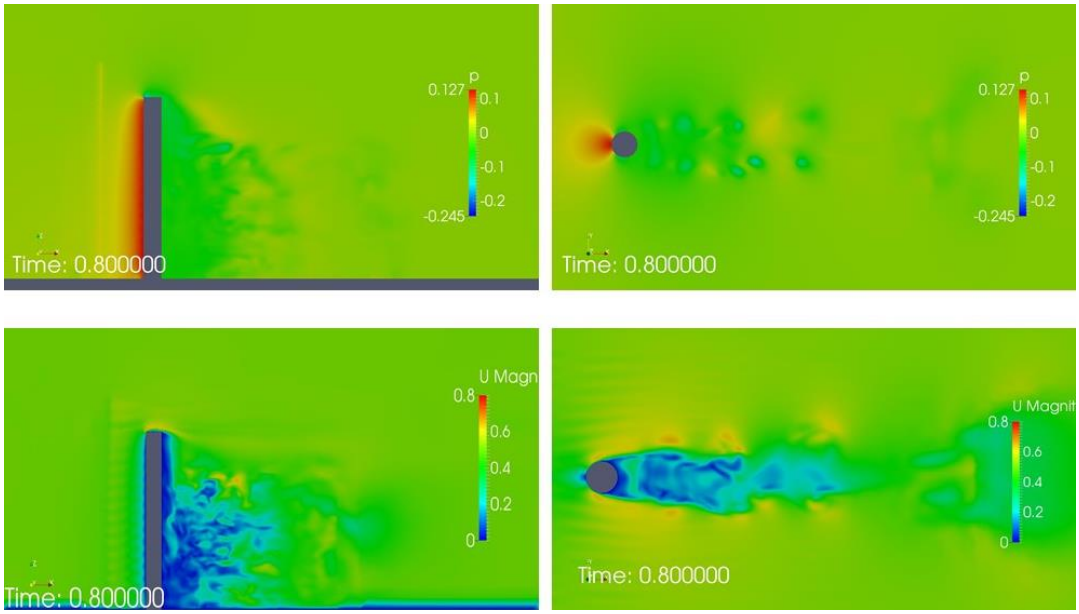

Fig. 7.3 Pressure and velocity contours for rigid cylinder at U=0.5 m/s (top left) pressure field at side view (top right) pressure field from top view (bottom left) velocity field side view (bottom right) velocity field side view

The pressure and velocity fields are shown in Fig. 7.3 for qualitative assessments. Both drag and lift coefficients were smaller than 2D configurations in literature because the wake was relatively weak for one third of the cylinder length from the tip as in Fig. 7.3. Small perturbations were observed in front of the cylinder. This was caused by relatively fine mesh with second order numerical schemes. However, such perturbations did not show significant influence on the drag and lift coefficients as well as the vortex shedding frequency. From this mesh convergence check, medium mesh with approximately 1.58 million finite volumes was chosen for the fluid structure interaction problem as a compromise between computational cost and accuracy.

7.2.1.3 Rigid cylinder at multiple inflow velocities

For the purpose of comparison between rigid and flexible cylinders, the computations for rigid cylinders at multiple inflow velocities were done. These cases are summarized in Table 7.3. Drag and lift coefficients were calculated by Eq 18 and 19, respectively while the Strouhal number was calculated by Eq. 20 using the vortex shedding frequency. The drag coefficients marginally decreased as the Reynolds' number increased from 450 to 750 while the lift coefficients saw a slight increase. The Strouhal frequencies for cases R2, R3 and R4 were observed to be very similar while the result of R1 was lower. This might be due to weaker vortex shedding for finite length cylinder with a flat bottom at fully laminar regime.

The time histories of C_D and C_L for case R2 as well as the frequency spectrum of vortex shedding are shown as an example in Fig. 7.4. Non-dimensionalised time $t^*=Ut/D$ is used where U is the inflow velocity (m/s), t is the time in seconds and D is the cylinder diameter. From the frequency spectrum, it was observed that vortex shedding occurred at two main frequencies at 3.503Hz and 6.305Hz while there were other smaller fluctuations caused by complex 3D vortex shedding along the length of the cylinder.

Table 7.3 Summary of multiple inflow velocities

Case	Inflow velocity, U (m/s)	Re	C_D	C_L (rms)	f_v (Hz)	St
R1	0.2	300	0.867	0.009	2.083	0.156
R2	0.3	450	0.877	0.023	3.503	0.175
R3	0.4	600	0.857	0.027	4.604	0.172
R4	0.5	750	0.849	0.039	5.732	0.172

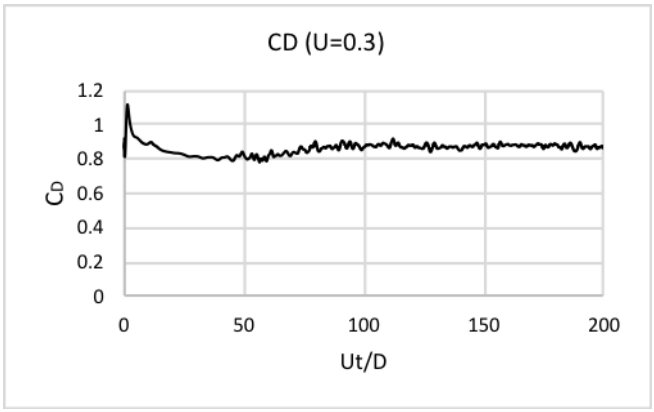

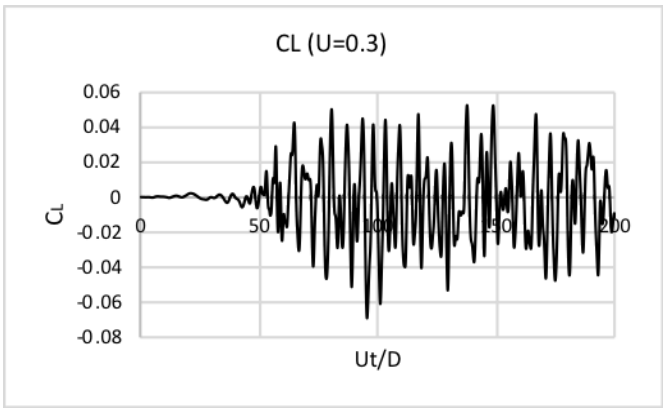

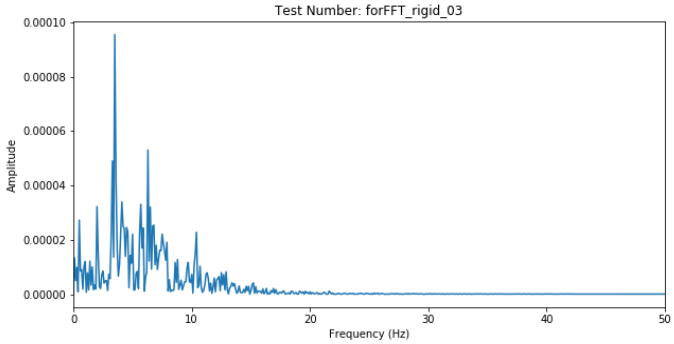

Fig. 7.4 An example of time series of drag coefficeints (top) lift coefficients (mid) and the frequency spectram of (bottom)

7.2.2 Finite Length Flexible Circular Cylinder

7.2.2.1 Numerical model

For the fluid mesh, the mesh chosen in the previous section was again employed. The solid mesh is a hexahedral structured mesh generated by OpenFOAM's native structured mesh generator, blockMesh application and it is composed of 3600 hexahedral elements. The boundary conditions of the fluid domain were set the same as the rigid cylinder case except moving wall boundary condition was applied for the cylinder patch. The fluid and solid meshes are shown in Fig. 7.5 left and right, respectively.

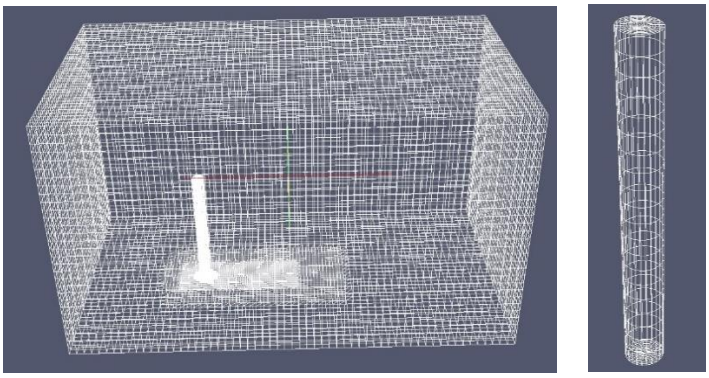

Fig. 7.5 Fluid mesh (left) and solid mesh (right)

The flow parameters for the fluid part were set similar to previous section shown in Table 7.1 and 3. The solid parameters are described in Table 7.4. The mass ratio ($m^*=\rho_{solid}/\rho_{fluid}$) was

assumed to be 1 in order to investigate the behavior of water injected flexible pipes. The Young's modulus E of the cylinder was $5x10^6$ Pa to represent a very flexible material such as rubber.

Table 7.4 Solid parameters for fluid structure interaction computations

Solid parameters	Value	Unit
Solid density, ρ_{solid}	1000	kg/m^3
Poisson's ratio, ν_{solid}	0.4	
Young's modulus, E	$5x10^6$	Pa
Bending stiffness, I	$2.485x10^{-9}$	m^4
Natural frequency, f_n	6.595	Hz
Mass ratio, m*	1	

7.2.2.2 Coupling of fluid and structure solvers

Since flow around a flexible circular cylinder is a highly transient case with very tight coupling between fluid and solid, it is necessary to couple the solvers in a tight manner. Thus, fixed-point relaxation with Aitken adaptive relaxation method explained using equations 7.13 to 7.16 was used. The initial relaxation factor for each time step was considered to be 0.7 in order to accelerate the convergence because of high computational cost.

The bottleneck of computation time was observed to be the solid solver with total Lagrangian approach. The convergence of the solid solver was considered by the residuals of the solid equations (equations 7.10). Since the convergence of the solid solver was very sensitive to relaxation factor, the relaxation factor for the solid computation was considered to be 0.01. For each time step, convergence was obtained in 8-10 Aitken iterations while, the solid solver iteration ranges up to over 1000 iterations for each Aitken iteration step. Time step size of

$5x10^{-4}$ was assigned for both solid and fluid solver in order to satisfy the CFL condition for the fluid computations. An example of relaxation factors, iteration steps and residuals for a time step is illustrated in Fig. 7.6. The horizontal axes represent the number of iteration steps.

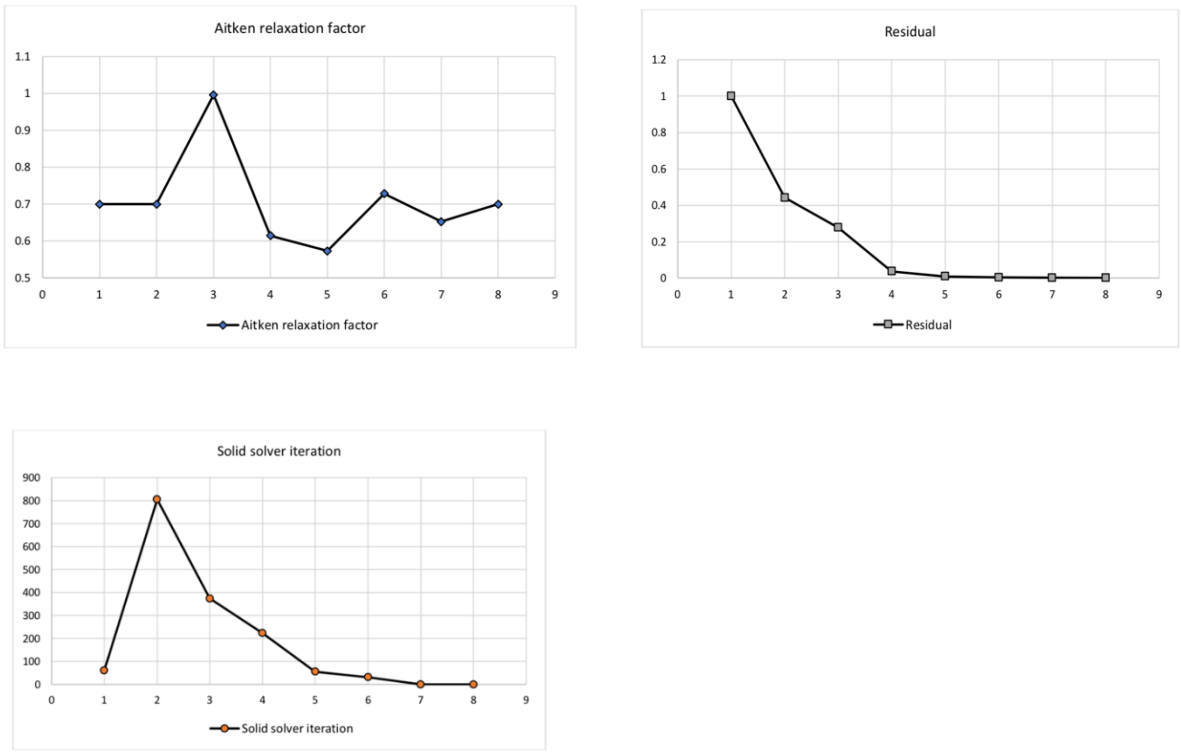

Fig. 7.6 An example of Aitken relaxation factors (top) convergence history (mid) and solid solver iterations (bottom) of a time step

7.2.2.3 FSI simulation results for flexible cylinder

Table 7.5 Simulation cases for flexible cylinder

Case	Inflow velocity, U (m/s)	Re	Ur
F1	0.3	450	3.03
F2	0.4	600	4.04
F3	0.5	750	5.05

Three cases of tests with different inflow velocities (U = 0.3, 0.4 and 0.5 m/s) were carried out having reduced velocities U_r = 3.03, 4.04 and 5.05, respectively as listed in Table 7.5. The side view of the flexible cylinder bending under uniform flow is shown in Fig. 7.7. The wake behind the pipe was more complex and 3-dimensional for F2 and F3 cases. It is contributed by the transition to turbulence for these due to larger Reynolds numbers (Re=600 and 750, respectively) while F1 was relatively larminar compared to the other two cases. As the inflow velocity increased, the deformation in the inflow direction increased.

The vorticity plots in z direction around the cylinder at z=2L/3 (where L is the length of the cylinder) is shown in Fig. 7.8. For F1, vortex shedding was not observed at that plane while for F2, slight vortices were observed. For F3, vortex shedding occurred at z=2L/3 plane. This is due to the domination of viscous effects at Re=450, suppressing vortex shedding. However, at z=L/3 plane, stronger vortex shedding potential was observed for all cases, with the wake much more complicated due to the interaction with the floor surface shown in Fig. 7.9.

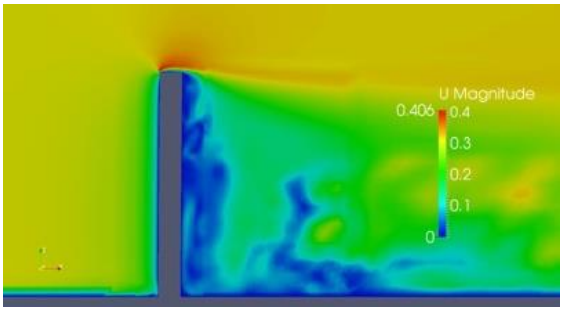

(a)

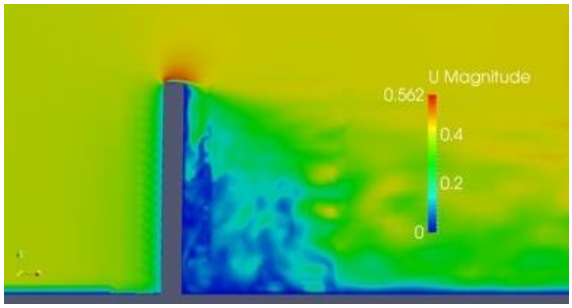

(b)

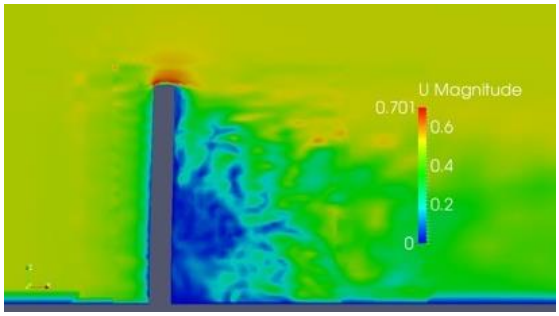

(c)

Fig. 7.7 Side view of flexible cylinder showing velocity field (a) F1: Ur=3.03 (b) F2: Ur=4.04 (c) F3: Ur=5.05

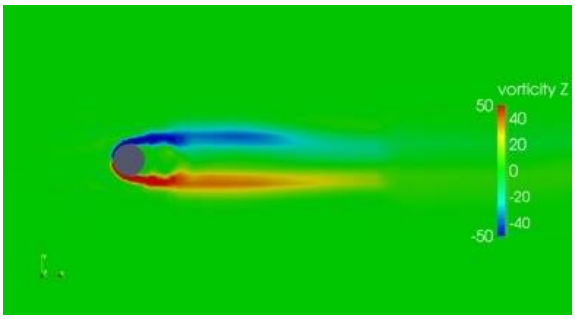

(a)

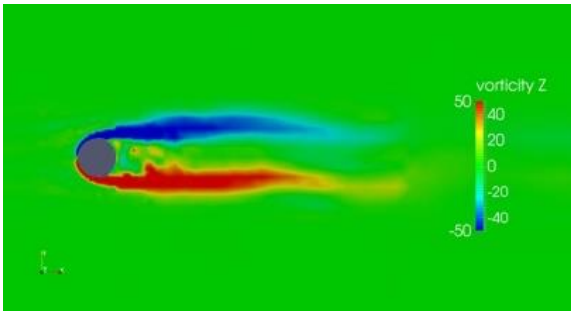

(b)

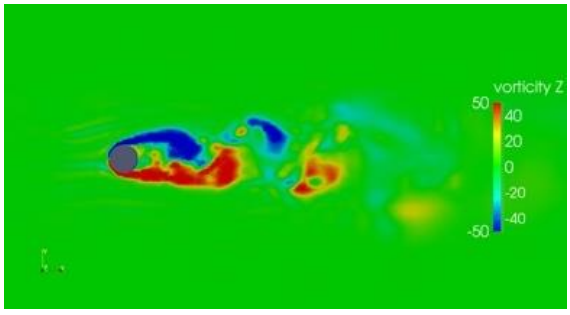

(c)

Fig. 7.8 Top view of the flexible cylinder showing vorticity field at z=2L/3(a) F1: Ur=3.03 (b) F2: Ur=4.04 (c) F3: Ur=5.05

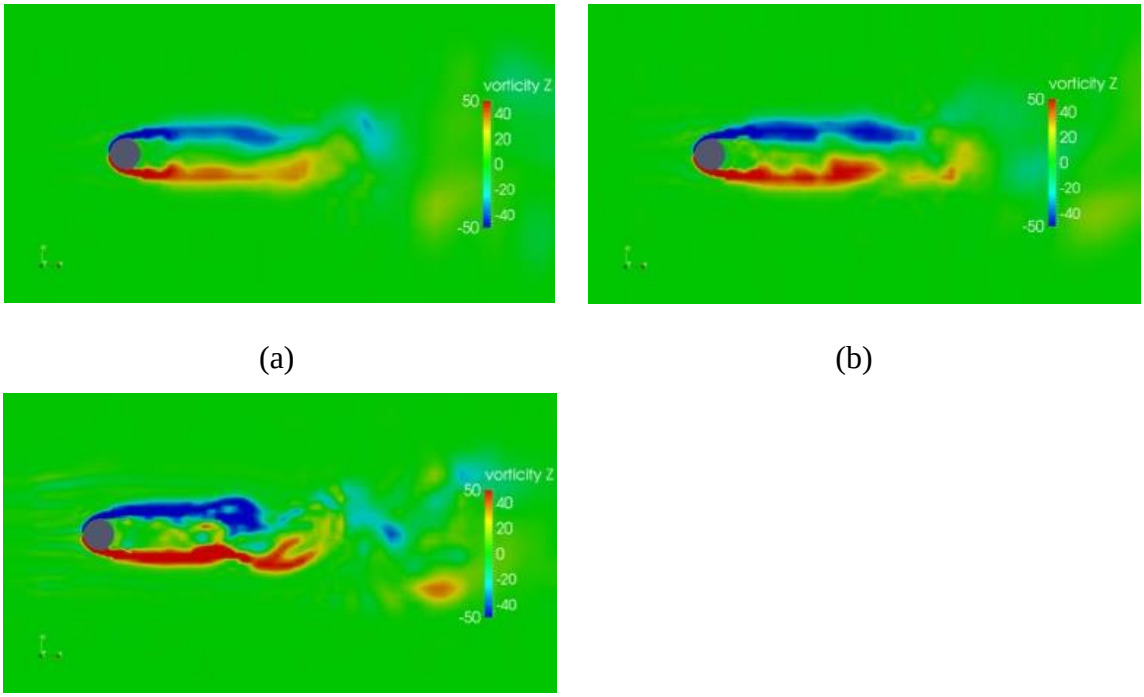

Fig. 7.9 Top view of the flexible cylinder showing vorticity field at z=L/3(a) F1: Ur=3.03 (b) F2: Ur=4.04 (c) F3: Ur=5.05

The time histories of drag and lift coefficients are compared in Fig. 7.11. Time is non-dimensionalized by t*=Ut/D. Since the FSI computations are computationally very heavy, only up to t*=120 was computed. For F1 and F2 cases, VIV was not observed. Consequently, the drag coefficients showed oscillations up to around t*=60 and then, reached to steady state. The initial oscillations are caused by the energy balance between cylinder motion and the internal strain energy. Steady state drag coefficients were found to be around C_D=0.8 (C_D=0.797 and 0.819 for F1 and F2, respectively) which is similar to their rigid counterparts. Slight oscillations were found in C_L values for F1 and F2, with $C_{L(rms)}$=0.003 and $C_{L(rms)}$=0.01 for F1 and F2. Strouhal numbers for F1 and F2 were found to be 0.13 and 0.248, respectively although the oscillation amplitudes of the lift coefficients were significantly smaller compared to F3 where VIV was observed, as in Fig. 7.10. For the F3, St=0.178 was observed, with only one dominant frequency in the spectrum. This is due to the synchronization of all vortices shedding along the whole length of the cylinder as observed in frequency spectra.

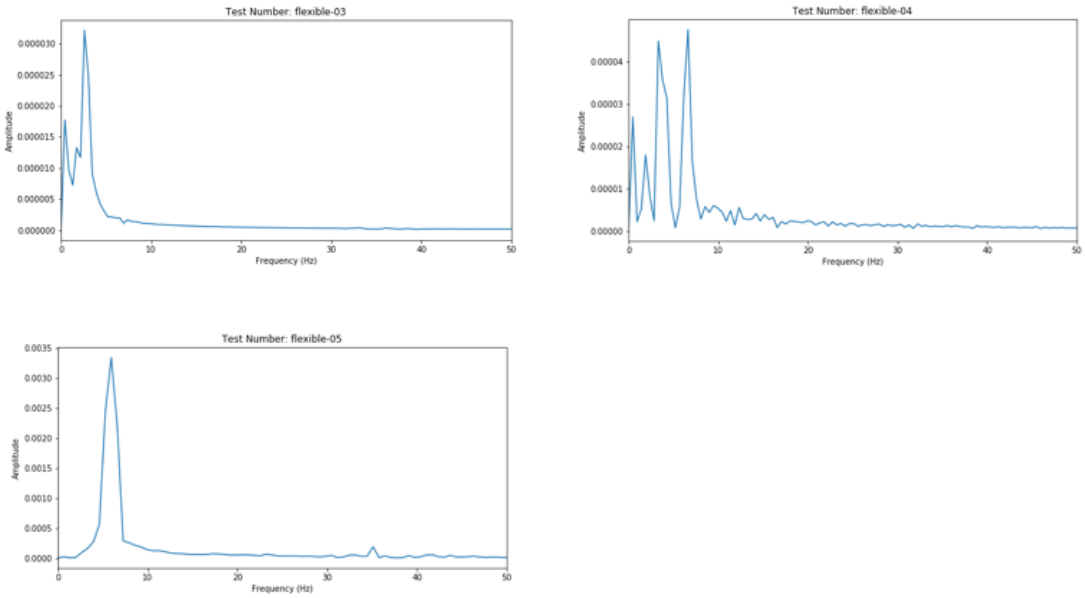

Fig. 7.10 Frequency spectra of F1, F2 and F3 results

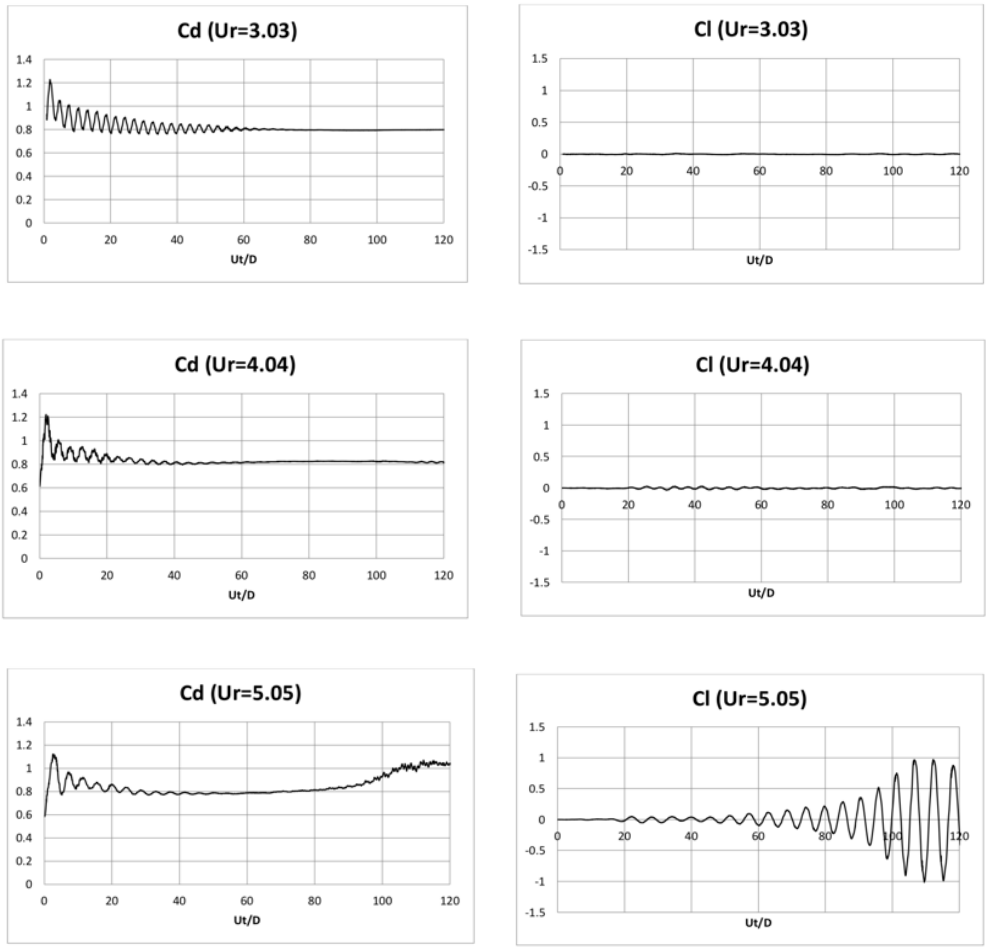

Fig. 7.11 Comparison of drag and lift coefficients for flexible cylinder at 3 reduced velocities

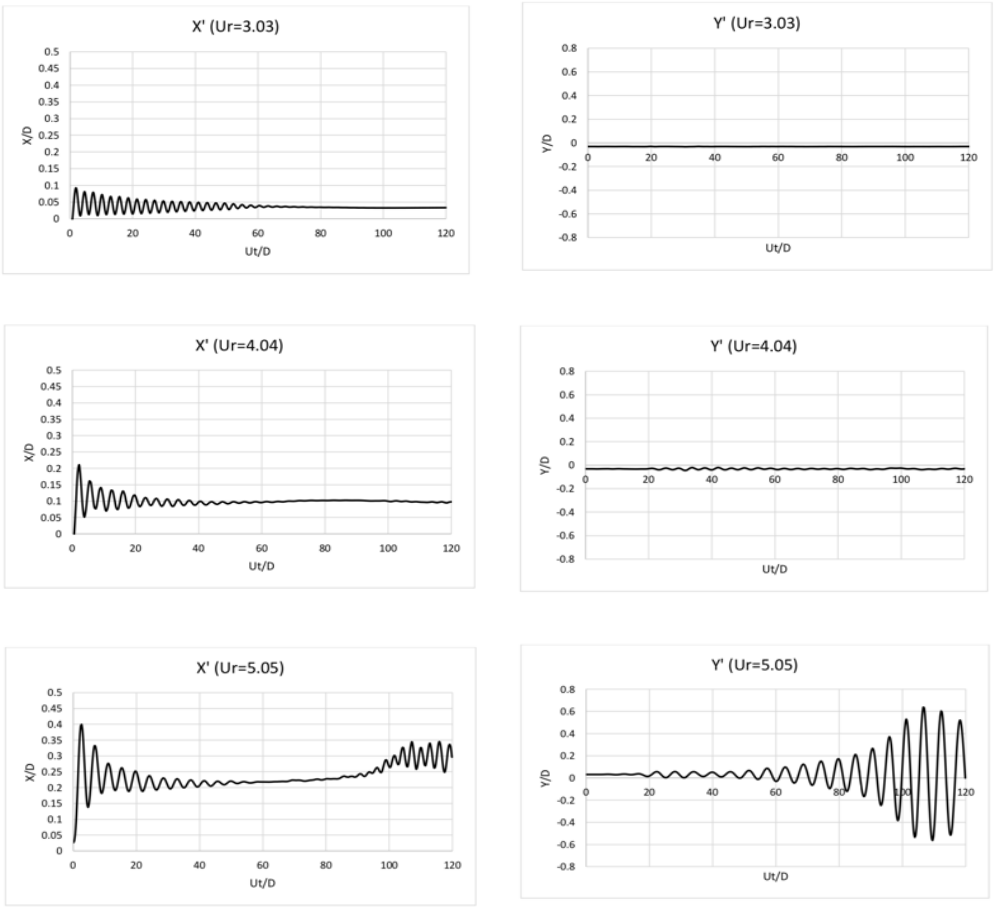

Fig. 7.12 Comparison of inflow and cross flow displacements for flexible cylinder at 3 reduced velocities

Fig. 7.12 shows the comparison of the displacement of the cylinder tip. The displacements are non-dimensionalized as $X'=X/D$ and $Y'=Y/D$ where X and Y are the displacements of flexible cylinder tip in inflow and cross flow directions. The amplitudes of the cross-flow motions for Ur=4.04 and Ur=5.05 were found to be 0.02 and 0.635, respectively. These values showed good agreements with Mittal and Navrose (2013)'s computational results. According to their work, Ur=4.0 is the initial excitation region and the vortex induced vibrations are not strong. On the other hand, around Ur=5.0 was the lower branch of the VIV phenomenon and at this part, the oscillations are large. By comparing between the results of Ur=4.04 and Ur=5.05, at the initial region of VIV, the cross-flow oscillations were small whereas, the small oscillations led to large oscillations in the lower branch region of VIV.

7.3 Analysis of flexible pipe deformation using Absolute Nodal Coordinate Formulation (ANCF) method

An in-house finite element was used code to carry out the structural analysis of the worst scenario of flexible pipe arrangements. Structural analysis of a single flexible pipe under the uniform flow having the velocities corresponding to Level 2 tsunami flows was considered. The in-house code used in this research is a kind of FEM solver but it employs Absolute Nodal Coordinate Formulation (ANCF). In ANCF method, the motion of a linear object with large deformation and large displacements can be expressed using absolute coordinate and the gradients of the line object are used as nodal coordinates (Suzuki et al., 2017). Thus, this method can be used to simulate the structural problems involving very large deformations, torsion and highly non-linear deformations. The derivation and detailed explanation of ANCF method can be found in references (Shabana et al., 1998, Gerstmayr et al., 2006, Nobuyuki Shimizu (Editor) 2007, Schwab et al. 2010).

7.3.1 Boundary conditions and solution procedure

In the FEM analysis, the pipe is considered as a series of multiple beam elements with uniform Young's modulus throughout the pipe length. A uniform flow is applied to the flexible pipes. For the boundary conditions, the bottom end of the pipe is fixed with motion of the bottom node (Fig. 7.2a). In Fig. 7.2b, the solver procedure of the simulation is shown. First, hydrodynamic forces acting on each element are computed from flow velocity and nodal velocities and accelerations, for the flow direction (x-direction). For the z direction, gravity and buoyant forces are also considered. The detail considerations of hydrodynamic forces can be found in the works of Nakajima et al. (1983) and Takehara et al. (2011). After that, the following equation of motion is solved to obtain the acceleration of the nodes.

$$\mathbf{M}\ddot{\boldsymbol{e}} + \mathbf{K}\boldsymbol{e} = \mathbf{Q}_{\boldsymbol{e}} \tag{7.20}$$

Where **M** is the mass matrix obtained from ANCF formulation, **K** is the stiffness matrix which depends on the bending stiffness (EI) of the flexible pipe and $\mathbf{Q}_e$ is the external force vector which includes hydrodynamic forces acting on the nodes.

By solving this motion equation, the nodal acceleration, velocity and displacements are obtained. Nodal velocity is used in the calculations of hydrodynamic forces in the next time step. In this way, the solution for fluid-structure interaction problem is established. Fourth order Runge-Kutta method is used for time-stepping. Each simulation was carried out for the time period of 12.0 seconds which is enough to reach the steady state solution.

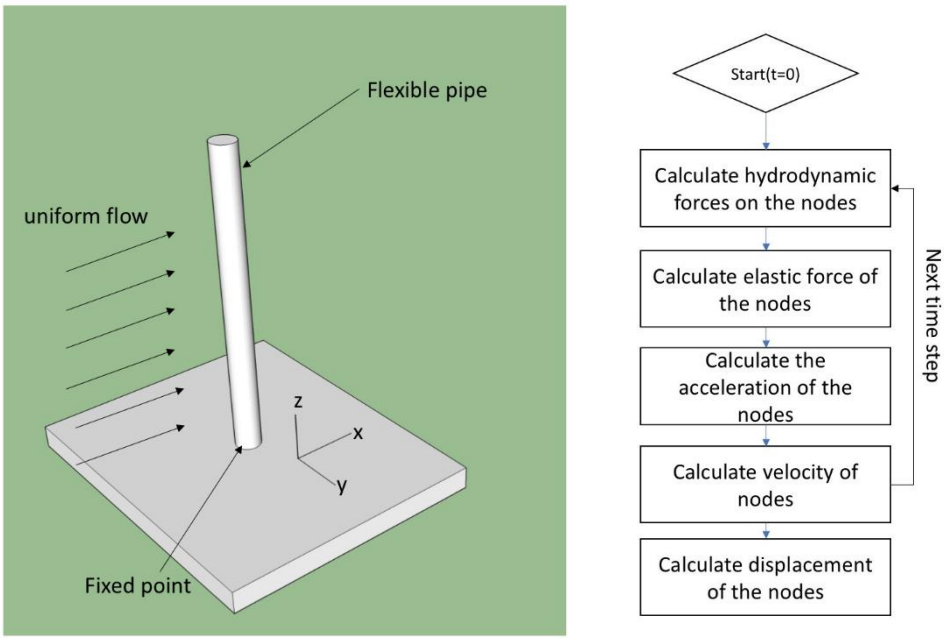

Fig. 7.13 (a) Schematics of the FEM simulation (b) Flow chart of the computation procedure

7.3.2 Simulation of scale-model flexible pipe deformation under a uniform flow

7.3.2.1 Simulation conditions

Firstly, simulations were carried out for 1:100 scale model silicone pipe used in Chapter 6. From the previous section, the drag coefficients of a finite length cylinder at Reynolds numbers below 1000 were observed to be approximately 1.0 for the case where vortex induced vibrations (VIV) phenomena occurred. Thus, C_D = 1.2 was assumed for the structural simulations for estimation of deformation of scale model pipes. Three different diameters were considered (0.01 m. 0.015 m and 0.02 m diameter pipes) while the length was kept the same (0.15m) for all the cases. Bending stiffness (EI) for 0.01 m diameter pipe is obtained from the measurements of silicone pipe shown in Section 4.2 while those for the larger diameter pipes were interpolated values. Three flow velocities were used, with the assumption of tsunami flow as an unsteady uniform flow. The flexible pipe was evenly discretized using 50 elements. The element length is 0.003 m. The detail simulation conditions are tabulated as in Table 7.5.

Table 7.6 Simulation Conditions for the structural analysis of model-scale pipes

Variable	Value			Unit
Pipe Length	0.15			m
Flow Velocity	0.5, 0.6, 0.7			m/s
Water Density	1000			kg/m^3
Pipe Density	9.467			kg/m^3
Pipe Diameter	0.01	0.015	0.02	m
Bending Stiffness	$3.47x10^{-10}$	$7.66x10^{-10}$	$1.91x10^{-9}$	MPa . m^4
Number of Elements	50			
Element Size	0.003			m
Time Step (Δt)	1.00E-06			sec

7.3.2.2 Results and discussions

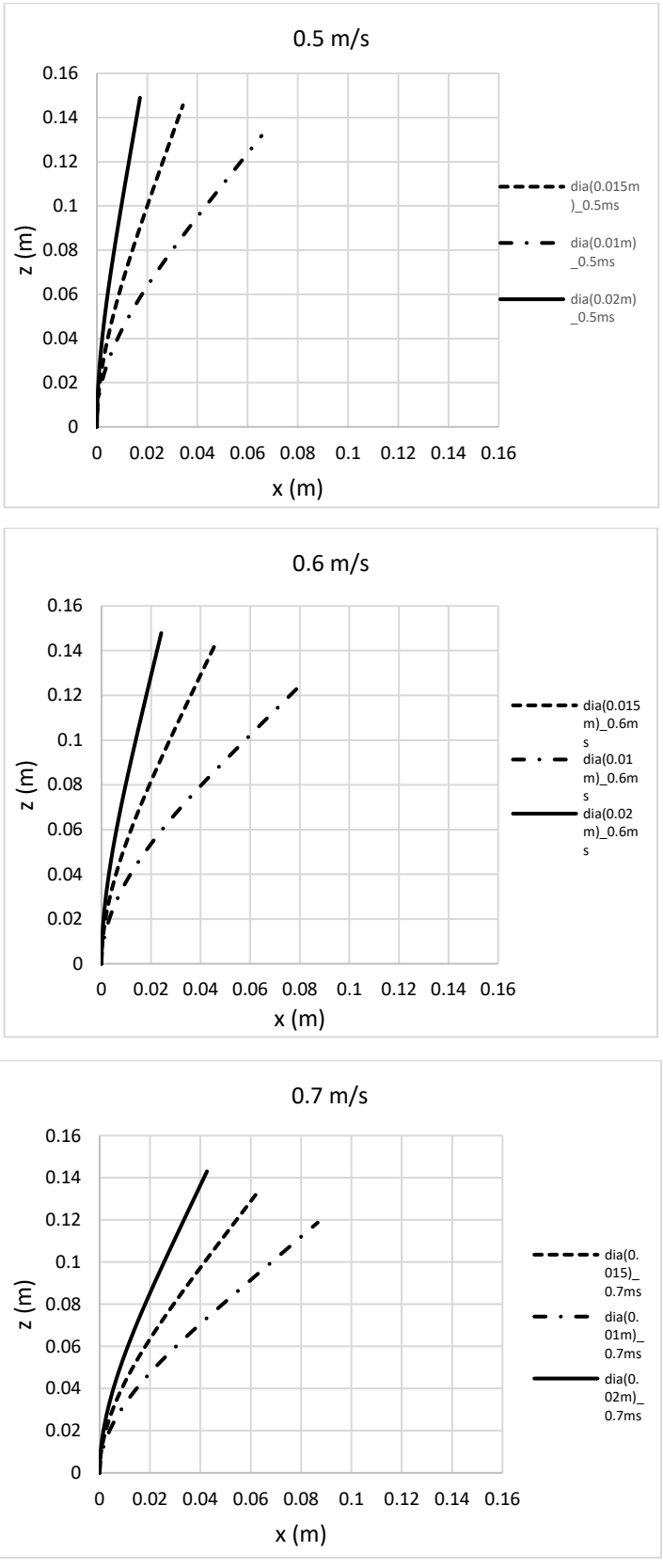

Fig. 7.14 Deformation of air injected flexible pipe under uniform velocities: 0.5 m/sec, 0.6m/s and

The purpose of this simulation is to test the performance of flexible pipes at the model scale and to investigate the effects of scale on the deformation. The results of scale model flexible pipe simulations are shown in Fig. 7.14. At 0.5 m/sec inflow velocity, all three pipes showed very small deformations. The deformations increased non-linearly as the inflow velocity increased, especially for 0.01m pipe which has significantly smaller bending stiffness. From this test, the scale-model pipes were observed to perform well in up to 0.7 m/s flows. Since the increment in deformation is non-linear, relatively larger deformations are expected at higher flow velocities, especially for 0.01m diameter pipe. Moreover, these results should be compared with the full-scale pipe results.

7.3.3 Simulation of full-scale flexible pipe deformation under a uniform flow

7.3.3.1 Simulation conditions

At this stage, ANCF analysis was carried out for the full-scale pipes. The specifications of the pipes proposed in Section 3.4 of Chapter 3 were used. Air and water injected pipes were used, with the inner pressures 0.2MPa and 1.0MPa, respectively, due to the restrictions explained in Section 3.4. Reynolds numbers for flow around full-scale pipes are in the order of 10^6. The drag coefficient of a circular cylinder at this flow regime is approximately 0.8. From the drag coefficient results of fluid structure interaction simulations presented in previous section, C_D was observed to have increased by 20 percent, leading to Re=1.0. However, Re=1.2 was also assumed in order to include a reliable safety factor. The detail simulation conditions are described in Table 7.7.

Table 7.7 Simulation Conditions for the structural analysis of full-scale pipes

Variable	Value			Unit
Pipe Length	15			m
Flow Velocity	5.0, 6.0, 7.0			m/s
Water Density	1000			kg/m3
Pipe Density (Air injected)	9.467			kg/m3
Pipe Density (Water injected)	1008.242			kg/m3
Pipe Diameter	1	1.5	2	m
Bending Stiffness (Air)	0.153	0.516	1.224	MPa . m^4
Bending Stiffness (Water)	4.8	24.3	76.8	MPa . m^4
Number of Elements	100			
Element Size	0.15			m
Time Step (Δt)	1.00E-05			sec

7.3.3.1 Results and discussions

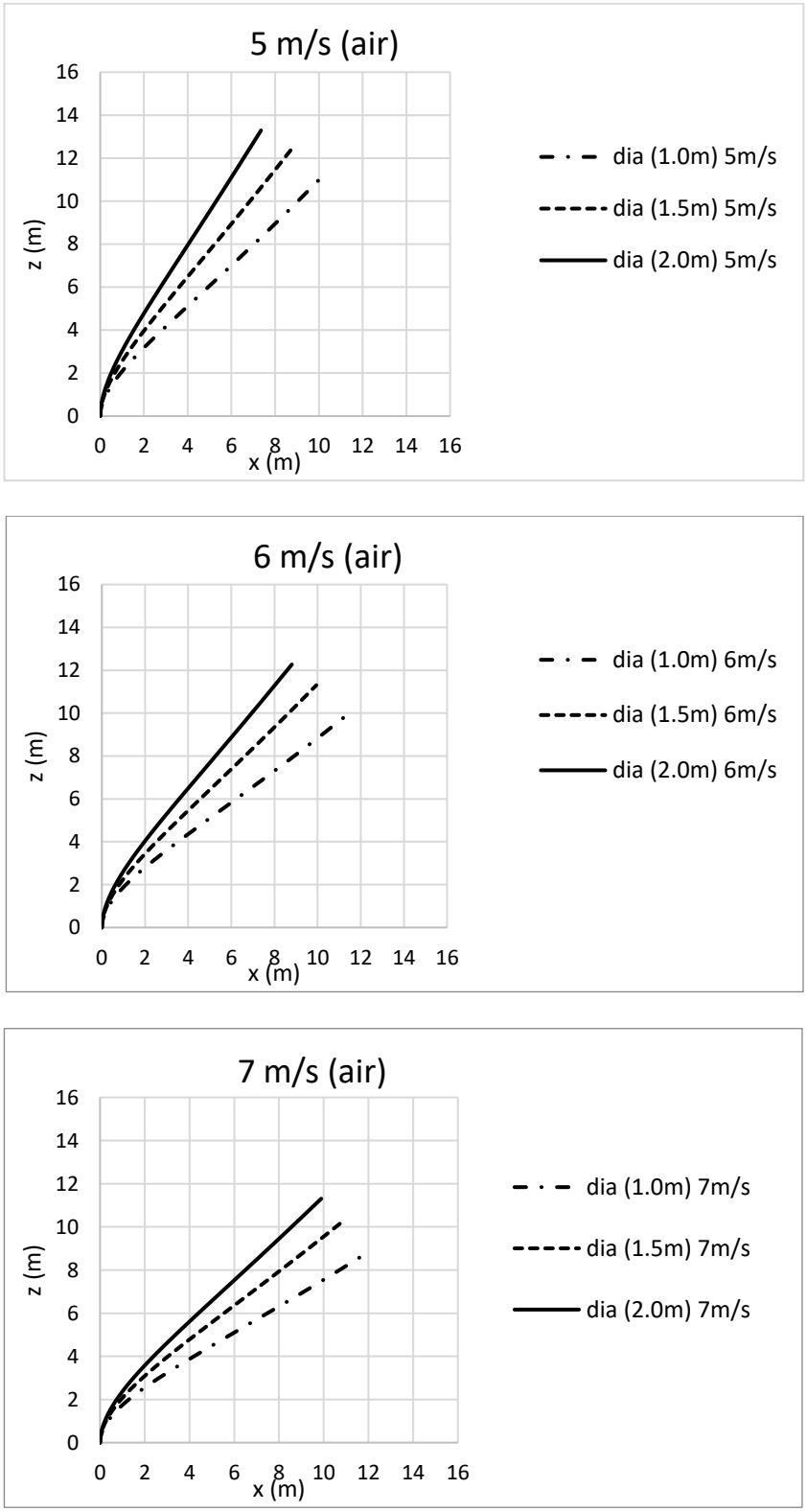

Fig. 7.15 Deformation of air injected flexible pipe under uniform velocities (a) 5 m/sec (b) 6 m/sec (c) 7 m/sec

The simulation results for the air injected pipes are shown in Fig. 7.15. For 5 m/s flow, 1.5m diameter and 2.0m diameter pipes showed very similar deformations while the deformation of 1.0m pipe was significantly larger. For 6 m/s and 7 m/s flows, 1.0m and 1.5m pipes showed significantly larger deformations while 2.0m diameter pipe showed much less deformations than the smaller pipes. This is due to the difference in bending stiffness (EI) values between different pipe diameters. From these simulation results, 2.0m diameter pipes are the most favorable because of smaller deformations compared to 1.0m and 1.5m diameter pipes.

By comparing the full-scale results with the model scale results, it is observed that the deformation increased in a non-linear manner. It can be deduced that there is a certain level of nonlinearity between the bending stiffness and structure deformations.

The results for water injected pipes are shown in Fig. 7.16. By injecting higher pressure water, the bending stiffness (EI) is estimated to increase by over 3 times than air injected pipes. However, the water injected pipes showed only slightly better performance than air pipes because the buoyant forces of the air pipes were much larger than water pipes. This net buoyancy acted as a tensile force in the axial direction of the air injected pipes while the net buoyant force of the water injected pipes was approximately zero. Thus, the smaller EI was compensated by buoyant force for the air injected pipes such that the differences in deformations were insignificant between air and water pipes. The simulation results suggested that air and water injection have small difference in effectiveness. Therefore, both methods might be eligible for the practical implementation.

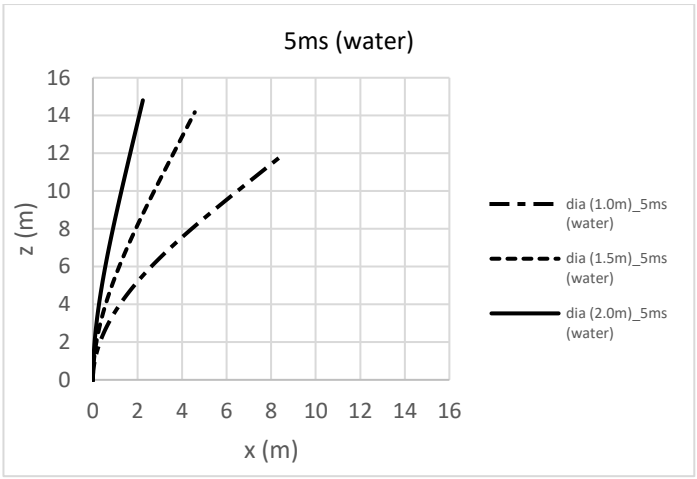

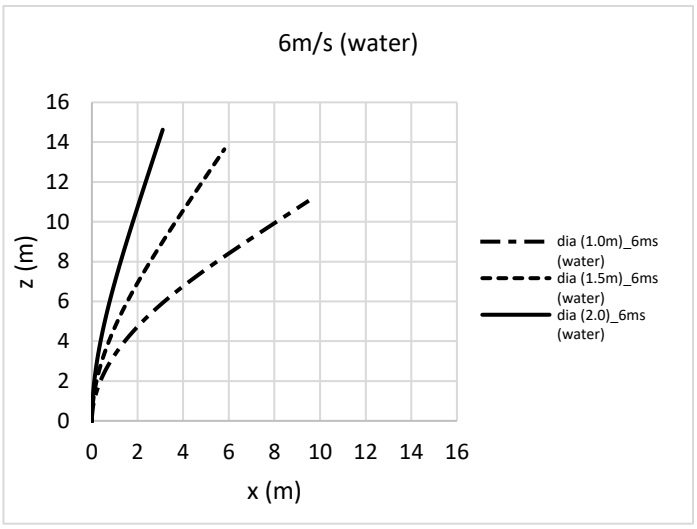

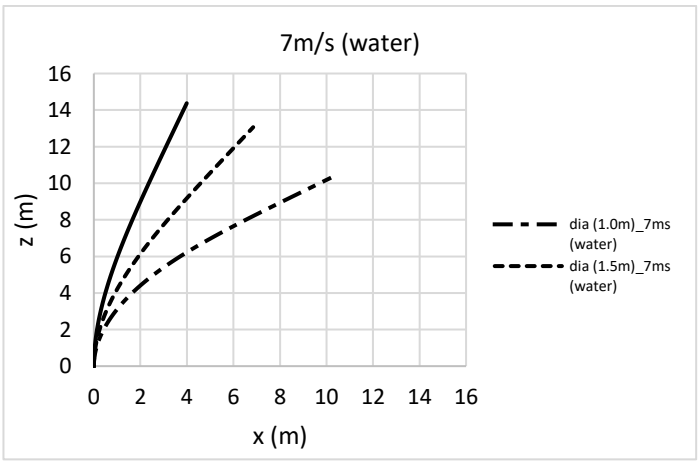

Fig. 7.16 Deformation of water injected flexible pipe under uniform velocities (a) 5 m/sec (b) 6 m/sec (c) 7 m/sec

These simulations represent the pipes located nearest to the tsunami wave head. Much less deformations are expected for the pipes far from the open sea because of the reduction in velocity and elevation of tsunami flow due to the nearer pipes. On the other hand, manufacturing of 1.5m and 2.0m diameter pipes have higher costs than 1.0m pipes. Therefore, at this stage of research, 1.0 m or 1.5 m diameter pipes were considered to be feasible for real-world implementation.

7.4 Prediction on the tsunami force reduction for full-scale by CFD approach

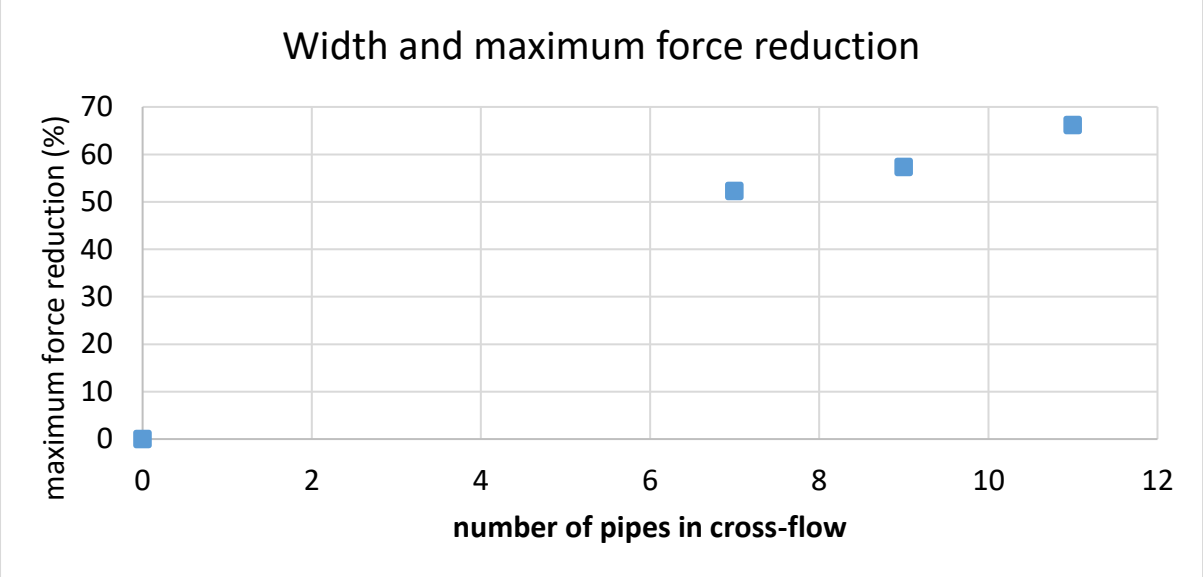

Fig. 7.17 Results on the prediction of force reduction for full-scale spherical tank using rigid pipes

CFD simulations were conducted based on the numerical model presented in Section 5.3 of this thesis in order to estimate the reduction of tsunami force for a full-scale spherical tank. The effectiveness for increased number of pipes in cross-flow direction using 7, 9, and 11 pipes in cross-flow direction, totaling 33, 43 and 53 pipes, respectively.

From the numerical results, over 50% of hydrodynamic force reduction was obtained. This reduction rate increased as the number of pipes increased in cross-flow direction. If flexible pipes are utilized instead of rigid pipes, this reduction rate will decrease to a smaller scale due to deformation of the pipes causing reduction in effective cross-sectional area. Overall, the use of flexible pipes are effective and feasible for practical implementation.

7.5 Conclusions

In the first part of the chapter, flow induced motions of a flexible finite length cylinder were numerically investigated using a strongly coupled FSI method in a finite volume framework. For smaller reduced velocities, only very small cross flow motions were observed whereas for Ur=0.5 case, large motions amplitudes were observed due to the occurrence of vortex induced vibrations. According to the numerical results, it can be deduced that the drag coefficients increased above 1.0 when VIV. However, these values are still smaller than the assumed value: C_D = 1.2. Thus, this drag coefficient could be used in further simulations to predict the deformation of the pipes. However, further simulations at higher Reynolds numbers with turbulence model should be carried out in order to confirm the feasibility of this C_D value. This research is one of the very few attempts to study the fluid structure interaction phenomenon of finite length structures using computational approach. Fixed-point relaxation with Aitken adaptive relaxation could effectively accelerate the convergence while still maintaining the stability of the simulations. The OpenFOAM framework used in this study is fully open-source and can be used and further developed for the numerical studies of FSI problems. Therefore, this approach can also be used as a tool in the study and development of flexible structures under flows such as biologically inspired applications.

In the second part of this chapter, structural analysis of flexible pipes were carried out by using one way fluid structure interaction approach with ANCF method in order to estimate the

deformations of a single flexible pipe under a Level 2 tsunami. The structural simulation results showed that 1.0m diameter pipes had good performance up to 6 m/s tsunami flows without unacceptably large deformations. For higher flow velocities, the deformations of 1.0 m pipe increased significantly. However, for multiple flexible pipes, it can be argued that the deformation of pipes away from tsunami wave direction would show relatively smaller deformations. On the other hand, 1.5 m diameter pipes showed good performance for flow velocities ranging to 7 m/s, provided that kink or non-linear buckling do not occur. From this analysis, the flexible pipes approach is feasible for practical implementation by the simulation parameters proposed in this thesis.

Chapter 8

Conclusions and future work

A new approach of tsunami countermeasure was developed in order to protect large-scale secondary disasters caused by tsunamis by protecting tsunami vulnerable industrial complexes. Being inspired by natural tsunami countermeasures such as mangrove and giant-Kelps, this approach utilizes flexible, foldable structures instead of traditional rigid wall type tsunami countermeasures. This method allows instant deployment of the countermeasure near the vulnerable areas at the occurrence of a tsunami while there will be no disturbance to marine traffic due to the countermeasure. In this thesis, experimental and numerical studies on the effectiveness and feasibility of this flexible-pipe-type tsunami countermeasure are presented. Each type of experiments were carried out at least 5 or 6 times in order to obtain a reliable and reproducible data, leading to approximately 160 total runs in the tsunami wave basin.

8.1 Conclusions

8.1.1 Conclusions on the effectiveness of flexible pipes

The tsunami basin experiments suggested that the application of flexible pipes could reduce the hydrodynamic force acting on the oil tanks by the tsunami flow, as well as flow velocity. By comparing the effectiveness of different types of materials with different bending stiffness (EI) values, the maximum tsunami load could be reduced up to approximately 35 percent by

using flexible silicone pipes and up to 44 percent by using more rigid pipes such as those made of urethane rubber and ABS. However, the rigid pipes are likely to disturb the marine traffic around the area of installation whereas the flexible pipes would not. According to these results, the use of flexible pipes could be considered as a tsunami damage reduction mechanism for oil and gas refineries, located in the areas vulnerable to tsunami attacks.

The experiments with rigid pipes were replicated in numerical model using finite volume technique with Volume of Fluid (VoF) method. This numerical model was validated by comparing with the experimental data. Numerical results showed good agreement with experiments for flow velocity and hydrodynamic forces. The peak values of hydrodynamic forces computed by CFD agreed with the measurements, and CFD could predict the flow phenomena well. Then, this method was employed to estimate the relationship between the force reduction of the pipes and the width of the arrangement. As the width of the flexible-pipe arrangement in the cross-flow direction increases, the force reduction will increase with the form of exponential recovery, reaching a constant value. Therefore, the number of rows of pipes should be increased in the inflow direction for better reduction of tsunami force. Such a model can be extended for multiple oil and gas tanks and used to predict the tsunami damage reduction for a large coastal area, such as the Osaka Bay.

By carrying out quasi-2D experiments using the flexible pipes arrangement covering the whole width of the wave flume, the momentum flux with or without the influence of scale-model oil tank located on the wave basin floor, being semi-submerged, was measured. It was observed that the unsteady momentum flux could be reduced up to 50 percent. This results can be used to estimate the reduction of tsunami drag force on a general structure such as a residential area or an industrial zone. By measuring the hydrodynamic force acting on the oil tank as well as the flow velocity and elevation in front of the oil tank, Morison Equation was found to be useful in estimating the unsteady horizontal force acting on energy storage tanks by a tsunami wave.

It was observed that 40% of hydrodynamic force acting on the cylindrical oil tank decreased when flexible pipes were installed. Better results are expected for different sizes of model tanks. From the experiments with the earth-bank and dyke wall being considered, the interaction between the bank and the flexible pipes in run-up pattern was observed. It was observed that improper installation of flexible pipes might deteriorate their effectiveness in reduction tsunami energy. By installing the pipes at a suitable location and attaching the dyke wall could reduce tsunami force by up to 50 percent. These results can be used in consideration of the location of the flexible pipes and the design of the energy storage facilities which are vulnerable to tsunami attacks.

8.1.2 Conclusions on the feasibility for implementation of flexible pipes

Flow induced motions of a flexible finite length cylinder were numerically investigated using a strongly coupled FSI method in a finite volume framework. For smaller reduced velocities, only very small cross flow motions were observed whereas for Ur=0.5 case, large motions amplitudes were observed due to the occurrence of vortex induced vibrations. According to the numerical results, it can be deduced that the drag coefficients increased above 1.0 when VIV. However, these values were smaller than those in ANCF analysis. Thus, no further correction to the ANCF simulations was necessary. This research is one of the very few attempts to study the fluid structure interaction phenomenon of finite length structures using computational approach.

Structural analysis of flexible pipes were carried out by using one way fluid structure interaction approach with ANCF method in order to estimate the deformations of a single flexible pipe under a Level 2 tsunami. The structural simulation results showed that 1.0m diameter pipes had good performance up to 6 m/s tsunami flows without unacceptably large

deformations while 1.5 m diameter pipes were suitable for stronger tsunami flows with higher flow velocities. From this analysis, the flexible pipes approach is feasible for practical implementation by given simulation parameters.

From the CFD simulations of full-scale rigid pipes, over 50% of hydrodynamic force acting on a spherical tank could be reduced. It can be deduced that this reduction rate will decrease by using flexible pipes. However, from these results flexible pipes are feasible for reducing tsunami force effectively.

8.2 Recommendations for the future work

Experiments with larger scale ratios should be carried out to confirm the results presented in this thesis and to investigate the influence of higher Reynolds numbers on the flow pattern after the occurrence of wave breaking. Moreover, in the current work, the tsunami wave was represented by a turbulent bore in which unsteady run-up forces were dominant. Longer period waves are preferable to investigate the effectiveness of flexible pipes for a quasi-steady flow part.

For the structural analysis, the FEM analysis with ANCF uses beam elements. Kink or buckling phenomena of an air injected pipe should be investigated using more realistic elements such as shell elements. For the numerical study on the fluid structure interaction of finite cylinder, higher Reynolds numbers and higher reduced velocities should be analyzed using turbulence modeling. For larger displacements in cross-flow directions, a finite volume overset mesh approach is recommended for the fluid solver.

References

Araki, S., Kunimatsu, W., Nishiyama, S., Furuse, T., Aoki, S., & Kotake, Y. 2016. Experimental study on tsunami wave load acting on storage tank in coastal area. J Loss Prevent Proc. Advance online publication. https://doi.org/10.1016/j.jlp.2016.10.004

Bao, T.Q. 2011. Effect of mangrove structures on wave attenuation in coastal Vietnam. OCEANOLOGIA, 53(3):807-818

Boussinesq, M. J. 1872. Theorie des ondes et des remous qui se propagent le long d'un canal rectangulaire horizontal, en communiquant au liquid contenu dans ce canal des vitesses sensiblement pareilles de la surface au fond. J. Math Pures Appl. (2) 17:55-108; translation by A. C. J. Vastano, J. C. H. Mungall, Texas A & M Uni., (March 1976).

Central Disaster Prevention Council (CDPC), 2012. Disaster prevention measures for oil storage tanks, Central Disaster Prevention Council, Disaster Preparedness Promotion Review Conference, 2012 December (In Japanese)

Cruz, A.M., Krausmann, E., Kato, N., & Girgin, S., 2016. Chapter 13 Reducing Natech Risk: Structural Measures In Natech Risk Assessment and Management: Reducing the Risk of Natural-Hazard Impact on Hazardous Installations (E. Krausmann A. Cruz, & E. Salzano, Eds.) pp 211-215, Elsevier.

Earthquake Engineering Research Institute (EERI), 2011. Learning From Tsunamis: The Japan Tohoku Tsunami of March 11, 2011. EERI Special Report.

FDMA, Fire Defense Research Center. 2011. A survey report on the damage and fire-fighting activities of the 2011 Tohoku Region Pacific Coast Earthquake. Japan: National Research Institute of Fire and Disaster. 489 pp. (In Japanese, title translated by the author).

FEMA, 2008. Guideline for design of structures for vertical evacuation from tsunamis, FEMA p646.

Fujii, N. and Imamura, F., 2010. Proposal of the practical evaluation method for tsunami disaster of oil storage tanks and impact by drifting bodies. J. Jap Soc Nat Dis Sci, 28(4). Pp 371-386.

Gatzhammer, B., Mehl, M. and Neckel, T., 2012. A Coupling Environment for Partitioned Multiphysics Simulations Applied to Fluid Structure Interaction Scenarios. Proce. Comp. Sci. 1 (2012) pp 681-689.

Gerstmayr, J., & Shabana, A. A. 2006. Analysis of thin beams and cables using the Absolute Nodal Co-ordinate Formulation. Nonlinear Dynamics, Vol. 45, pp. 109-130

Hatayama, K. Damage to oil storage tanks due to tsunami of the Mw9.0 2011 off the Pacific Coast of Tohoku, Japan. 2014, In: 10th National Conference in Earthquake Engineering, Earthquake Engineering Research Institute, Anchorage, AK.

Heseltine, J. L., 2003. Flow Around a Circular Cylinder with a Free End. Master Thesis. University of Saskatchewan, Canada.

Huang, Z., Yao, Y., Sim, S. Y., Yao., Y., 2011. Interaction of solitary waves with emergent, rigid vegetation, Ocean Eng 38 (2011):1080- 1088

Ikemura, H., Pradono, M. H., Yasuda, T. and Tada, T. 2007. Experiments of tsunami force acting on bridge models, J. Earth. Quak Eng. 2007, pp 902-911.

Imamura, F., Goto, K., and Ohkubo, S. 2008. A numerical model for the transport of a boulder by tsunami. J. Geophys. Res., 113, C01008, doi:10.1029/2007JC004170.

Irtem, E., Gedik, N., Kabdasli, M. S., Yasa, N. E. 2009. Coastal forest effects on tsunami run-up heights. Ocean Eng 36 (2009) 313-320

Japan Meteorological Agency (JMA). 2011. Tsunami Information (Estimated tsunami arrival time and height), http://www.jma.go.jp/en/tsunami/info_04_20110311145026.html

Kato, N., Suzuki, H., Takeuchi, K., 2014, Band of biology-inspired flexible pipes for decreasing damage of oil and gas storage tanks caused by large-scale tsunami, Proc. for ISABMEC 2014, Soci. ABMECH (in CD-ROM)

Kimura, Y., Chikamoto, T., Yoshida, H., Shimosako, K., and Kiyomiya, O. 2012. Field Experiment of Flap-Gate Breakwater. Journal of JSCE, B3, 68(2): I240-I245 (In Japanese).

Krausmann, E., Cruz, A. M., Salzano, E., 2016. Chapter 1 Introduction, In: Natech Risk Assessment and Management: Reducing the Risk of Natural-Hazard Impact on Hazardous Installations, pp 1-2, Amsterdam, Elsevier.

Kunimatsu, W., Nishiyama, S., Aoki, S., Araki, S., Kotake, Y. 2015. Hydrodynamic forces acting on energy storage facilities in a harbor by tsunami inundation flow. Proceedings for 25th Ocean Engineering Symposium, Japan, 2015 August 6,7. (In Japanese).

Liu, H., Sakashita, T. and Sato, S. 2014. An experimental study on the tsunami boulder movement. Proc Coast Eng. 34 (2014)

Matsumoto, K., Izumiya, T. and Ishibashi, K. 2013. Laboratory investigation on tsunami wave forces acting on a horizontal pipeline and oil tanks, Journal of Civil Engineering, Japan. 69 (2), 293 – 298.

Maza, M., Lara, J. L., Losada, I. J., 2015, Tsunami wave interaction with mangrove forests: A 3-D numerical approach, Coast Eng. 98 (2015) 33-54.

Mazda, Y., Magi, M., Ikeda, Y., Kurokawa, T., and Asano, T. 2006. Wave reduction in a mangrove forest dominated by Sonneratia sp. Wet Ecol and Manag (2006) 14:365–378.

Ministry of Land, Infrastructure, Transport and Tourism, Japan (MLITT). 2012. Concept of comprehensive tsunami countermeasures. In: 2nd Disaster Management Meeting, Transport Policy Council, Port Section. (In Japanese, title translated by the author).

Mori, N., Takahashi, T., 2012. Nationwide post event survey and analysis of the 2011 Tohoku earthquake tsunami. Coast Eng J. 54, (1): 1250001-1-27.

Muhari, A., Imamura, F., Suppasri, A., Mas, E., 2012, Tsunami arrival time characteristics of the 2011 Great East Japan Tsunami obtained from eyewitness accounts, evidence and numerical simulation, J Nat Disast Sci. 34(1), pp 91-104.

Nakajima, T., Motora, S., and Fujino, M. 1983. A three dimensional lumped mass method for the dynamic analysis of mooring lines. Journal of Society of Naval Architects of Japan, 154. pp. 192-202

Nobuyuki Shimizu (Editor; Edited by Japan Society of Mechanical Engineers). 2007. Multi body dynamics (2). Corona Publishing Co. Ltd., pp. 108-145 (in Japanese)

Okubayashi, T. 2014. Study on Tsunami Damage Reduction Method Using Flexible Pipes. Bachelor thesis. Osaka University, pp 44.

Park, H., Cox, D. T., and Barbosa, A. R., 2017. Comparison of inundation depth and momentum flux based fragilities for probabilistic tsunami damage assessment and uncertainty analysis. Coast Eng. 122 (2017), pp 10-26.

Park, H., Cox, D. T., Lynett, P. J., Wiebe, D. M., and Shin, S., 2013. Tsunami inundation modeling in constructed environments: A physical and numerical comparison of free-surface elevation, velocity and momentum flux. Coast Eng. 79 (2013), pp 9-21.

Ramsden, J.D., 1993. Tsunamis: forces on a vertical wall caused by long waves, bores, and surges on a dry bed. Ph.D. Dissertation, California Institute of Technology, pp251.

Rosman, J. H., Denny, M. W., Zeller, R. B., Monismith, S. G., Koseff, J., R. 2013. Interaction of waves and currents with kelp forests (Macrocystis pyrifera): Insights from a dynamically scaled laboratory model. Limnol. Oceanogr. 58(3), pp. 790-802.

Shabana, A. A., Hussein, H. A., and Escalona, J. L. 1998. Application of the Absolute Nodal Coordinate Formulation to Large Rotation and Large Deformation Problems, ASME J Mech Des, 120, pp. 188-195

Suppasri, A., Shuto, N., Imamura, F., Koshimura, S., Mas, E., Yalciner, A. C., 2013. Lessons Learned from the 2011 Great East Japan Tsunami: Performance of Tsunami Countermeasures, Coastal Buildings and Tsunami Evacuation in Japan. Pure Appl Geophys. 170 (2013), 993-1018.

Suzuki, H., Tomobe, H., Takasu, H., Kuwano, A., Inoue, T., and Ishiwata, J. 2017. Numerical Analysis of the Motion of ROV Applying ANC Method to the Motion of Tether Cable, 27th ISOPE, 25-30 June, San Franciso, California, USA.

Suzuki, T., Zijlema, M., Burger, B., Meijer, M. C., Narayan, S. 2011. Wave dissipation by vegetation with layer schematization in SWAN.

Takayama, T., Arikawa, T., Nishimura, D., and Hitasawa, M., Development of Urgently Emerging Tsunami Breakwater-Buoyancy-Driven Vertical Piling System. 2010, J Coastal Development Institute of Technology (In Japanese).

Takehara, S., Terumichi, Y., Sogabe, K. 2011. Motion of a submerged tether subject to large deformations and displacements. Journal of System Design and Dynamics, 5(2), pp. 296-305

Tanaka, N., Sasaki, Y., Mowjood, M., Jinadasa, K., Homchuen, S., 2007, Coastal vegation structures and their functions in tsunami protection: experience of the recent Indian Ocean tsunami, Landscape Ecol Eng, No. 3, pp. 33-45.

Tar, T., Kato, N., Suzuki, H., Nagai, Y., Ohnishi, K., Okbayashi, T. 2017. Experimental and numerical study on the reduction of tsunami flow using multiple flexible pipes, J Loss Prevent Proc. http://dx.doi.org/10.1016/j.jlp.2017.03.007

Tokida, K., & Tanimoto, R., Lessons and views on hardware countermeasures with earthbanks against tsunamis estimated in 2011 Great East Japan Earthquake. Soils Found 2014; 54(4):523–543.

Yeh, H., 2006. Maximum fluid forces in the tsunami runup zone. J. Waterway, Port, Coastal and Ocean Eng, ASCE, 132. Pp 496-500.

Zama, S., Nishi, H., Hatayam, K., Yamada, M, Yoshihara, H., & Ogawa, Y. 2012. On Damage of Oil Storage Tanks due to the 2011 off the Pacific Coast of Tohoku Earthquake (Mw9.0), Japan, Proceedings of 15 WCEE (World Conference on Earthquake Engineering). Lisboa, Portugal. Available at: http://www.iitk.ac.in/nicee/wcee/article/WCEE2012_0238.pdf